Gust Response and Control of Very Flexible Aircraft

by

Matthew J. Dillsaver

A dissertation submitted in partial fulfillment
of the requirements for the degree of
Doctor of Philosophy
(Aerospace Engineering)
in the University of Michigan
2013

Doctoral Committee:

Professor Carlos E. S. Cesnik, Co-Chair
Professor Ilya V. Kolmanovsky, Co-Chair
Professor Bogdan Epureanu
Christopher M. Shearer, United States Air Force

2013

A C K N O W L E D G M E N T S

I would like to first thank the United States Air Force and the Air Force Institute of Technology for giving me this wonderful opportunity and funding me throughout my time in Michigan.

I would also like to acknowledge my co-advisors, Professors Carlos E. S. Cesnik and Ilya V. Kolmanovsky. Their support, guidance, knowledge and inspiration has been immense during this process. I would also like to thank the other members of my committee, Prof. Bogdan Epureanu and Lt. Col. Christopher M. Shearer, for their suggestions during the review of this dissertation.

To my wife and daughter, I am thankful for the love and support you have provided. Sometimes I wasn't home as much as I wanted and was on the computer many times when I was there.

Finally, to all of my fellow graduate students with whom I have interacted, I am grateful for the suggestions and discussion on this research effort and other subjects.

TABLE OF CONTENTS

LIST OF FIGURES

LIST OF TABLES

LIST OF APPENDICES

ABSTRACT

Gust Response and Control of Very Flexible Aircraft

by

Matthew J. Dillsaver

Co-Chairs: Carlos E. S. Cesnik and Ilya V. Kolmanovsky

Current aircraft designs envisioned for high altitude, long endurance flight bear little resemblance to modern airliners. Therefore, many modeling and simulation techniques used to design and test conventional aircraft are not suitable for this class of aircraft. This become evident in the 2003 crash of the NASA sponsored AeroVironment Helios aircraft after an encounter with a gust disturbance. A lack of understanding of the complex interactions present in very flexible aircraft (VFA) and the lack of accurate modeling techniques of very flexible aircraft was cited as a cause of the mishap.

This dissertation studies the response of very flexible aircraft models to gust disturbances and introduces methods for controlling the aircraft within this environment. The stiffness properties of the baseline aircraft models are varied, while keeping the inertial and geometric properties constant, to create multiple models for testing. These models are then subjected to external gust disturbances of varying time scales in fully nonlinear simulations. The aircraft response to the gust is then correlated with the aircraft stiffness parameters, as well as various ratios involving stiffness parameters and flight dynamic mode frequencies.

The contributions of this dissertation include a new control technique for minimizing the bending moment induced on the aircraft by a gust disturbance. The curvature of the

wing, which is proportional to the bending moment, is assumed to be a state available for feedback. A controller is then designed to use the control surfaces to minimize the deviations in wing curvature caused by a gust encounter or by maneuvering flight. The controller is validated on a linearized aircraft model and then in a fully nonlinear simulation.

As another contribution, a two-loop control architecture for tracking longitudinal trajectory commands is developed. A new outer loop is introduced which uses a combination of proportional, integral, derivative as well as sliding mode control. The body frame velocities are tracked using a dynamic inversion inner loop. Control of the lateral states is demonstrated using an output feedback controller designed using a reduced order linear aircraft model. This control scheme is first demonstrated in still air and then multiple discrete and stochastic gust disturbances are added. The wing curvature controller is then added to the system, allowing for reduced bending moments and virtually no degradation in tracking performance. Finally, the control architecture is augmented with reference and extended command governors to enforce constraints on the wing curvature during maneuvering flight with gust disturbances.

The closed loop sensitivity of this class of aircraft to changes in stiffness parameters is also studied. Aircraft models previously used for the open loop study are simulated in the closed loop system described above. The VFA models are given longitudinal trajectory commands in both still air and with a gust disturbance. The aircraft responses are then evaluated in a similar manner to the open loop sensitivities. Conclusions are then drawn about methods of VFA aircraft design to maximize open and closed loop performance during gust encounter.

CHAPTER 1

Introduction

Aircraft design has come a long way since the Wright Brothers flight at Kitty Hawk in 1903. Modern swept wing jet-powered airliners bear almost no resemblance to the aircraft they flew on the North Carolina beach that December day. Currently, there is much research effort being put into High Altitude Long Endurance (HALE) aircraft. These aircraft are envisioned to be powered in such a way as to have endurance of days, weeks, or in the case of solar powered HALE aircraft a theoretical endurance of years. This long endurance combined with flight ceilings in some cases of 100,000 feet make HALE aircraft very desirable for military applications. Military planners are envisioning using HALE aircraft in a similar manner as satellites, with the ability to provide persistent Intelligence, Surveillance, and Reconnaissance (ISR) ability over large areas, but also the ability to easily move from one area to another.

The mission of HALE aircraft leads them to bear little resemblance to modern jet airliners. They are normally built with long, flexible wings creating high lift-to-drag ratios and thereby maximizing aerodynamic efficiency. Additionally, lightweight materials are used to the maximum extent possible with structural engineers trying to minimize the structural weight. These attributes mean that HALE aircraft tend to be very flexible, with large wing deformations possible in flight. These Very Flexible Aircraft (VFA) also may exhibit an overlap between the lowest elastic mode frequencies and the rigid-body, flight dynamic frequencies, which is not normally seen in more conventional aircraft designs [1].

These VFA characteristics can lead it to be much more susceptible to external disturbances such as wind gust. This susceptibility was manifested in the Aerovironment Helios mishap in June 2003. The aircraft encountered unexpected turbulence shortly after takeoff on a test flight from Hawaii. The turbulence caused the aircraft to enter a high dihedral flight condition. As a result, the aircraft began an unstable, divergent pitch oscillation with airspeed excursions doubling on every oscillation. Eventually, the design airspeed was exceeded and the aircraft broke apart and fell into the Pacific Ocean. The mishap report [2] named the following as root causes of the accident:

1)" Lack of adequate analysis methods led to an inaccurate risk assessment of the effects of configuration changes leading to an inappropriate decision to fly an aircraft configuration highly sensitive to disturbances."

2) "Configuration changes to the aircraft, driven by programmatic and technological constraints, altered the aircraft from a spanloader to a highly point-loaded mass distribution on the same structure significantly reducing design robustness and margins of safety." As these findings point out, there is a fundamental lack of understanding of the flight dynamics of these aircraft and the effect that configuration changes could make. Additionally, the report also highlights a lack of models and tools to accurately asses the performance of VFA aircraft. In fact two of the recommendations from the mishap report are:

1) "Develop more advanced, multi-disciplinary (structures, aeroelastic, aerodynamics, atmospheric, materials, propulsion, controls, etc.) "*time-domain*" analysis methods appropriate to highly-flexible "morphing" vehicles."

2) "Develop multidisciplinary (structures, aerodynamic, controls, etc) models, which can describe the nonlinear dynamic behavior of aircraft modifications or perform incremental flight testing."

1.1 Previous Work

There has been significant research activity recently into the issues raised in the Helios mishap report. This section will serve as a review of those in the areas related to this dissertation. First, the relevant literature in the area of VFA flight dynamics and their response to gust disturbances is reviewed. Next, a review of the literature on gust load alleviation for flexible aircraft is reviewed.

1.1.1 VFA Flight Dynamics

In recent years, there has been a growing amount of research into the flight dynamics of HALE aircraft and VFA. Van Schoor, Zerweckh and von Flotow [3] performed an aeroelastic analysis of a human-powered aircraft, but also stated that the characteristics of this aircraft: very flexible wings, high aspect ratio and low wing loadings, are typical of HALE aircraft. They found that the effect of the unsteady aerodynamics on aircraft dynamics is significant. Additionally, in order to accurately model the dynamics, the flexibility of the aircraft must be included. Finally, they showed that the dynamics are sensitive to changes in flight conditions, specifically speed and altitude.

Patil, Hodges and Cesnik [4] performed a nonlinear aeroelastic study on a HALE aircraft model. The large deformations due to the flexibility of the wings caused changes in their aeroelastic behavior, which can only be accounted for in a nonlinear analysis. The trim solution, as well as the short-period and phugoid mode frequencies, was also found to be a function of wing flexibility. The authors also showed that neglecting these dependencies would lead to very different aircraft behavior.

Chang, Hodges and Patil [5] completed an aeroelastic analysis of highly flexible aircraft. The payload distribution had a large effect of the trimmed shape of the aircraft, and this shape was shown to cause large changes in aircraft flight dynamics. Also, the aerodynamic and wing flexibility were found to be strongly coupled, resulting in a large change

in trim condition as a result of a small change in design parameters.

Palacios and Cesnik [6] compared displacement-based, strain based, and geometrically nonlinear beam models for use in modeling the large deformations in high aspect-ratio wings. They found an efficient approach is to utilize different beam representations depending on the part of the aircraft being modeled. A good solution was presented using a displacement based method for the fuselage and tails, and a strain based or geometrically nonlinear beam model for the flexible wings.

Su and Cesnik [1] presented an analysis of the coupled nonlinear flight dynamics and aeroelasticity of highly flexible flying wings. They showed that a finite gust disturbance could cause divergent oscillations on a stable aircraft model. Furthermore, they demonstrated that the addition of a center payload change the aircraft from a span loaded to a point mass loaded configuration. These changes affected not only the flight dynamic characteristics and trimmed shape of the aircraft, but also created an unstable phugoid mode.

Shearer and Cesnik [7] studied the nonlinear flight dynamics of a VFA model using a formulation which couples the flight dynamics and aeroelastic equations of motion using a strain-based geometrically nonlinear formulation and an implicit modified Newmark integration method. The responses of nonlinear rigid-body, linearized, and fully nonlinear solutions were compared. The rigid-body formulation was found to be insufficient to capture the aircraft response. For symmetric maneuvers, the linearized formulation was found to be sufficient. However, when asymmetric maneuvers were simulated, it was discovered that a fully nonlinear solution was necessary to accurately capture aircraft response.

Palacios, Cesnik and Reichenbach [8] presented a critical review of design techniques which could used in the design of very flexible aircraft with large slender wings. They found that the deformed aircraft geometry should be used in weight, structural and stability analyses. They also demonstrated that the coupling between aeroelastic and flight dynamic modes could not be neglected. Finally, they showed that time domain simulations should include the nonlinear displacements of the aircraft, and that while linear models may be

used to obtain stability characteristics they are too conservative for critical loadings, such as gust response

Hesse and Palacios [9], [10] proposed a balanced model reduction approach of the aeroelastic framework for simulating the dynamics of very flexible aircraft. This method calculates aerodynamic loads using a three-dimensional vortex lattice method which is linearized about the trimmed flight condition and assumes small wing deformations. The structural degrees of freedom were linearized so that the nonlinear flexible body dynamics could be projected on the dominant vibration modes of the unconstrained structure while maintaining all of the gyroscopic effect terms.

1.1.2 Gust Load Alleviation

Mclean [11] presented multiple control schemes for alleviating gusts loads on deformable aircraft. Output feedback control laws are used because, in general, not all states are available as measured outputs. The author points out that one difficulty in designing gust load alleviation control laws is that the aircraft are modeled using a system of ordinary differential equations, but that partial differential equations are more accurate due to the flexible aircraft behaving more like an infinite-dimensional system as opposed to a finite-dimensional lumped parameter system. He showed significant reductions in vertical acceleration at specific body locations using a linear quadratic based controller as well as a controller based on model matching.

Botez, Boustani, Vayani, Bigras and Wong [12] performed a study of gust load alleviation (GLA) techniques on a flexible B-52 model. A reduction in the Power Spectral Density (PSD) of the aircraft vertical acceleration during an encounter with a stochastic gust disturbance was demonstrated when a Linear Quadratic Gaussian (LQG) controller was added to the open loop system.

Shao, Wu, Yang, Chen and Lu [13] designed an adaptive GLA control system based on fuzzy logic. The controller was demonstrated on a large aspect ratio wing with two control

surfaces. The model was subjected to both sinusoidal and stochastic gust disturbances. A reduction of up to 27% in vertical acceleration measured at the wing tip was achieved. This method was also tested in a wind tunnel with good agreement shown between experimental and simulation results.

Rui, Xiaoping and Zhou [14] created a GLA controller for a large solar powered unmanned aerial vehicle (UAV). A static output feedback control law with a quadratic performance index was developed using linearized equations of motion. The UAV was given a vertical "1-cos" gust disturbance and the vertical displacement of the wing mid-span and tips, as well as their rates, were fed back for control. This approach showed a 33% reduction in wing tip deflection during the gust encounter.

Haghighat, Liu and Martins [15] presented a model-predictive controller (MPC) formulation for GLA on the VFA aircraft model previously studied in [16], [17] and [7]. Linear simulations were accomplished with discrete and continuous gust disturbances added to the system. The authors also compared traditional linear quadratic controllers to the newly formulated MPC controller. They showed that the MPC controller performed better at reducing stresses on the aircraft induced by the gust than the LQ controller. Additionally, they found that the inclusion of either GLA controller also resulted in smaller perturbations of the rigid body states during gust encounter.

1.1.3 Very Flexible Aircraft Control

Shearer [17] and Shearer and Cesnik [16], [7] studied nonlinear dynamics and control of VFA. They developed a two-loop control architecture to control the trajectory of a simplified VFA model which captured the unstable phugoid mode, but failed to exhibit the large wing deformations often present in VFA aircraft models. The outer loop was based on a heuristic mimicking the actions of a human pilot. The inputs to the outer loop are flight path angle and roll angle, which are then passed through a proportional, integral, derivative (PID) controller and converted to body frame velocities and angular rates. They showed

that, with appropriate eigenvalue decoupling of the aircraft linearization, the lateral and longitudinal inner loop controllers could be designed independently of each other. A dynamic inversion controller for longitudinal modes in the inner loop was designed and when coupled with the outer loop controller provided good tracking of altitude change commands. The lateral motion was found to be coupled with the elastic states, and therefore acceptable tracking of lateral commands using an LQR inner loop controller was only achieved when the elastic states were fed back.

Gibson, Annaswamy and Lavretsky [18] compared a linear LQR/LTR controller with an adaptive LQR/LTR controller for stabilization of a VFA model. The unstable phugoid mode was excited by giving the aircraft a dihedral angle initial condition differing from the trim value and then using the controller to return the aircraft to trim. They showed that the linear LQR/LTR could not return the aircraft to the initial trim state, while the adaptive LQR/LTR could.

Cesnik, Ortega-Morales and Patil [19] studied the aeroelastic performance of highly-flexible active composite wings. An LQG controller was used to control anisotropic strain actuation. Careful placement of the embedded actuators and orientation of the electric field profile led to successful control of the aeroelastic instabilities as well as GLA.

Patil and Hodges [20] presented a static output feedback (SOF) design for a nonlinear aeroelastic system. The controllers were designed for flutter suppression as well as gust alleviation. The choice of sensors and sensor placement was found to be directly tied to controller performance. Twist and twist rate were shown to be most important for flutter suppression while root curvature was the most important for GLA. The SOF controller performance was also compared to that of a full-state feedback LQR. The SOF flutter suppression controller was found to have similar gain and phase margins to the LQR controller. An LQR with knowledge of the gust states was found to have the best GLA performance, however a full state LQR with no knowledge of the gust states was shown to have similar GLA performance as the SOF controller.

Che, Gregory and Cao presented an LQG controller augmented with an L_1 adaptive output feedback control scheme. A semi-span wind tunnel model capable of pitch and plunge is used. The control objective is to track a pitch command with altitude hold while suppressing body freedom flutter. The LQG controller is designed at a nominal dynamic pressure and then the model is tested at multiple off-nominal dynamic pressures. The adaptive control loop is able to successfully account for the parameter variations due to the change in dynamic pressure, and is able to stabilize the model at dynamic pressures above the open-loop flutter boundary.

Raghavan and Patil [21] developed a controller for a VFA flying wing model to match a turning trajectory. The mean axis concept is used to create a reduced order model which minimizes coupling between the rigid body dynamics and the elastic modes. The reduced order model is used to design a multi-step nonlinear dynamic inversion controller. This controller, along with a nonlinear guidance law, is able to successful guide the aircraft model to follow a curved ground path.

Cook, Palacios and Goulart [22] studied GLA and stabilization of a VFA model. A reduced order, linearized model was obtained by linearizing the nonlinear VFA equations of motion and then applying the balanced truncation method. An H_∞ controller was designed using this reduced order model. The controller was able to reduce the root curvature values on a linear model, which are related to bending moments, by 9% incurred as a result of a discrete gust occurring at the worst case gust length. The controller also performed comparably in nonlinear simulations on the worst-case gust, but as the gust length was increased, the frequency of the gust excitation approach the phugoid mode frequency, which led to difficulties for the controller.

Wang, Wynn and Palacios [23] formulated a robust controller using intrinsic variables on a large flexible wing model. They achieved a 7.9% reduction in maximum root bending moment caused by a gust disturbance using a linear H_∞ controller. The controller was also able to increase the flutter velocity when comapred to the open loop system.

1.2 Dissertation Outline

There are many goals and objectives of this dissertation. The first is to characterize the open and closed loop dynamics of VFA aircraft, and to relate these characteristics to aircraft stiffness and flight dynamic properties. The next objective is to demonstrate a stable and effective control architecture capable of tracking longitudinal and lateral commands in the presence of various gust disturbances. Finally, this dissertation will present multiple strategies for minimizing VFA loads caused by gust disturbances and aircraft maneuvers. The dissertation is organized as follows:

In Chapter 2 the theoretical background is presented. An overview of the aeroelastic governing equations as well as the equations of motion is shown. The numerical integration scheme used to time march the equations is described. The various models for representing the gust are described. Finally, a description of the computer framework used in this study is given.

Chapter 3 presents a study on the open loop gust response sensitivity of VFA. The stiffness properties of two baseline VFA models are varied to create multiple aircraft with equivalent inertia and geometric properties, but with different flexibilities. These aircraft models are then subjected to time-varying gust disturbances. The responses are then analyzed and trends identified.

Chapter 4 formulates a control architecture including a new method for calculating a desired VFA trajectory. Longitudinal control is first demonstrated on an altitude change command in still air, with two outer loop controllers presented to replace a PID controller shown to be unstable. A lateral control scheme is then introduced to track commanded roll and yaw angles, which is designed using only a subset of the elastic states. Then, the same commands are matched in the presence of various gust disturbances.

In Chapter 5, a method for minimizing aircraft loads during an encounter with a gust disturbance is developed, which relies on coordinated aileron commands. The bending moment of the aircraft model is shown to be proportional to the curvature of the wing. The

curvature of the wing is then controlled, thereby minimizing the bending moment induced on VFA by controlling the shape of the aircraft. A method for enforcing limits on wing curvature values by modifying the set point to the closed loop system is also demonstrated.

Finally, Chapter 6 summarizes the current work and presents the main conclusions. The key contributions of this dissertation are also summarized. Finally, recommendations for future work are given.

CHAPTER 2

Theoretical Background

This chapter presents the theoretical background needed for this work. An overview of the coupled aeroelastic and rigid body equations of motion is given. Then, an introduction to the aircraft trimming and linearization of the equations of motion is presented. Next, the various wind gust models used in this study are described. Finally, the numerical implementation methods are presented.

2.1 Coupled Aeroelastic and Rigid Body Equations

The coupled nonlinear aeroelastic and rigid body equations of motion (EOM) were developed by Cesnik and co-workers, with the details documented in [1], [16], [7], [17], [24], [25] [26], [27], and [28]. Shearer and Cesnik [16] state three typical assumptions normally made in the formulation of rigid-body aircraft EOM which are invalid for VFA in general: 1) inertia properties are constant or slowly time-varying, 2) the inertial force due a coupling of the rotating coordinate frame and relative velocity of flexible members is negligible, and 3) external forces and moments resulting from aerodynamic loading are based on a fixed aircraft geometry.

The coupled aeroelastic and rigid-body EOM used in this study are derived using the Principle of Virtual Work and the variation of the energy functional [16]. The EOM take the standard form of:

$$M\ddot{q} + C\dot{q} + Kq = R(q, \dot{q}) \tag{2.1}$$

$$q = \begin{bmatrix} \varepsilon \\ b \end{bmatrix}, \dot{q} = \begin{bmatrix} \dot{\varepsilon} \\ \beta \end{bmatrix}, \dot{q} = \begin{bmatrix} \ddot{\varepsilon} \\ \dot{\beta} \end{bmatrix} \tag{2.2}$$

where ε is the element strain, b is the position vector of the body-fixed frame in relation to an inertial frame, β is the velocity of the body frame, consisting of the translational and rotational velocities, M is the generalized mass matrix, C is the generalized damping matrix, K is the generalized stiffness matrix and R is the state-dependent generalized force vector.

The elastic deformation of the wing is determined by modeling the wing using nonlinear beam elements. Each of the beam elements has four degrees of freedom and three nodes. The four degrees of freedom for the ith element along the wing are given by:

$$\varepsilon_i = \begin{bmatrix} \varepsilon_x \\ \kappa_x \\ \kappa_y \\ \kappa_z \end{bmatrix} \tag{2.3}$$

where ε_x is the extensional strain, κ_x is the beam twist, and κ_y and κ_z are the curvatures about the y and z axes, respectively.

The total virtual work on the system is found by summing the internal work, δW_{int}, and external work, δW_{ext}, for all the elements and adding the contribution of the rigid elements,

δW_{RB}. This yields:

$$
\begin{aligned}
\delta W &= \delta W_{RB} + \sum (-\delta W_{int} + \delta W_{ext}) \\
&= \begin{bmatrix} \delta\varepsilon^T & \delta b^T \end{bmatrix} (- \begin{bmatrix} J_{h\varepsilon}^T M J_{h\varepsilon} & J_{h\varepsilon}^T M J_{hb} \\ J_{hb}^T M J_{h\varepsilon} & J_{hb}^T M J_{hb} \end{bmatrix} \begin{bmatrix} \ddot{\varepsilon} \\ \dot{\beta} \end{bmatrix} - \begin{bmatrix} 0 & 0 \\ 0 & M_{RB} \end{bmatrix} \begin{bmatrix} \ddot{\varepsilon} \\ \dot{\beta} \end{bmatrix} \\
&- \begin{bmatrix} J_{h\varepsilon}^T M \dot{J}_{h\varepsilon} & 0 \\ J_{hb}^T M \dot{J}_{h\varepsilon} & 0 \end{bmatrix} \begin{bmatrix} \dot{\varepsilon} \\ \beta \end{bmatrix} - \begin{bmatrix} 0 & J_{h\varepsilon}^T M H_{hb} \\ 0 & J_{hb}^T M H_{hb} \end{bmatrix} \begin{bmatrix} \dot{\varepsilon} \\ \beta \end{bmatrix} - \begin{bmatrix} 0 & J_{h\varepsilon}^T M \dot{J}_{hb} \\ 0 & J_{hb}^T M \dot{J}_{hb} \end{bmatrix} \begin{bmatrix} \dot{\varepsilon} \\ \beta \end{bmatrix} \\
&- \begin{bmatrix} C & 0 \\ 0 & 0 \end{bmatrix} \begin{bmatrix} \dot{\varepsilon} \\ \beta \end{bmatrix} - \begin{bmatrix} 0 & 0 \\ 0 & C_{RB} \end{bmatrix} \begin{bmatrix} \dot{\varepsilon} \\ \beta \end{bmatrix} - \begin{bmatrix} K & 0 \\ 0 & 0 \end{bmatrix} \begin{bmatrix} \varepsilon \\ b \end{bmatrix} + \begin{bmatrix} K\varepsilon^0 \\ R_{RB}^{ext} \end{bmatrix} \\
&+ \begin{bmatrix} J_{h\varepsilon}^T \\ J_{hb}^T \end{bmatrix} Ng + \begin{bmatrix} J_{p\varepsilon}^T \\ J_{pb}^T \end{bmatrix} B^F F^{dist} + \begin{bmatrix} J_{\Theta\varepsilon}^T \\ J_{\Theta b}^T \end{bmatrix} B^M M^{dist} \\
&+ \begin{bmatrix} J_{p\varepsilon}^T \\ J_{pb}^T \end{bmatrix} F^{pt} + \begin{bmatrix} J_{\Theta\varepsilon}^T \\ J_{\Theta b}^T \end{bmatrix} M^{pt})
\end{aligned}
\tag{2.4}
$$

where $J_{h\varepsilon}$, $J_{p\varepsilon}$, $J_{\Theta\varepsilon}$, J_{hb}, J_{pb}, and $J_{\Theta b}$ are the Jacobian matrices relating displacements (h in body frame and p in inertial frame) and rotations (Θ) to the independent variables ε and b (the position and orientation of the body fixed frame), H_{hb} is a matrix consisting of influence from Jacobian and body angular velocities, N is the gravity influence matrix, g is gravity acceleration, B^F and B^M are the distributed force and moment influence matrices, F^{dist} and M^{dist} are the distributed force and moments (which include aerodynamic loads), F^{pt} and M^{pt} are point forces and moments and ε^0 is the initial strain vector. A detailed derivation of the Jacobians and influence matrices can be found in [25] and [17]. Additionally, the notation used for the Jacobian definition is:

$$
J_{h\varepsilon} = \frac{\partial h}{\partial \varepsilon} \tag{2.5}
$$

The EOM are then determined by setting the virtual work to zero. The variation of $[\delta\varepsilon \ \delta b]$ is arbitrary which, after re-arranging the terms, leads to:

$$\begin{bmatrix} M_{FF} \ M_{FB} \\ M_{BF} \ M_{BB} \end{bmatrix} \begin{bmatrix} \ddot{\varepsilon} \\ \dot{\beta} \end{bmatrix} + \begin{bmatrix} C_{FF} \ C_{FB} \\ C_{BF} \ C_{BB} \end{bmatrix} \begin{bmatrix} \dot{\varepsilon} \\ \beta \end{bmatrix} + \begin{bmatrix} K_{FF} \ 0 \\ 0 \quad 0 \end{bmatrix} \begin{bmatrix} \varepsilon \\ b \end{bmatrix} = \begin{bmatrix} R_F \\ R_B \end{bmatrix} \tag{2.6}$$

where

$$M_{FF}(\varepsilon) = J_{h\varepsilon}^T M J_{h\varepsilon} \tag{2.7}$$

$$M_{FB}(\varepsilon) = J_{h\varepsilon}^T M J_{hb} \tag{2.8}$$

$$M_{BF}(\varepsilon) = J_{hb}^T M J_{h\varepsilon} \tag{2.9}$$

$$M_{BB}(\varepsilon) = J_{hb}^T M J_{hb} + M_{RB} \tag{2.10}$$

$$C_{FF}(\varepsilon, \dot{\varepsilon}, \beta) = C + J_{h\varepsilon}^T M \dot{J}_{h\varepsilon} \tag{2.11}$$

$$C_{FB}(\varepsilon, \dot{\varepsilon}, \beta) = J_{h\varepsilon}^T M H_{hb} + 2 J_{h\varepsilon}^T M \dot{J}_{hb} \tag{2.12}$$

$$C_{BF}(\varepsilon, \dot{\varepsilon}, \beta) = J_{h\varepsilon}^T M \dot{J}_{h\varepsilon} \tag{2.13}$$

$$C_{BB}(\varepsilon, \dot{\varepsilon}, \beta) = J_{hb}^T M H_{hb} + 2 J_{hb}^T M \dot{J}_{hb} + C_{RB} \tag{2.14}$$

$$K_{FF} = K \tag{2.15}$$

where M, C, and K represent, respectively, the assembled flexible element generalized mass, damping and stiffness matrices, and M_{RB} and C_{RB} represent the mass and damping matrices for the B frame element [16].

$$\begin{bmatrix} R_F \\ R_B \end{bmatrix} = \begin{bmatrix} J_{h\varepsilon}^T \\ J_{hb}^T \end{bmatrix} Ng + \begin{bmatrix} J_{p\varepsilon}^T \\ J_{pb}^T \end{bmatrix} B^F F^{dist} + \begin{bmatrix} J_{\Theta\varepsilon}^T \\ J_{\Theta b}^T \end{bmatrix} B^M M^{dist} + \begin{bmatrix} J_{p\varepsilon}^T \\ J_{pb}^T \end{bmatrix} F^{pt} + \begin{bmatrix} J_{\Theta\varepsilon}^T \\ J_{\Theta b}^T \end{bmatrix} M^{pt} \tag{2.16}$$

The body-fixed, B, reference frame is propagated using first-order quaternion differen-

tial equations which are presented in [29] and [7]:

$$\begin{bmatrix} \dot{\zeta}_0 \\ \dot{\zeta}_1 \\ \dot{\zeta}_2 \\ \dot{\zeta}_3 \end{bmatrix} = -\frac{1}{2} \begin{bmatrix} 0 & \omega_{B1} & \omega_{B2} & \omega_{B3} \\ -\omega_{B1} & 0 & -\omega_{B3} & \omega_{B2} \\ -\omega_{B2} & \omega_{B3} & 0 & -\omega_{B1} \\ -\omega_{B3} & -\omega_{B2} & \omega_{B1} & 0 \end{bmatrix} \begin{bmatrix} \zeta_0 \\ \zeta_1 \\ \zeta_2 \\ \zeta_3 \end{bmatrix} \equiv -\frac{1}{2} \Omega_\zeta (\beta) \zeta \tag{2.17}$$

where ω_{Bi} is the i-th component of the angular velocity. The B frame inertial velocity is given by:

$$\dot{p}_B = C^{GB} v_B \tag{2.18}$$

where C^{GB} is the transformation matrix from the B frame to the inertial frame G, whose representation in terms of the quaternions is:

$$C^{GB} = \begin{bmatrix} \zeta_0^2 + \zeta_1^2 - \zeta_2^2 - \zeta_3^2 & 2(\zeta_1\zeta_2 - \zeta_0\zeta_3) & 2(\zeta_1\zeta_3 - \zeta_0\zeta_2) \\ 2(\zeta_1\zeta_2 - \zeta_0\zeta_3) & \zeta_0^2 - \zeta_1^2 + \zeta_2^2 - \zeta_3^2 & 2(\zeta_2\zeta_3 - \zeta_0\zeta_1) \\ 2(\zeta_1\zeta_3 - \zeta_0\zeta_2) & 2(\zeta_2\zeta_3 - \zeta_0\zeta_1) & \zeta_0^2 - \zeta_1^2 - \zeta_2^2 + \zeta_3^2 \end{bmatrix} \tag{2.19}$$

2.1.1 Unsteady Aerodynamic Loads

The unsteady aerodynamic formulation used in this study is taken from [25] and uses the finite-state inflow method of [30]. The aerodynamic forces are calculated on a thin airfoil section possibly undergoing large motion in an incompressible flow. A Prandtl-Glauert correction factor can then be added if compressibility effects are needed. The velocity components are shown in Fig. 2.1. The aerodynamic loads calculated at the mid-

chord are then:

$$l_{mc} = \pi\rho b_c^2\left(-\ddot{z} + \dot{y}\dot{\alpha} - d\ddot{\alpha}\right) + 2\pi\rho b_c\dot{y}^2\left[-\frac{1}{2} + \left(\frac{1}{2}b_c - d\right)\frac{\dot{\alpha}}{\dot{y}} - \frac{\lambda_0}{\dot{y}}\right] + 2\pi\rho b_c c_1\dot{y}^2\delta \tag{2.20}$$

$$m_{mc} = 2\pi\rho b_c^2\left(-\frac{1}{2}\dot{y}\dot{z} - \frac{1}{2}d\dot{y}\dot{\alpha} - \frac{1}{2}\dot{y}\lambda_0 - \frac{1}{16}b_c^2\ddot{\alpha}\right) + 2\pi\rho b_c^2 c_4\dot{y}^2\delta \tag{2.21}$$

$$\begin{aligned} d_{mc} = {} & -2\pi\rho b_c\left(\dot{z}^2 + d^2\alpha^2 + \lambda_0^2 + 2d\dot{\alpha}\dot{z} + 2\lambda_0\dot{z} + 2d\dot{\alpha}\lambda_0\right) \\ & - 2\pi\rho b_c\left[c_1\dot{y}\dot{z}\delta + \left(dc_1 + b_c g_2\right)\dot{y}\dot{\alpha}\delta + c_1\dot{y}\lambda_0\delta + \frac{1}{2}b_c g_2\ddot{z}\delta + \left(\frac{1}{2}b_c d g_2 - \frac{1}{4}b_c^2 g_3\right)\ddot{\alpha}\delta\right] \end{aligned} \tag{2.22}$$

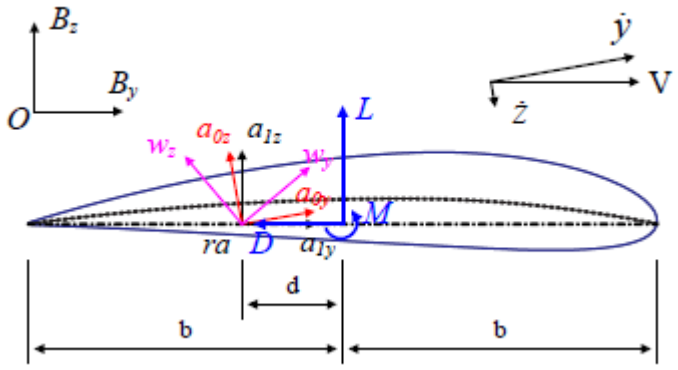

Figure 2.1: Airfoil coordinate system and velocity components [25]

where b_c is the semichord, d is the distance from the beam reference axis to the mid-chord, $-\dot{z}/\dot{y}$ is the total angle of attack and includes both the steady-state angle of attack as well as the angle of attack induced by the plunging motion of the airfoil, δ is the trailing-edge control surface deflection, c_i and g_i are parameters based on geometry with details provided in [24] and [30]. The inflow parameter, λ_0, accounts for the induced flow caused by the

wake vorticity, which is the summation of finite inflow states, λ, given by [30]:

$$\begin{aligned}\dot{\lambda} &= F_1\ddot{q} + F_2\dot{q} + F_3\lambda \\ &= F_1\begin{bmatrix}\ddot{\varepsilon}\\ \dot{\beta}\end{bmatrix} + F_2\begin{bmatrix}\dot{\varepsilon}\\ \beta\end{bmatrix} + F_3\lambda\end{aligned} \tag{2.23}$$

where F_1, F_2, and F_3 can be found in [30].

The aerodynamic formulation above assumes a thin airfoil with no camber and an aerodynamic moment coefficient, c_{m0} of zero. This can be generalized for a user-supplied aerodynamic coefficients. The aerodynamic loads at the airfoil's aerodynamic center are given by:

$$l_{ac} = \pi\rho b_c^2\left(-\ddot{z} + \dot{\alpha} - d\ddot{\alpha}\right) + c_{l\alpha}\rho b\dot{y}^2\left[-\frac{\dot{z}}{\dot{y}} + \left(\frac{1}{2}b_c - d\right)\frac{\dot{\alpha}}{\dot{y}} - \frac{\lambda_0}{\dot{y}}\right] + \rho b\dot{y}^2 c_{l\delta} \tag{2.24}$$

$$m_{ac} = \pi\rho b_c^3\left[\frac{1}{2}\ddot{z} - \dot{y}\dot{\alpha} - \left(\frac{1}{8}b_c - \frac{1}{2}d\right)\ddot{\alpha}\right] + 2\rho b_c^2\dot{y}^2\left(c_{m0} + c_{m\delta}\delta\right) \tag{2.25}$$

$$d_{ac} = -\rho b_c\dot{y}^2 c_{d0} \tag{2.26}$$

where $c_{l\alpha}$ is the lift curve slope, $c_{l\delta}$ and $c_{m\delta}$ are the lift and moment slopes due to a control surface deflection, and c_{d0} and c_{m0} are the zero angle of attack drag and moment coefficients, respectively.

To transfer the aerodynamic loads from the mid-chord or the aerodynamic center to the reference axis, the following equations can be used:

a) Mid-chord to beam reference axis:

$$l_{ra} = l_{mc} \tag{2.27}$$

$$m_{ra} = m_{mc} + dl_{mc} \tag{2.28}$$

$$d_{ra} = d_{mc} \tag{2.29}$$

b) Aerodynamic center (quarter-chord) to beam reference axis:

$$l_{ra} = l_{ac} \tag{2.30}$$

$$m_{ra} = m_{ac} + \left(\frac{1}{2}b_c + d\right) l_{ac} \tag{2.31}$$

$$d_{ra} = d_{ac} \tag{2.32}$$

Finally, the loads are transformed to the B frame using the transformation matrix C^{Ba_1} by use of:

$$F^{aero} = C^{Ba_1} \begin{bmatrix} 0 \\ d_{ra} \\ l_{ra} \end{bmatrix}, \quad M^{aero} = C^{Ba_1} \begin{bmatrix} m_{ra} \\ 0 \\ 0 \end{bmatrix} \tag{2.33}$$

2.1.2 Final EOM

The complete governing set of coupled equations of motion is then given by:

$$M_{FF}\ddot{\varepsilon} = -M_{FB}\dot{\beta} - C_{FF}\dot{\varepsilon} - C_{FB}\beta - K_{FF}\varepsilon + R_F \tag{2.34}$$

$$M_{BB}\dot{\beta} = -M_{BF}\ddot{\varepsilon} - C_{BB}\beta - C_{BF}\dot{\varepsilon} + R_B \tag{2.35}$$

$$\dot{\zeta} = -\frac{1}{2}\Omega_\zeta \zeta \tag{2.36}$$

$$\dot{p}_B = \begin{bmatrix} C^{BG} & 0 \end{bmatrix} \beta \tag{2.37}$$

$$\dot{\lambda} = F_1 \begin{bmatrix} \ddot{\varepsilon} \\ \dot{\beta} \end{bmatrix} + F_2 \begin{bmatrix} \dot{\varepsilon} \\ \beta \end{bmatrix} + F_3\lambda \tag{2.38}$$

with the aerodynamic forces and moments included in the generalized forces, R_F and R_B, as distributed forces and moments.

Various improvements and additions to the fundamental governing equations of motion have been made and can be found in [25] and [17]. These additions include absolute and relative constraints, rigid bodies attached to flexible members, skin wrinkling, and simpli-

fied stall models.

2.2 Aircraft Trimming

The aircraft is trimmed based on the thrust required for 1-g level flight using a method developed in [16] based upon techniques in [29] and [31]. A cost function is defined as:

$$J = f^T \cdot f \tag{2.39}$$

The function f is defined using either the B frame linear and angular accelerations or using the aerodynamic forces of lift, pitching moment about the center of gravity, and drag:

$$f = \begin{bmatrix} \dot{v}_{By} \\ \dot{v}_{Bz} \\ \dot{\omega}_x \end{bmatrix}, \quad \text{or} \quad f = \begin{bmatrix} L \\ M_{x,cg} \\ D \end{bmatrix} \tag{2.40}$$

A zero of the cost function, J, is then found using the body angle of attack, α, elevator deflection angle, δ_e, and the thrust, δ_t, as the inputs. The Newton-Raphson method is used to find the local root of the search variable:

$$\Delta S_k = -\left[\frac{\partial f}{\partial S}\right]_k^{-1} f_k \tag{2.41}$$

where

$$S_k = \begin{bmatrix} \delta_e \\ \alpha \\ \delta_t \end{bmatrix}_k \tag{2.42}$$

The next iteration of the search variable is found via:

$$S_{k+1} = S_k + \Delta S_k \tag{2.43}$$

and Eqs. 2.41 and 2.42 are recomputed using S_{k+1}. Equations 2.41 and 2.42 are then iterated until the cost function J is smaller than a user-defined tolerance. To prevent divergence, S_{k+1} is constrained at every iteration to fall within prescribed bounds, with the Jacobian:

$$J_f = \frac{\partial f}{\partial S} \tag{2.44}$$

calculated numerically. A flowchart for the trim routine is shown in Fig. 2.2.

2.2.1 Linearization of Governing Equations

The method for linearizing the equations of motion was developed in [25] and is summarized here. The complete set of equations of motion is given in Eqs. 2.34 - 2.38.The aircraft is in free flight, therefore only aerodynamic, gravity and thrust forces are applied to the system, which are given by:

$$R_F = R_F^{aero}\left(\ddot{\varepsilon}, \dot{\varepsilon}, \varepsilon, \dot{\beta}, \beta, \lambda\right) + R_F^{grav}\left(\zeta\right) + R_F^{thrust} \tag{2.45}$$

$$R_B = R_B^{aero}\left(\ddot{\varepsilon}, \dot{\varepsilon}, \varepsilon, \dot{\beta}, \beta, \lambda\right) + R_B^{grav}\left(\zeta\right) + R_B^{thrust} \tag{2.46}$$

where R_F^{grav} and R_B^{grav} are the flexible and rigid body components of the generalized gravity force, and R_F^{thrust} and R_B^{thrust} are the flexible and rigid body components of the generalized thrust force.

The linearization of Eqs. 2.34 - 2.38 is performed about a trim point, with the trim value of the state variables given by $[\dot{\varepsilon}_0 \;\; \varepsilon_0 \;\; \beta_0 \;\; \zeta_0 \;\; p_{B0} \;\; \lambda_0]^T$, yielding:

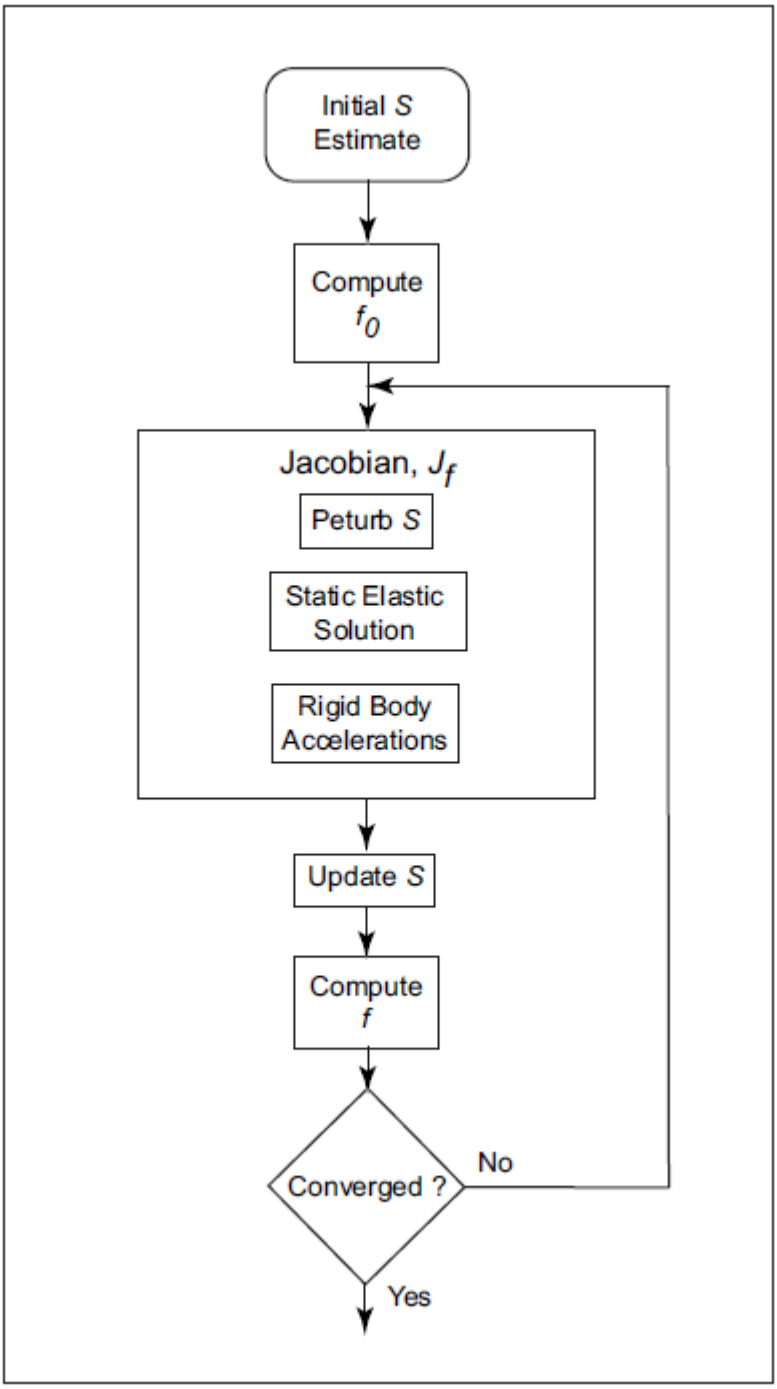

Figure 2.2: Trim solution flow [16]

$$M_{FF}\ddot{\varepsilon} + M_{FB}\dot{\beta} + \left(C_{FF} + C_{FF/\dot{\varepsilon}_0}\dot{\varepsilon}_0 + C_{FB/\dot{\varepsilon}_0}\dot{\beta}_0\right)\dot{\varepsilon} \tag{2.47}$$

$$+ \left(C_{FB} + C_{FF/\beta_0}\dot{\varepsilon}_0 + C_{FB/\beta_0}\beta_0\right)\beta + K_{FF}\varepsilon \tag{2.48}$$

$$= R^{aero}_{F/\ddot{\varepsilon}_0}\ddot{\varepsilon} + R^{aero}_{F/\dot{\varepsilon}_0}\dot{\varepsilon} + R^{aero}_{F/\varepsilon_0}\varepsilon + R^{aero}_{F/\dot{\beta}_0}\dot{\beta} + R^{aero}_{F/\beta_0}\beta + R^{aero}_{F/\lambda_0}\lambda + R^{grav}_{F/\zeta_0}\zeta \tag{2.49}$$

$$M_{BF}\ddot{\varepsilon} + M_{BB}\dot{\beta} + \left(C_{BF} + C_{BF/\dot{\varepsilon}_0}\dot{\varepsilon}_0 + C_{BB/\dot{\varepsilon}_0}\dot{\beta}_0\right)\dot{\varepsilon} \tag{2.50}$$

$$+ \left(C_{BB} + C_{BF/\beta_0}\dot{\varepsilon}_0 + C_{FB/\beta_0}\beta_0\right)\beta \tag{2.51}$$

$$= R^{aero}_{B/\ddot{\varepsilon}_0}\ddot{\varepsilon} + R^{aero}_{B/\dot{\varepsilon}_0}\dot{\varepsilon} + R^{aero}_{B/\varepsilon_0}\varepsilon + R^{aero}_{B/\dot{\beta}_0}\dot{\beta} + R^{aero}_{B/\beta_0}\beta + R^{aero}_{B/\lambda_0}\lambda + R^{grav}_{B/\zeta_0}\zeta \tag{2.52}$$

$$\dot{\zeta} = -\frac{1}{2}\Omega_{\zeta}\zeta - \frac{1}{2}\Omega_{\zeta/\beta_0}\zeta_0 \tag{2.53}$$

$$\dot{p}_B = \begin{bmatrix} C^{GB} & 0 \end{bmatrix}\beta + \begin{bmatrix} C_{\zeta_0^{GB}}\zeta & 0 \end{bmatrix}\beta_0 \tag{2.54}$$

$$\dot{\lambda} = F_1 \begin{bmatrix} \ddot{\varepsilon} \\ \dot{\beta} \end{bmatrix} + F_2 \begin{bmatrix} \dot{\varepsilon} \\ \beta \end{bmatrix} + F_3\lambda \tag{2.55}$$

where $(\bullet)_{/x_0}$ denotes $\frac{\partial(\bullet)}{\partial x}|_{x0}$.

The linearized equations are then transformed into state-space form given by:

$$\begin{bmatrix} \ddot{\varepsilon} & \dot{\varepsilon} & \dot{\beta} & \dot{\zeta} & \dot{p}_B & \dot{\lambda} \end{bmatrix}^T = Q_1^{-1}Q_2 \begin{bmatrix} \dot{\varepsilon} & \varepsilon & \beta & \zeta & p_B & \lambda \end{bmatrix} \tag{2.56}$$

$$= A \begin{bmatrix} \dot{\varepsilon} & \varepsilon & \beta & \zeta & p_B & \lambda \end{bmatrix} \tag{2.57}$$

where

$$Q_1 = \begin{bmatrix} I & 0 & 0 & 0 & 0 & 0 \\ 0 & \overline{M}_{FF} & \overline{M}_{FB} & 0 & 0 & 0 \\ 0 & \overline{M}_{BF} & \overline{M}_{BB} & 0 & 0 & 0 \\ 0 & 0 & 0 & I & 0 & 0 \\ 0 & 0 & 0 & 0 & I & 0 \\ 0 & -F_{1F} & -F_{1B} & 0 & 0 & I \end{bmatrix} \tag{2.58}$$

$$Q_2 = \begin{bmatrix} 0 & I & 0 & 0 & 0 & 0 \\ -\overline{K}_{FF} & \overline{C}_{FF} & \overline{C}_{FB} & R^{grav}_{F/\zeta_0} & 0 & R^{aero}_{F/\lambda_0} \\ 0 & \overline{C}_{BF} & \overline{C}_{BB} & R^{grav}_{B/\zeta_0} & 0 & R^{grav}_{B/\zeta_0} \\ 0 & 0 & -\frac{1}{2}\Omega_{\zeta/\beta_0}\zeta_0 & -\frac{1}{2}\Omega & 0 & 0 \\ 0 & 0 & \begin{bmatrix} C^{GB} & 0 \end{bmatrix} & \begin{bmatrix} C^{GB}_{\zeta_0} & 0 \end{bmatrix}\beta_0 & 0 & 0 \\ 0 & F_{2F} & F_{2B} & 0 & 0 & F_3 \end{bmatrix} \tag{2.59}$$

and

$$\overline{M}_{FF} = M_{FF} - R^{aero}_{F/\ddot{\varepsilon}_0} \tag{2.60}$$

$$\overline{M}_{BF} = M_{BF} - R^{aero}_{B/\ddot{\varepsilon}_0} \tag{2.61}$$

$$\overline{M}_{FB} = M_{FB} - R^{aero}_{F/\ddot{\beta}_0} \tag{2.62}$$

$$\overline{M}_{BB} = M_{BB} - R^{aero}_{B/\ddot{\beta}_0} \tag{2.63}$$

$$\overline{C}_{FF} = C_{FF} + C_{FF/\dot{\varepsilon}_0}\dot{\varepsilon}_0 + C_{FB/\dot{\varepsilon}_0}\dot{\beta}_0 - R^{aero}_{F/\dot{\varepsilon}_0} \tag{2.64}$$

$$\overline{C}_{BF} = C_{BF} + C_{BF/\dot{\varepsilon}_0}\dot{\varepsilon}_0 + C_{BB/\dot{\varepsilon}_0}\dot{\beta}_0 - R^{aero}_{B/\dot{\varepsilon}_0} \tag{2.65}$$

$$\overline{C}_{FB} = C_{FB} + C_{FF/\dot{\beta}_0}\dot{\varepsilon}_0 + C_{FB/\dot{\beta}_0}\dot{\beta}_0 - R^{aero}_{F/\dot{\beta}_0} \tag{2.66}$$

$$\overline{C}_{BB} = C_{BB} + C_{BF/\dot{\beta}_0}\dot{\varepsilon}_0 + C_{BB/\dot{\beta}_0}\dot{\beta}_0 - R^{aero}_{B/\dot{\beta}_0} \tag{2.67}$$

$$\overline{K}_{FF} = K_{FF} - R^{aero}_{F/\varepsilon_0} \tag{2.68}$$

The control effector matrix, B, is then found to be:

$$B = Q_1^{-1}Q_3 \tag{2.69}$$

where

$$Q_3 = \begin{bmatrix} 0 & 0 \\ B_{\delta F} & B_{TF} \\ B_{\delta B} & B_{TB} \\ 0 & 0 \\ 0 & 0 \\ 0 & 0 \end{bmatrix} \tag{2.70}$$

where $B_{\delta F}$ and $B_{\delta B}$ are the elastic and rigid body contributions due to control surface deflections and B_{TF} and B_{TB} are the elastic and rigid body contributions due to thrust forces. All four of these terms are derived in Appendix B.

In a similar manner, the gust effector matrix, B_w, is given by:

$$B_w = Q_1^{-1} Q_4 \tag{2.71}$$

where

$$Q_4 = \begin{bmatrix} 0 \\ B_w F \\ B_w B \\ 0 \\ 0 \\ 0 \end{bmatrix} \tag{2.72}$$

and $B_w F$ and $B_w B$ are derived in Appendix B.

2.2.2 Numerical Integration Scheme

The coupled first- and second-order nonlinear differential equations of motion, Eqs. 2.34 - 2.38, are integrated in time using the implicit Modified Newmark Method developed in [32], where details can be found. The method uses the Newmark integration scheme,

with the selection of the numerical tuning parameters based upon first- and second- order Generalized-α methods. This scheme possesses long term integration stability and good computational performance when used on large nonlinear elastic systems with augmented rigid-body motion and aeroelastic interaction [32].

The Newmark method [33] is an integration scheme originally developed for use in structural response to an earthquake. The scheme is designed to provide numerical damping for second order linear time invariant (LTI) systems of the form:

$$Ma + Cv + Kd = F \tag{2.73}$$

where M, C, and K are the generalized mass, damping, and stiffness matrices, a is the generalized acceleration, v is the generalized velocity, d is the generalized displacement, and F is the generalized force.

The discrete-time state equations are:

$$v_{n+1} = v_n + \left[(1-\delta)\, a_n + \delta a_{n+1}\right] \Delta t \tag{2.74}$$

$$d_{n+1} = d_n + v_n \Delta t + \left[\left(\frac{1}{2} - \alpha\right) a_n + \alpha a_{n+1}\right] \Delta t^2 \tag{2.75}$$

where the time step is

$$\Delta t = t_{n+1} - t_n \tag{2.76}$$

One can guarantee unconditional first-order accuracy with the proper selection of the two tuning parameters, δ and α [33], [32]. This Modified Newmark Method uses Generalized-α tuning parameters which allows the user to define a spectral radius [34], [35], ensure unconditional stability (at least in the LTI case) and prevent a knee in the spectral radius found in the Newmark method [36]. The method predicts the states and their time derivatives at each time step and then uses a Newton-Raphson sub-iteration method to correct these predictions until a user-specified tolerance is met.

The sub-iteration step begins with the prediction of the states at the next time step, as described in [32]. The predictions are then substituted back into the governing equations, resulting in a residual vector given by:

$$r = \begin{bmatrix} r_f \\ r_b \\ r_q \\ r_p \\ r_i \end{bmatrix} \tag{2.77}$$

where

$$r_f = M_{FF}\ddot{\varepsilon} + M_{FB}\dot{\beta} + C_{FF}\dot{\varepsilon} + C_{FB}\beta + K_{FF}\varepsilon - R_F \tag{2.78}$$

$$r_b = M_{BF}\ddot{\varepsilon} + M_{BB}\dot{\beta} + C_{BF}\dot{\varepsilon} + C_{BB}\beta - R_B \tag{2.79}$$

$$r_q = \dot{\zeta} + \frac{1}{2}\Omega_\zeta \zeta \tag{2.80}$$

$$r_p = \dot{p}_B - \begin{bmatrix} C^{BG} & 0 \end{bmatrix} \beta \tag{2.81}$$

$$r_i = \dot{\lambda} - F_1 \begin{bmatrix} \ddot{\varepsilon} \\ \dot{\beta} \end{bmatrix} - F_2 \begin{bmatrix} \dot{\varepsilon} \\ \beta \end{bmatrix} - F_3 \lambda \tag{2.82}$$

A Taylor series expansion is then performed on the residual vector at time-step $n+1$ and sub-iteration step $k+1$ yielding:

$$r_{n+1}^{k+1} = r_{n+1}^{k} + \left[\frac{\partial r}{\partial q}\right]_{n+1}^{k} \left(q_{n+1}^{k+1} - r_{n+1}^{k}\right) + H.O.T. \tag{2.83}$$

where

$$q = \begin{bmatrix} \varepsilon \\ \beta \\ \zeta \\ p_B \\ \lambda \end{bmatrix} \tag{2.84}$$

Setting the higher order terms to zero and given Eq. 2.83, the tangent matrix, S^k_{n+1}, is defined as

$$S^k_{n+1} = \left[\frac{\partial r}{\partial q}\right]^k_{n+1} \tag{2.85}$$

Then defining the correction term, Δq^k, as

$$\Delta q^k = q^{k+1}_{n+1} - q^k_{n+1} \tag{2.86}$$

which can then be solved as

$$\Delta q^k = -\left[S^k_{n+1}\right]^{-1} r^k_{n+1} \tag{2.87}$$

This correction term, Δq^k, is then used to update the states and their time derivative using the technique outlined in [32] and the residual vector, r, is then updated at every sub-iteration using these state updates.

The Newton-Raphson scheme outlined above generally does a good job of converging. However, due to large number of states, there may be times where an acceptably low norm of the residual vector cannot be found. When this occurs, the state correction, Δq^k, is modified using a line search algorithm:

$$\Delta q^k = \alpha_{sc}\left(-\left[S^k_{n+1}\right]^{-1} r^k_{n+1}\right) \tag{2.88}$$

Bounds on the scaling parameter, α_{sc}, are determined by calculating r at various values of

α_{sc} such that

$$0 < \alpha_{sc,l} < \alpha_{sc} < \alpha_{sc,u} < 1 \tag{2.89}$$

The upper, $\alpha_{sc,u}$, and lower, $\alpha_{sc,l}$, bounds on the scaling parameter are used in a quadratic interpolation curve fitting formula, which is then iterated until an acceptale value of α_{sc} is found.

Since it is possible for this method to find a local minimum, in which case the scaling parameter α_{sc} will be zero, an additional step is added to ensure convergence to the global minimum [32]. This is done by modifying the scaling parameter if $\alpha_{sc} < \epsilon$, where ϵ is a very small parameter, for more than a user-defined number of steps. If this occurs, then α_{sc} is arbitrarily set to

$$\alpha_{sc} = \frac{1}{4}\left(1 + k_i\right) \tag{2.90}$$

where k_i is the number of sub-iteration steps when a local minimum has been reached. Then, the state update is re-calculated using this value of α_{sc} in Eq. 2.88. This allows the Newton-Raphson method to move away from the local minimum and continue searching for the global minimum. The approach has perfomed very well at resolving convergence to local minimums [32].

2.3 Gust Modeling

The air that an aircraft flies through is never truly still. As a result, the aircraft is constantly encountering an external disturbance which affects its motion. The problem of modeling aircraft response during an encounter with wind gust is not a new one. In fact, Part 2 of the National Advisory Committee of Aeronautics (NACA) first ever technical report is titled, *Theory of an Aeroplane Encountering Gusts* [37].

The turbulence encountered by an aircraft can be caused by many different sources. The first type is convective turbulence, which occurs in and around clouds, especially thunder-

storms. This turbulence is the most violent for of turbulence disturbances[38]. The other main type of turbulence is Clear Air Turbulence (CAT), which can have several causes. These include wind shear at altitude due to flight through or near the jet stream, wind shear close to the ground caused by the Earths boundary layer, wind flowing over mountains, and updrafts caused by heating of the air [39].

There are two common methods for modeling the wind turbulence for aircraft design and simulation. These are the discrete method, where the gust is modeled using a $1 - cos$ profile, and the continuous method where the gust is modeled as a stochastic process with a known power spectral density (PSD).

2.3.1 Discrete Gust

The discrete gust method provides a way to model the turbulence as a single or repeating disturbance with a $1 - cos$ temporal distribution. This method is called out in the Federal Aviation Administrations (FAA) Federal Aviation Regulations (FAR) 25 [40] for determining aircraft response to turbulence. This study assumes that the gust is a disturbance that acts in the vertical direction only because vertical gust will impart larger elastic deformations on VFA than a horizontal gust would.. The discrete gust profile used in this study is given by:

$$U_{gust} = \frac{U_0}{2}\left(\frac{b}{2L}\right)^3\left[1 - cos\left(2\pi\frac{t}{t_{gust}}\right)\right] \tag{2.91}$$

where U_0 is the reference gust amplitude, b is the aircraft wing span, L is the turbulence length, t is the current time, and t_{gust} is the turbulence time duration. This gust profile can either enter into the system once during the simulations, or it can be repeated multiple times during the length of the simulations. A depiction of a single period discrete gust is shown in Fig. 2.3 and the repeating gust is shown in Fig. 2.4.

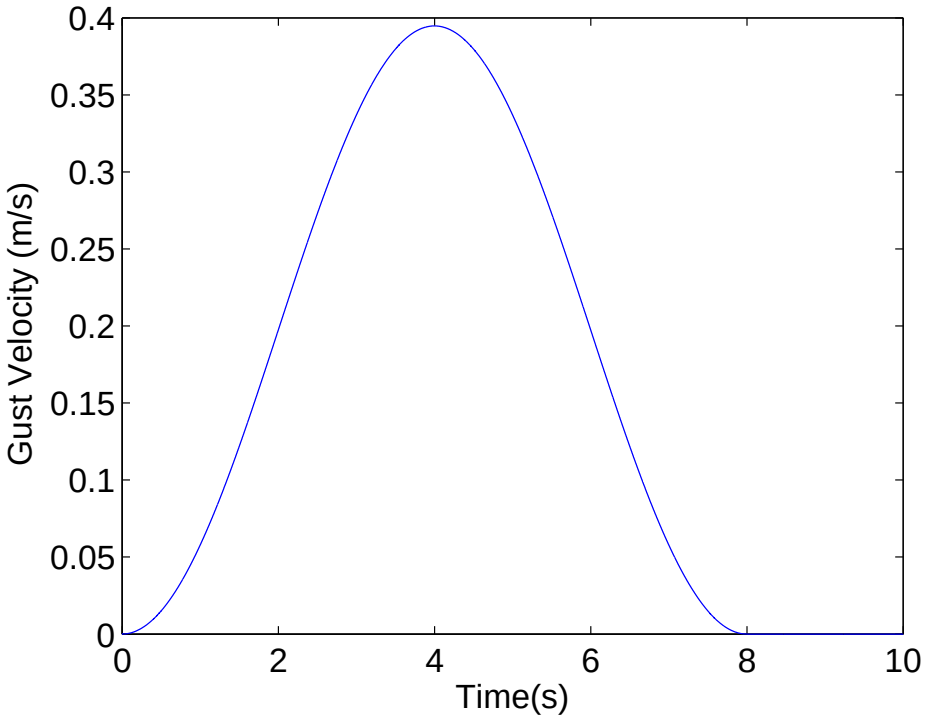

Figure 2.3: Single amplitude discrete gust.

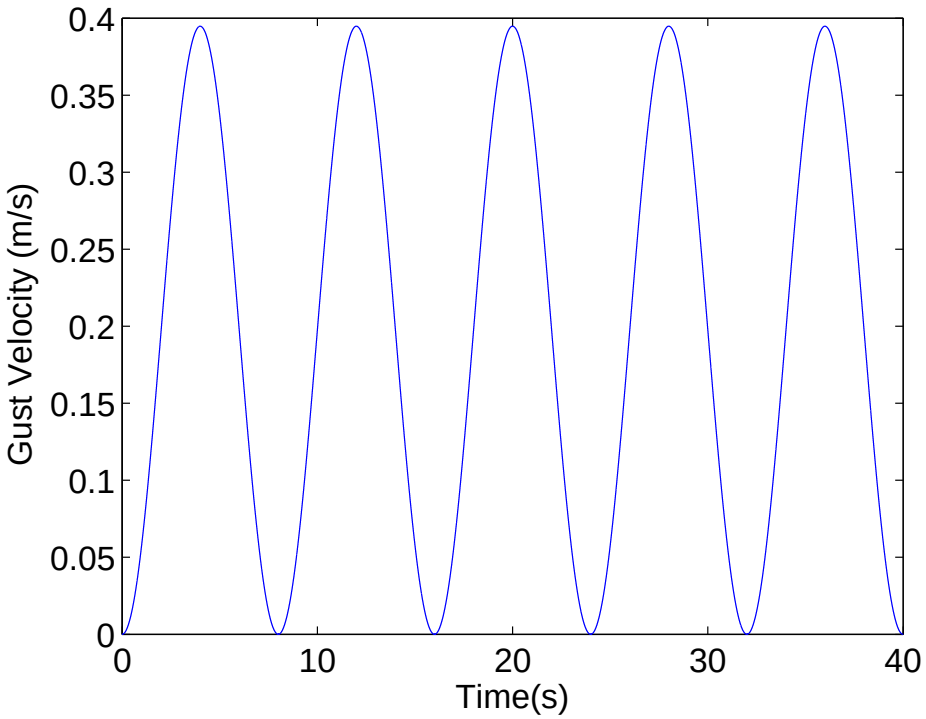

Figure 2.4: Repeating discrete gust.

2.3.2 Continuous Gust

Another common way to model atmospheric turbulence for use in aircraft simulations is to consider the turbulence as a stochastic process that is stationary and Gaussian. A stationary process is one for which the statistical properties of a sample are independent of when the sampling occurs. There are two main reasons why this formulation has become popular. Firstly, comparison with flight test data has shown this method to be more accurate than the discrete gust method. Secondly, there are relatively simple mathematical formulations developed for modeling in this fashion [39].

This method of turbulence modeling is based on the notion of PSD. The PSD of a signal gives one knowledge of how the mean squared value of that signal is distributed as a function of frequency. The most straightforward way to calculate the PSD of a function, $x(t)$, is to start by calculating the autocorrelation function [38]:

$$R\left(T\right) = \lim_{T\to\infty} \frac{1}{T} \int_0^T x\left(t\right) x\left(t+T\right) dt \tag{2.92}$$

where T is the length of the signal x in seconds. From the autocorrelation function $R(T)$, the PSD is calculated using [38]:

$$\Phi\left(\Omega\right) = \frac{1}{2\pi} \int_{-\infty}^{\infty} R\left(T\right) e^{j\omega T} dT \tag{2.93}$$

There are two main continuous gust models that use the PSD approach: the von Karman and the Dryden models. The corresponding PSDs for vertical gusts are [39]:

$$\Phi_{vk}\left(\Omega\right) = \sigma^2 \frac{L}{\pi} \left(\frac{1 + \frac{8}{3}\left(1.339L\Omega\right)^2}{\left[1 + \left(1.339L\Omega\right)^2\right]^{11/6}} \right) \tag{2.94}$$

$$\Phi_{d}\left(\Omega\right) = \sigma^2 \frac{L}{\pi} \left(\frac{1 + 3L^2\Omega^2}{\left(1 + L^2\Omega^2\right)^2} \right) \tag{2.95}$$

where σ is the root mean square gust velocity, L is the turbulence length, and Ω is the

spatial frequency which is defined as

$$\Omega = \frac{\omega}{v_{By}} \tag{2.96}$$

where ω is the angular frequency and v_{By} is the forward velocity of the aircraft. Equation 2.96 can also be used to convert Eqs. 2.94 and 2.95 to units of ω.

In practice, a time history of the gust is created by passing a white noise signal, Φ_η, through a coloring filter as shown in Fig 2.5. The coloring filter, $G(s)$, is designed so that the output signal $\Phi(\omega)$ will have the desired PSD. An exact coloring filter for the Dryden spectrum can be determined while only an approximate filter can be determined for the von Karman model. However, flight test data have shown a better agreement with the von Karman PSD that the Dryden PSD. This leads to a tradeoff that one wishing to simulate gust response must make. The coloring filter for the Dryden profile is given by [39]:

$$G_{dry}(s) = \sigma_w \sqrt{\frac{\tau}{\pi}} \frac{1 + \sqrt{3}\tau s}{(1 + \tau s)^2} \tag{2.97}$$

where $\tau = L/v_{By}$. An approximate von Karman coloring filter is:

$$G_{vk}(s) = \sigma_w \sqrt{\frac{\tau}{\pi}} \frac{(1 + 2.187\tau s)(1 + 0.1833\tau s)(1 + 0.021\tau s)}{(1 + 1.339\tau s)(1 + 1.118\tau s)(1 + 0.1277\tau s)(1 + 0.0146\tau s)} \tag{2.98}$$

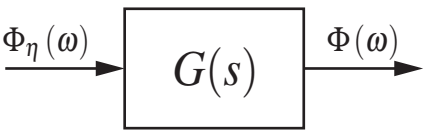

Figure 2.5: Coloring filter for PSD creation

2.3.3 Spanwise Gust Distribution

There are several different ways to model the spanwise distribution of the gust field. Hoblit [39] states that the gust is isotropic, meaning that the spanwise distribution would be the same as the temporal distribution if one views the gust as being frozen in space as the aircraft flies through it. Another approach is to argue that the aircraft wing span is significantly less than the turbulence scale, which usually has a value between 1750 ft and 2500 ft (533 m and 762 m), so that the spanwise variation in gust is negligible. For the Vulture program, the Defense Advanced Projects Agency (DARPA) [41] suggested using a sinusoidal spanwise variation, with the sinusoidal distribution placed so as to cause the largest bending moment possible. A depiction of a DARPA gust profile is shown in Fig. 2.6.

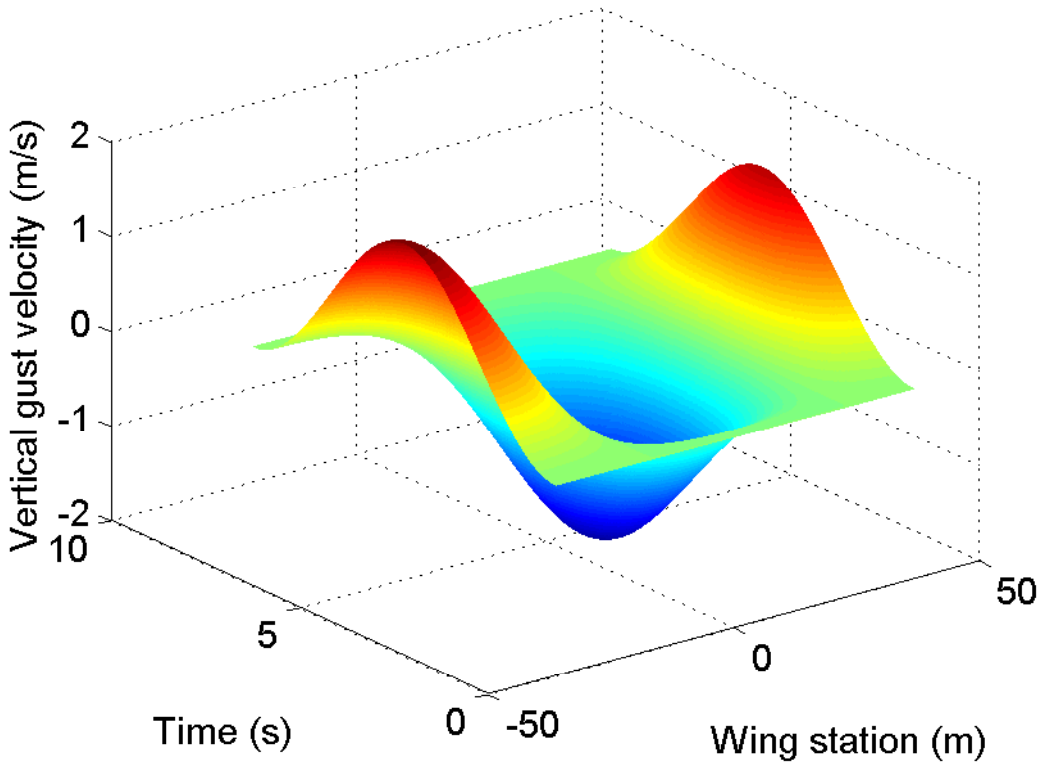

Figure 2.6: DARPA gust profile

2.4 Numerical Implementation

This section provides an overview of the numerical simulation framework used in this study. A historical summary as well as a capability overview are presented. The computer program package is known as the University of Michigan Nonlinear Aeroelastic Simulation Toolbox (UM/NAST) and is coded in Matlab which allows for user-friendly code development. The original framework was developed by Brown [24] under the guidance of Professor Carlos E. S. Cesnik with significant improvements made by Shearer [7], [17], [32] and Su [1], [25], [26], [27], [28].

2.4.1 Historical Overview

The code package was originally developed for use in nonlinear aeroelastic simulations of flexible aircraft. The initial implementation contained a reduced-order strain based formulation for geometrically nonlinear beam elements containing active piezoelectric actuators. The code was capable of static and dynamic aeroelastic simulations and was used to compare wing warping control with traditional aileron control [24].

Shearer and Cesnik [16], [7], [17], [32] corrected and improved the governing differential equations by adding Coriolis effects, developed the long term stable integration scheme, enhanced the framework for closed loop simulations, developed a closed form solution to the matrix exponential and closed form solutions to the Jacobian matrices. Su and Cesnik [1], [25], [26], [27], [28] developed kinematic relationships for the modeling of split beams, added changes in torsional stiffness due to skin wrinkling, developed a method for accounting for absolute and relative constraints using Lagrange multipliers, developed a method for finding the nonlinear flutter boundary, implemented a discrete gust capability, derived the aerodynamic Jacobians, developed a method for linearizing the nonlinear governing equations, and developed the capability to analyze and simulate flapping wing aerial vehicles. In this dissertation we expanded the linearization routines to include calcu-

lation of the control and gust effector matrices, commonly known in controls as the B and B_w matrices, and augmented the gust models to include von Karman and Dryden models. Additional minor changes were also made to improve computational efficiency.

2.4.2 Architecture

Figure 2.7 shows an overview of the current version of UM/NAST. The code is organized into several inter-connected modules. These modules include: initialization, modal analysis, flight dynamics determination, trim, static solver, time simulation, and linearization. There are other capabilities, such as flutter boundary determination, that were not used in this study as well as additional post-processing tools.

2.4.3 Input Files and Model Initialization

The two inputs files described in [17] and [25] have been combined into a single input file in the current version of UM/NAST, *filename.nin*. This file allows the user to define the aircraft model to be used by specifying geometric, inertial, mass, and stiffness properties to be used. The file also has sections for the user to specify aerodynamic options to be used, such as stall model type and inflow force inclusion, as well as the flight conditions, specifically altitude and airspeed. A time history of pilot inputs can be included. Various options needed for closed-loop simulations are defined, such as outputs to be tracked, control inputs used and control sampling time. Finally, the type of simulation to be run is defined as well as various other options pertaining to file and screen ouputs.

The aircraft wings are modeled as beams around a reference point somewhere on the aircraft, which is in general not at the aircraft center of gravity. The beam structure is defined using the levels key point - member - group. Two or more key points define a member, and a group is a set of members that originates from a single key point. The kinematics of a particular member are only coupled with members in the same group [25].

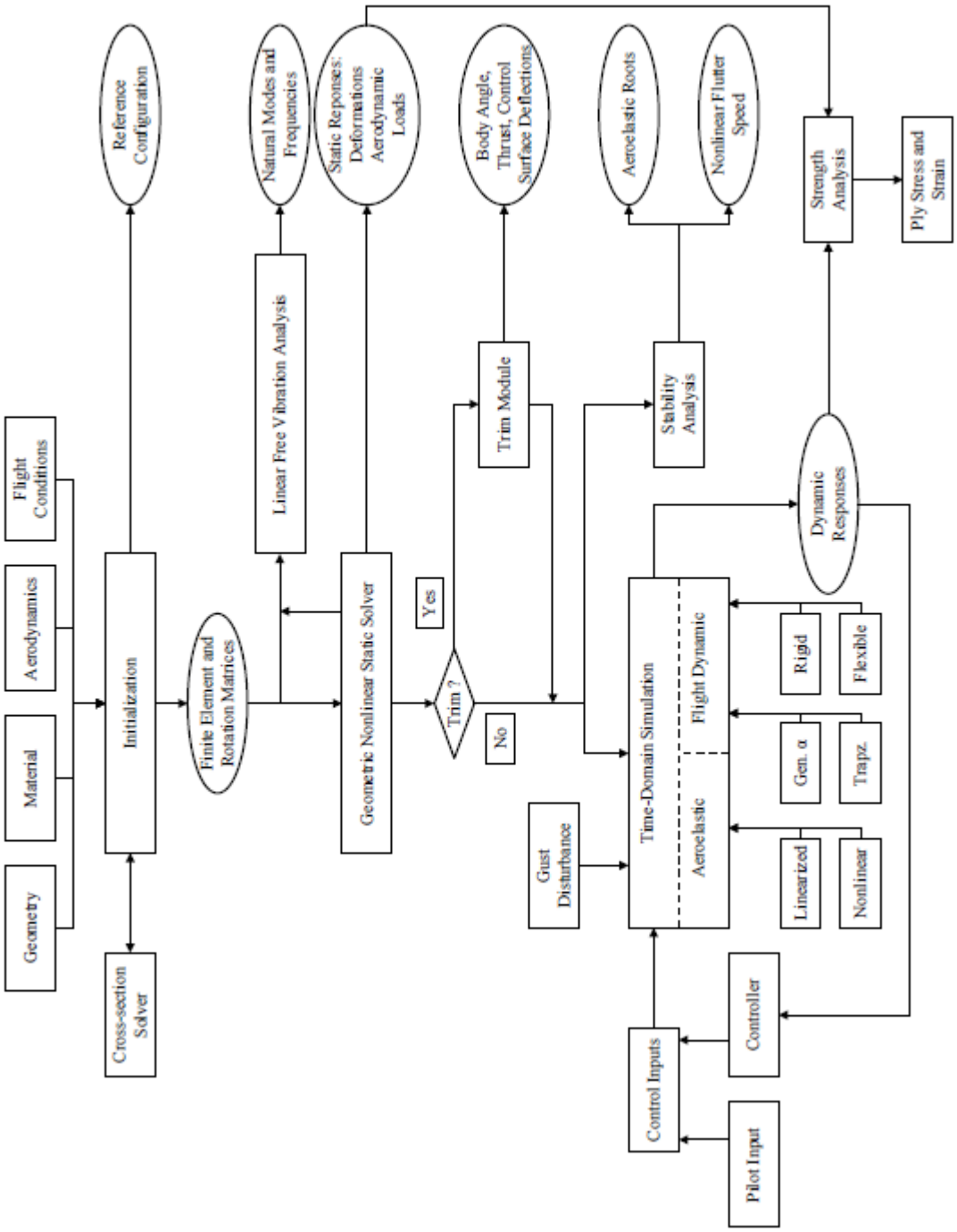

Figure 2.7: Functional overview of UM/NAST code [25]

Multiple subroutines are then called to initialize the run, which determine the undeformed shape, mass, damping and stiffness matrices, unsteady aerodynamic inflow matrices, structural Jacobians, and rotation matrices between the various reference frames used.

2.4.4 Modal Analysis

The modal analysis routine allows a user to determine the natural modes and frequencies of the aircraft. The modes can be determined in different configurations: the aircraft can be in free flight or fixed at the origin of its B frame. The mode can be extracted about its undeformed, trimmed, or any other statically loaded condition.

2.4.5 Linearized Flight Dynamics Module

The flight dynamics module allows a user to get a representation of the flight dynamic modes of the complete aircraft in free flight. The routine is started by the user running a trim solution to ensure the aircraft is at an approximate equilibrium state. Then the aircraft model is linearized about this trim state, retaining only the rigid body vector:

$$x_{rigid} = \begin{bmatrix} v_x \\ v_y \\ v_z \\ \omega_x \\ \omega_y \\ \omega_z \\ \phi \\ \theta \\ \psi \end{bmatrix} \tag{2.99}$$

where v_i are the velocity components, ω_i are the rotational velocity components, and ϕ, θ,

and ψ are the Euler roll, pitch and yaw angles, respectively.

Then a method similar to that found in [42] is followed, where the yaw angle, ψ is neglected and the remaining rigid body linearization is further separated into longitudinal and lateral components:

$$x_{rigid,long} = \begin{bmatrix} v_y \\ v_z \\ \omega_x \\ \theta \end{bmatrix}, \quad x_{rigid,lat} = \begin{bmatrix} v_x \\ \omega_y \\ \omega_z \\ \phi \end{bmatrix} \tag{2.100}$$

The eigenvalues of the longitudinal and lateral linearizations are found. The short period, if it exists, is then the longitudinal eigenvalue pair of higher frequency and the pair with the lower frequency is the phugoid. The lateral linearization typically has a single eigenvalue pair and then two non-oscillatory eigenvalues. The eigenvalue pair is the Dutch Roll mode, while the two other eigenvalues represent the spiral and roll modes. Although we make reference to classic, rigid body flight dynamic modes, the modes exhibited by VFA are dominated by these rigid body modes but are also coupled with the elastic modes.

2.4.6 Static Solver

The geometric nonlinear static solver is run to determine the static deformation of the aircraft to a given load condition. The routine input consists of flight conditions and control surface deflections. The equations of motion are then solved with the rigid-body motion constrained and the time derivatives and inflow force terms removed. Since the aerodynamic forces are a function of local angle of attack, and therefore aircraft deflection, the solution is iterative. As the routine begins the aerodynamic forces are calculated, causing an aircraft deformation, causing a change in aerodynamic forces, etc. The routine is then iterated until a user defined tolerance is met. The outputs of the routine are the final strain vector, which shows final aircraft deformation, global and local aerodynamic forces and

structural and aerodynamic Jacobians.

2.4.7 Trim Module

The trim module implements the formulation described in Section 2.2. There are two ways to trim the aircraft based on either a force or acceleration balance. This module output the body angle of attack, control surface deflection, and thrust force required to trim the aircraft at 1-g level flight at the user input altitude and airspeed.

2.4.8 Time-marching Simulation

The time marching simulation begins by running a static solution. The user can define multiple simulation types: nonlinear, linearized (the structural Jacobians are kept constant) and rigid body. The user can also define the time integration scheme: the modified Newmark method described in Sec. 2.2.2 or the trapezoidal method. The time marching solution is also capable of time-varying control inputs in either open loop, through use of a table, or closed loop, through use of a user defined feedback control file. The user may also select which gust profile, if any, to use in the simulation.

CHAPTER 3

Gust Response Sensitivity

This chapter presents a study on the sensitivity of aircraft response to a gust disturbance as a function of various stiffness parameters. Two different baseline VFA configurations, a flying wing model as well as a flying wing with tails, are considered. The baseline stiffness parameters are varied, while keeping the aircraft geometric and inertial properties constant to create multiple aircraft models. These models are then simulated in the presence of several different gust profiles. Various response characteristics are then studied as a function of various aircraft parameters to determine any trends that are present.

3.1 Aircraft Models

3.1.1 Flying Wing

The flying wing model used in this study is a Helios-like vehicle originally developed in [43] and later studied in [1]. The aircraft has a rectangular planform with a span of 72.8 m and a constant chord of 2.44 m. The outer one-third of the wing on each side has a dihedral angle of 10° to provide lateral stability. There are five motors, equally spaced on the section of the wing with no dihedral. The aircraft also has three pods, each capable of carrying a varying payload. In this study the payload on the two outer pods it set to 27.23 kg and the center pod payload can vary from 0 kg to 227 kg. Figure 3.1 shows the aircraft geometry and Table 3.1 lists the aircraft properties.

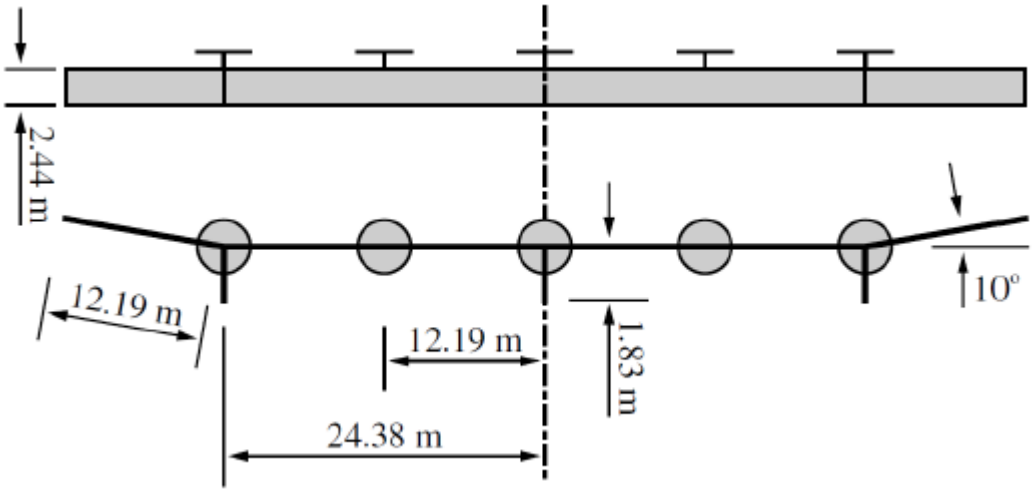

Figure 3.1: Flying wing VFA model geometry [1]

Table 3.1: Flying Wing Model Properties (no elastic nor inertial couplings present)

PARAMETER	BASELINE VALUE
Elastic Axis	25% chord
Center of Gravity	25% chord
Stiffness properties	
Bending stiffness	1.03 x $10^6 N \cdot m^2$
Torsional stiffness	1.65 x $10^5 N \cdot m^2$
In-plane bending stiffness	1.24 x $10^7 N \cdot m^2$
Extensional Stiffness	1 x $10^{10} N$
Inertial properties	
Mass per unit length	8.93 kg/m
Bending mass moment of inertia	0.69 $kg \cdot m$
Torsional mass moment of inertia	4.15 $kg \cdot m$
In-plane bending mass moment of inertia	3.46 $kg \cdot m$
Aerodynamic properties	
$c_{l\alpha}$	2 π
$c_{l\delta}$	1
c_{d0}	0.01
c_{m0}	0.0025
$c_{m\delta}$	-0.25

The aircraft is trimmed for level flight at 12.2 m/s. The trim shape of the aircraft is very dependent on the payload of the center pod. This is because at low payloads, the aircraft is span loaded, while at higher payloads, the aircraft moves more toward point mass loading. This behavior was also seen on the Helios aircraft [2]. In fact, one of the finding from the mishap report was a failure to understand the effect a larger center pod payload had on aircraft flight dynamics [2]. Figure 3.2 shows a comparison between the trim shape of the 0-kg and 227-kg configurations superimposed on the undeformed jig shape of the aircraft. The trim shape of the 0-kg payload and the undeformed shape are virtually identical, while the trimmed and undeformed shapes for the 227-kg case are vastly different, even though the flight condition, material and inertial properties for the two models are identical.

Figure 3.2: Comparison of trimmed shape for 0-kg (left) and 227-kg (right) center payloads to undeformed shape (black mesh) [1]

The properties of the phugoid mode are dependent on aircraft shape, and therefore are also dependent on center pod payload. The phugoid frequency and damping were calculated for payloads ranging from 0 kg to 227 kg, with the poles plotted in Fig. 3.3. The phugoid mode is initially stable with a 0-kg payload, but the addition of mass de-stabilizes the mode, with it eventually becoming unstable at about 145 kg. For this study a stable point, close to the stability boundary, of 140-kg payload was chosen, shown in Fig. 3.3 with a red diamond.

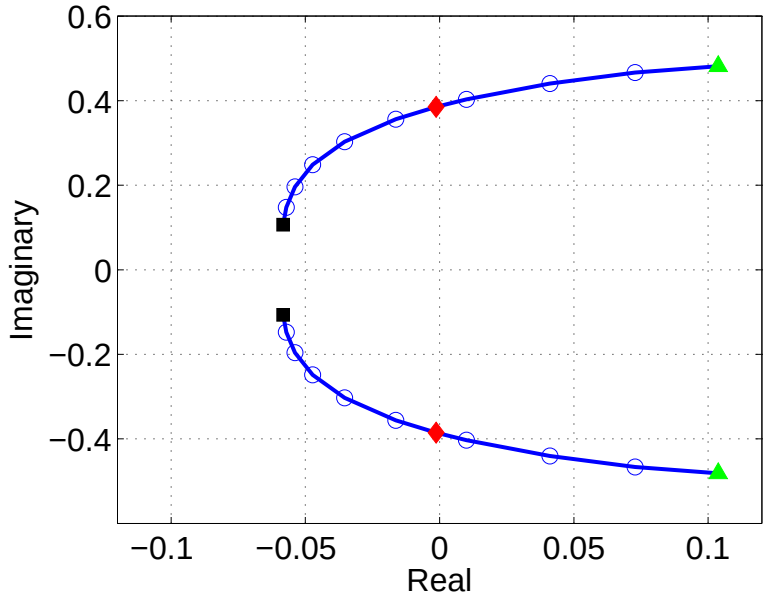

Figure 3.3: Phugoid poles varying center pod payload from 0 kg (square) to 227 kg (triangle).

3.1.2 X-HALE

The X-HALE is an aeroelastically representative test bed developed at the University of Michigan. The aircraft has a wingspan of 6 m, with the outboard 1 m on each side having a dihedral angle of 10° and a constant chord of 0.2 m. The aircraft has four all moveable horizontal tails and a tail in the center that can be horizontal or flipped to the vertical, and is kept vertical in this study. The aircraft also has five motors spaced evenly along the non-dihedral section of the wing. A UM/NAST representation of the X-HALE is shown in Fig. 3.4 and a picture of the X-HALE in flight is shown in Fig. 3.5. Additionally, the X-HALE aircraft properties are listed in Table 3.2. The aerodynamic forces and moments are calculated using a table created by running $XFOIL$ using the aircraft's airfoil, EMX07.

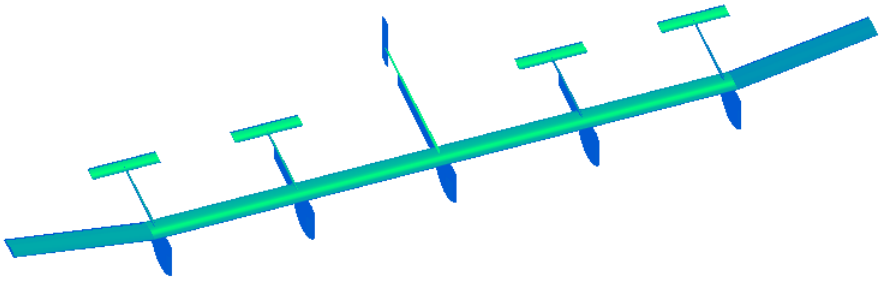

Figure 3.4: UM/NAST representation of X-HALE.

Figure 3.5: X-HALE in flight.

Table 3.2: X-HALE Model Properties

PARAMETER	BASELINE VALUE
Elastic Axis	28.78% chord
Center of Gravity	43.5% chord
Stiffness properties	
Bending stiffness	112 $N \cdot m^2$
Torsional stiffness	55.8 $N \cdot m^2$
In-plane bending stiffness	6350 $N \cdot m^2$
Extensional stiffness	2.14 x $10^6 N$
Coupling Terms	
Extensional/bending	1.54 x $10^3 N \cdot m$
Extensional/in-plane bending	-4.91 x $10^4 N \cdot m$
Torsional/bending	0
Torsional/in-plane bending	0
In-plane bending/bending	-46.3 x $N \cdot m^2$
Inertial properties	
Mass per unit length	0.50 kg/m
Bending mass moment of inertia	1.22 x $10^{-5} kg \cdot m$
Torsional mass moment of inertia	8.09 x $10^{-4} kg \cdot m$
In-plane bending mass moment of inertia	7.97 x $10^{-4} kg \cdot m$

3.2 Open Loop Sensitivity

3.2.1 Flying Wing Open Loop Sensitivity

In order to examine the sensitivity of the flying wing aircraft stability and gust response to variations in stiffness properties, the bending, torsional and in-plane bending stiffness, aircraft models for simulation were created by varying the elements of the stiffness matrix. The original intent was to vary these three parameters up and down one order of magnitude from the baseline value. However, it was found that there was a lower bound on bending stiffness, below which the aircraft was too flexible for a successful trim to be possible. The property variations, from the baseline values, are shown in Table 3.3. Variations in the extensional stiffness were seen to have virtually no effect on aircraft response, so it is not varied in this study. Additionally, all geometric and inertial properties of the aircraft are held constant during model creation.

Table 3.3: Flying Wing Model Property Variations

PARAMETER	VARIATION	% CHANGE
Bending stiffness	5 x10^5 - 9 x $10^6 N \cdot m^2$	49% - 873%
Torsional stiffness	3 x10^4 - 7 x $10^5 N \cdot m^2$	18% - 424%
In-plane bending stiffness	1 x10^6 - 7 x $10^7 N \cdot m^2$	8% - 565%

3.2.2 Stability Study

To determine the effect of the stiffness parameter variations on the phugoid mode, the phugoid poles were plotted as the individual stiffness parameters were varied, while keeping the other parameters at the baseline values and using a center payload of 140 kg. The phugoid mode pole plots as a function of the torsional, bending and in-plane bending stiffness are shown in Fig. 3.6, with the black diamond indicating a rigid aircraft, the green square is the highest stiffness used and the red triangle the lowest. As the figure shows, the stability of the phugoid mode is a function of the stiffness chosen. For the torsional and bending stiffnesses, as the values are lowered, the phugoid mode damping increases, eventually crossing the stability boundary. This phenomenon is caused by the coupling between the elastic and rigid body modes. As the aircraft becomes more flexible in torsion or bending, the elastic modes frequencies approach the rigid body frequencies,and the elastic modes begin to amplify the rigid body motion. Interestingly, the phugoid mode shows the opposite trend when the in-plane stiffness is varied. As the in-plane stiffness is lowered, the phugoid pole damping becomes more negative, indicating the pole is moving away from the stability boundary, although the damping is very close to the stability boundary for all cases.

After the lower and upper bounds shown in Table 3.3 were chosen, Latin Hypercube Sampling (LHS) [44] was used to determine the optimal placement of the aircraft model stiffness parameters within this three-dimensional sample space. A matrix of points between zero and one was created using the Matlab command *lhsdesign* which ran one million samples attempting to maximize the minimum distance between any two points. The simulation models were then generated by multiplying the matrix calculated by Matlab by

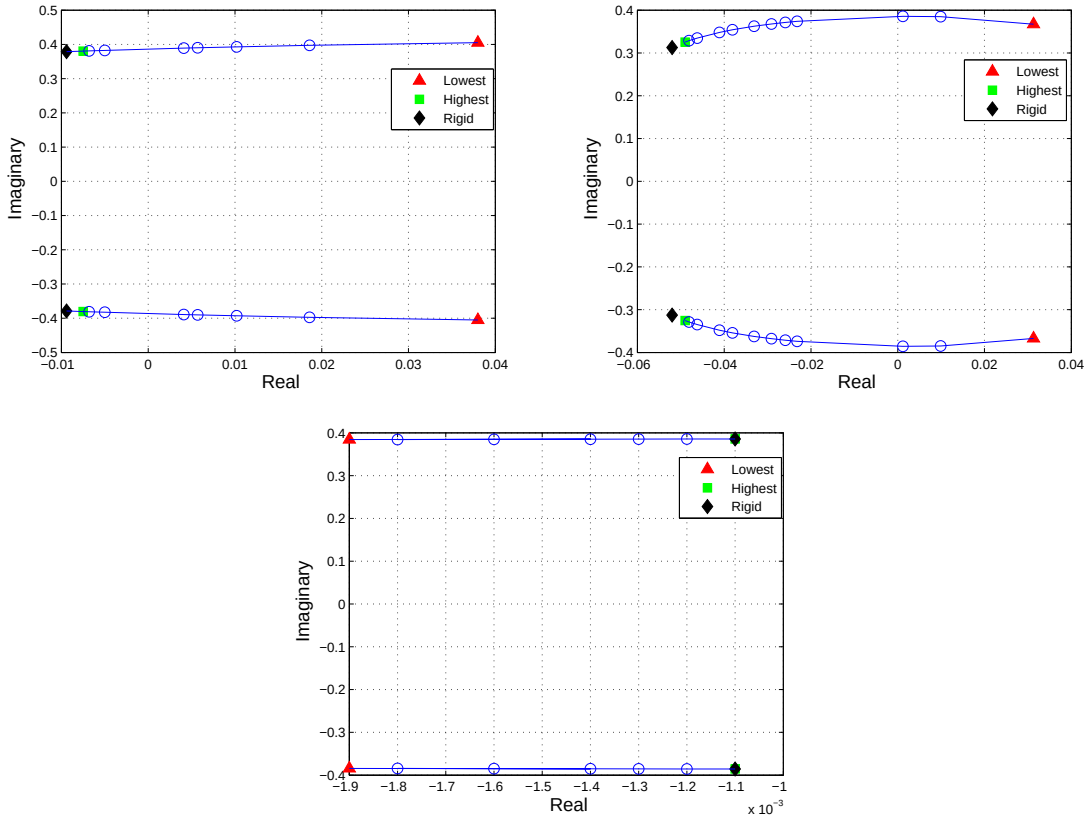

Figure 3.6: Phugoid poles as a function of torsional stiffness (top left), bending stiffness (top right) and in-plane bending-stiffness (bottom) for the flying wing model (140-kg payload)

the upper and lower bounds, giving ten aircraft models. After visually inspecting the sample space, it was determined that there were two regions without acceptable sampling, so two additional aircraft model parameters were manually chosen. The stiffness parameters for the aircraft simulation models are shown in Table 3.4.

Table 3.4: Flying Wing Model Stiffness Properties (Extensional = 1 x $10^{10} N$)

MODEL	BENDING $(N \cdot m^2)$	TORSIONAL $(N \cdot m^2)$	IN-PLANE BENDING $(N \cdot m^2)$
Baseline	1.03 x 10^6	1.65 x 10^5	1.24 x 10^7
1	6.93 x 10^6	1.73 x 10^5	1.80 x 10^7
2	2.08 x 10^6	5.11 x 10^5	2.69 x 10^7
3	4.79 x 10^6	0.78 x 10^5	4.51 x 10^7
4	4.35 x 10^6	3.60 x 10^5	6.91 x 10^7
5	0.74 x 10^6	1.14 x 10^5	3.08 x 10^7
6	3.03 x 10^6	2.36 x 10^5	0.77 x 10^7
7	5.82 x 10^6	4.58 x 10^5	1.09 x 10^7
8	7.32 x 10^6	6.18 x 10^5	3.73 x 10^7
9	8.96 x 10^6	4.11 x 10^5	5.95 x 10^7
10	3.11 x 10^6	6.68 x 10^5	5.38 x 10^7
11	1.01 x 10^6	3.00 x 10^5	6.00 x 10^7
12	1.20 x 10^6	6.01 x 10^5	1.50 x 10^7

The flight dynamic modes for the aircraft models are shown in Table 3.5. The models do not show the short period mode, which is a longitudinal mode exhibiting a higher frequency and damping ratio than the phugoid. Instead there is a longitudinal pair of stable, real eigenvalues. The phugoid mode is stable for all models except Model 5, which also has the lowest bending stiffness. Additionally, the baseline model and model 11, both with bending stiffness slightly higher than model 5, have phugoid modes which, while stable, are close to the stability boundary. When looking at the lateral modes, only the four models with the lowest bending stiffness, the baseline model and models 5, 11 and 12, exhibit the classical Dutch Roll mode. The other models instead have a pair of stable, real eigenvalues. Finally, the roll and spiral mode eigenvalues do not change much with the variation in stiffness parameters.

The elastic modes of the aircraft in its undeformed configuration are shown in Table 3.6. The table shows that all fundamental modes occur at relatively low frequencies. With

Table 3.5: Flying Wing Model Flight Dynamic Properties

MODEL	PHUGOID	SHORT PERIOD	DUTCH ROLL	ROLL	SPIRAL
Baseline	$-0.0015 \pm 0.359i$	$-6.22, -3.89$	$-0.295 \pm 0.154i$	-7.09	-0.210
1	$-0.048 \pm 0.329i$	$-7.32, -3.89$	-0.484, -0.098	-7.12	-0.218
2	$-0.0358 \pm 0.357i$	$-6.65, -2.71$	-0.409, -0.150	-7.12	-0.246
3	$-0.0451 \pm 0.339i$	$-7.08, -3.58$	-0.469, -0.112	-7.11	-0.225
4	$-0.0456 \pm 0.337i$	$-7.10, -3.60$	-0.468, -0.110	-7.13	-0.219
5	$0.0319 \pm 0.372i$	$-5.93, -0.93$	$-0.29 \pm 0.247i$	-7.05	-0.229
6	$-0.0417 \pm 0.346i$	$-6.86, -3.20$	-0.445, -0.127	-7.12	-0.225
7	$-0.0476 \pm 0.330i$	$-7.26, -3.81$	-0.480, -0.100	-7.13	-0.217
8	$-0.0486 \pm 0.327i$	$-7.38, -3.94$	-0.486, -0.095	-7.13	-0.216
9	$-0.0492 \pm 0.325i$	$-7.46, -4.03$	-0.491, -0.092	-7.13	-0.215
10	$-0.0426 \pm 0.344i$	$-6.91, -3.28$	-0.450, -0.123	-7.12	-0.223
11	$-0.0028 \pm 0.383i$	$-6.23, -1.46$	$-0.295 \pm 0.152i$	-7.09	-0.206
12	$-0.0168 \pm 0.375i$	$-6.43, -1.81$	$-0.302 \pm 0.103i$	-7.11	-0.190

the exception of model 4, which has a 1^{st} torsional frequency lower than the 1^{st} in-plane bending frequency, the 1^{st} bending mode has the lowest frequency, followed by the 1^{st} in-plane bending mode and the 1^{st} torsional mode having the highest frequency. An important VFA parameter is the separation between the elastic modes and the flight dynamic modes. Examination of Tables 3.5 and 3.6 shows that there is not much of a separation between the phugoid mode and the 1^{st} bending mode frequency. Model 5 only has a separation of 0.057 Hz between the 1^{st} bending mode frequency and the phugoid mode frequency. In fact, the largest separation is for model 9, which only has 0.348-Hz separation.

The aircraft were then trimmed for level flight with a velocity of 12.192 m/s at sea level. The various trim parameters are shown in Table 3.7, with the convention that a positive elevator deflection denotes trailing edge down. By examining the wingtip deflection, it is clear that there is a large variation in trim shape of the various aircraft models. The tip deflection ranges from 2.62 m, which is not much different from the undeformed deflection of 2.12 m due to the 10° dihedral, to 9.98 m including the 2.12 m due to the dihedral, which is almost 22% of the half span. The table also shows that the trim values stay relatively constant, regardless of aircraft properties. One would expect that the aircraft models with larger tip deflections would have a larger trim angle of attack, because as the

Table 3.6: Flying Wing Model Elastic Frequencies (Hz) about the Aircraft's Undeformed Configuration

MODEL	1^{st} BENDING	1^{st} TORSIONAL	1^{st}IN-PLANE BENDING
Baseline	0.137	0.978	0.445
1	0.355	1.04	0.519
2	0.195	1.67	0.671
3	0.295	0.506	0.759
4	0.281	1.67	0.917
5	0.116	1.03	0.557
6	0.235	1.10	0.364
7	0.325	1.50	0.437
8	0.365	1.86	0.783
9	0.404	1.68	0.901
10	0.238	1.98	0.922
11	0.135	1.19	0.326
12	0.148	2.09	0.165

models get more deformed into a "U" shape, the lift vector is no longer pointing straight up and has a larger horizontal component. Therefore, the aircraft raises its body angle of attack to account for this loss of lift. This in turn necessitates a larger elevator deflection angle to counteract the moment increase. The reason for the counterintuitive trim results is unknown at this time, but should be studied in the future.

Table 3.7: Flying Wing Aircraft Trim Parameters

MODEL	ANGLE OF ATTACK (DEG)	ELEVATOR DEFLECTION (DEG)	THRUST PER MOTOR (N)	WINGTIP DEFLECTION (m)	HALF SPAN DEFLECTION %
Baseline	3.99	4.85	37.23	7.08	19.4
1	3.87	4.86	37.24	2.79	7.7
2	4.04	4.84	37.23	4.29	11.8
3	3.66	4.83	37.23	3.17	8.7
4	3.98	4.85	37.24	3.16	8.6
5	4.06	5.00	37.21	9.98	27.4
6	3.94	4.85	37.24	3.64	10
7	3.99	4.86	37.24	2.89	7.9
8	4.01	4.86	37.24	2.72	2.7
9	3.98	4.86	37.24	2.62	7.5
10	4.03	4.85	37.24	3.56	7.2
11	4.10	4.88	37.23	7.02	19.3
12	4.11	4.89	37.23	5.98	16.4

3.2.3 Gust Response Study

The gust response of the baseline model was determined by running simulation using the DARPA gust described in Section 2.3.3. A reference gust velocity, U_{ref}, of 10 m/s was selected due to its proximity to the aircraft's cruise speed of 12.2 m/s. The derived gust velocity, U_{de}, is calculated using:

$$U_{de} = \frac{U_{ref}}{2}\left[1 - cos\left(2\pi\frac{t}{t_g}\right)\right] \tag{3.1}$$

where t is the current time and t_g is the gust duration. Once the derived gust velocity U_{de} is determined, then the single amplitude gust velocity, U_{SA}, is calculated by:

$$U_{SA} = \frac{U_{de}}{2}\left(\frac{b}{2L}\right)^{\frac{1}{3}} \tag{3.2}$$

In this study, the turbulence length, L, is taken to be the standard Dryden value of 2500 ft.

The gust is then applied within UM/NAST at 111 nodes along the wing. The gust applied at the i-th node is given by:

$$U_{gust,i} = U_{SA}cos\left(\frac{x_i}{4\pi}\right) \tag{3.3}$$

The model was subjected to 2-s, 4-s and 8-s duration gusts of the form described above. A depiction, in both time and space, of a 8-s duration gust is shown in Fig. 3.7. The gust velocity is at a maximum at the wing tips and a minimum in the center of the aircraft. This profile will induce much higher wing curvatures than a constant spanwise gust of the same magnitude. Also, the maximum gust velocity used is approximately 1.8 m/s.

A simplified stall model [1] is used in this study. The lift coefficient , c_l, is kept constant at $c_{l,max}$ if the angle of attack exceeds a user-defined α_{stall}. Additionally, the moment coefficient, c_{m0}, is also lowered to a constant value, $c_{m0,stall}$ above α_{stall}. The stall angle

of attack is set to 14° for this work. Although in subsequent results the pitch angle exceeds 14°, the aircraft does not stall because the stall angle is also dependent on the local angle of attack.

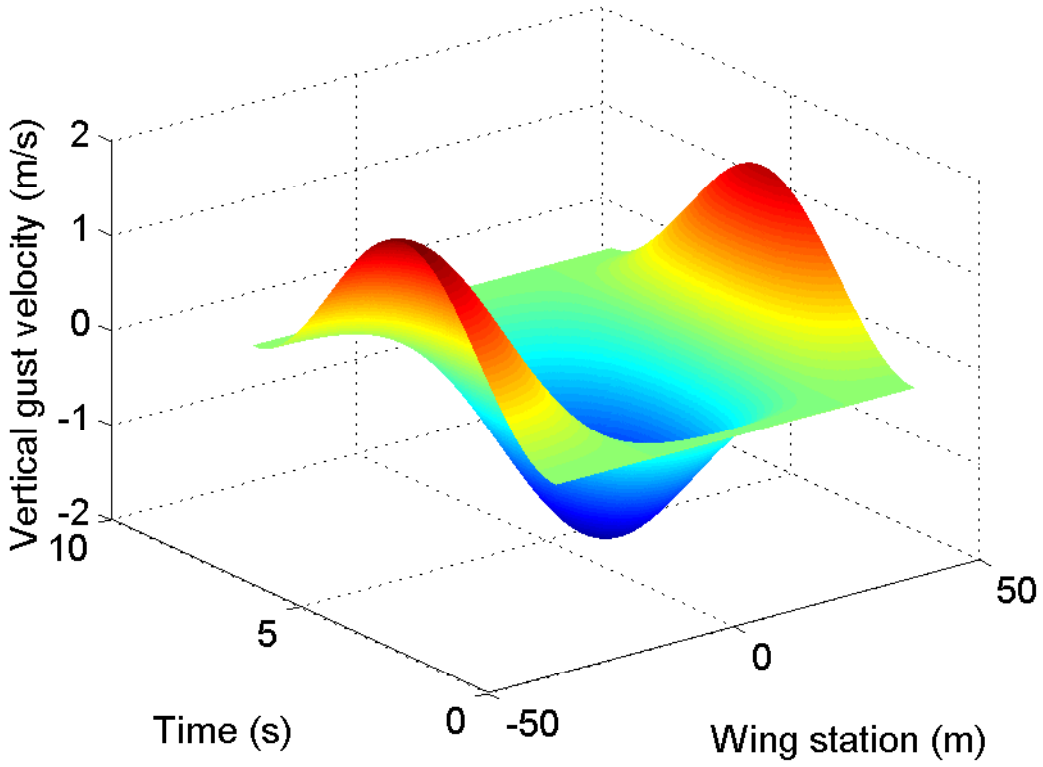

Figure 3.7: 8-s duration DARPA gust profile

The aircraft response due to the varying gust durations was studied by comparing the response of four outputs: forward velocity, altitude, pitch angle, and the wing curvature about the y-axis measured at the center of the wingspan. This is the location where a normal configuration aircraft would have a wing root, and for this reason it is referred to as the root curvature.

The responses of the baseline aircraft, in nonlinear simulations, to the 2-s, 4-s, and 8-s duration gusts with a reference gust velocity of 10 m/s are shown in Fig. 3.8. The figures show that the gust duration is an important parameter when determining aircraft response. Although, the maximum amplitude is the same in all cases, the aircraft response

is very different. The responses of all four outputs examined are larger as the gust duration is increased, with all being asymptotically stable. This is reasonable since only a single period is simulated, with the gust going to zero afterwards, the amount of time the gust acts upon the aircraft is dependent on the gust duration. In fact, the turbulence that caused the Helios mishap was within acceptable limits, however the aircraft was in the gust field for longer than on previous flights due to a shallower than normal climb out [2]. As the gust duration increases, the root curvature value remains at a higher value for a longer period of time and takes significantly longer to return to the trim values. Additionally, the aircraft reaches a new equilibrium state for altitude, with the longer duration gusts causing a larger drop in altitude.

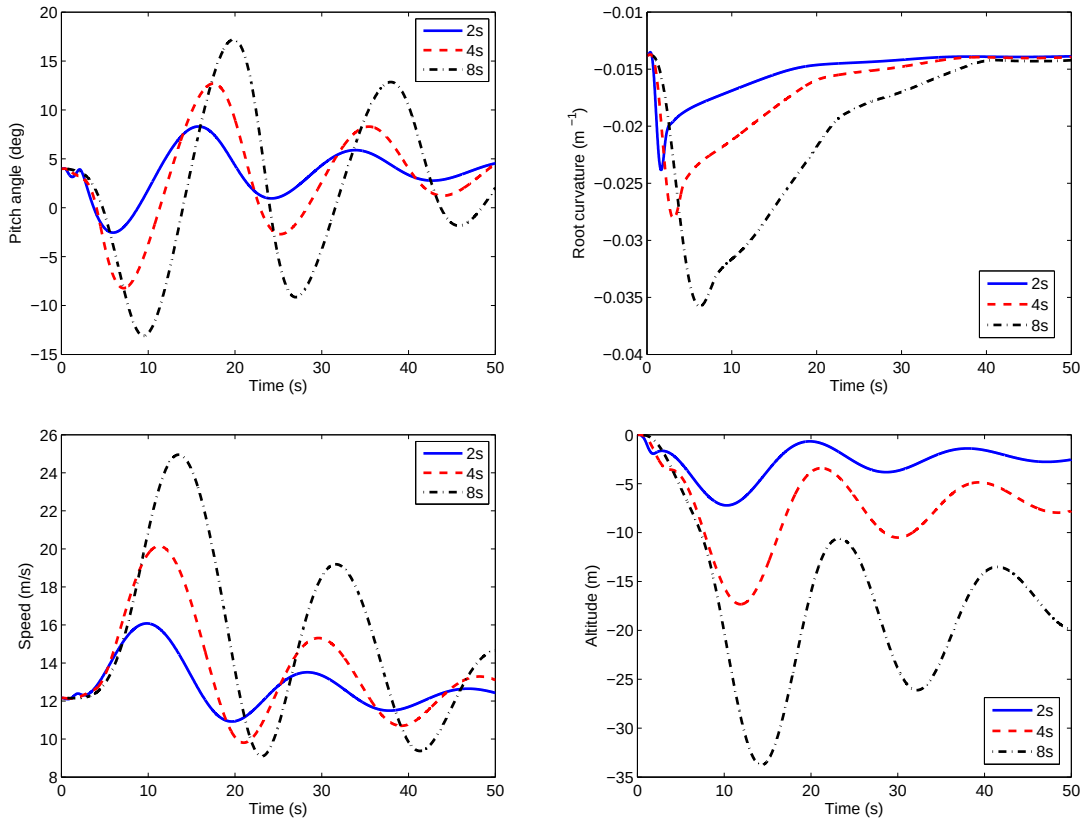

Figure 3.8: Gust response of baseline flying wing model to gust durations of 2 s, 4 s, and 8 s.

In order to increase the excitation caused by the gust, the baseline aircraft was subjected to a 2-s duration gust with the reference gust velocity values of 10, 20, 30 and 40 m/s with

the results show in Fig. 3.9. The reference gust velocities end up being very large when compared to the aircraft's velocity of 12.2 m/s, but the resulting maximum gust amplitude in the time simulation is still smaller than the aircraft cruise speed. The figure shows that, as expected, larger gust amplitudes induce larger output responses. Additionally, the plots show that the response to varying gust amplitudes is nonlinear. If this were a linear system, the elastic and rigid body responses to different gust amplitudes would scale linearly. For example, one would expect the response to a 20-m/s amplitude gust to be double that to a 10-m/s amplitude. However, this is not seen in these plots. The 20-m/s and 30-m/s responses of the maximum speed deviation and root curvature roughly scale up linearly, but the 40-m/s response does not scale linearly for any of the outputs examined. The speed, curvature and pitch plots show that the 40-m/s response is less than the four times amplification from the 10 m/s case that would be expected in linear simulations and are, respectively, 3.55, 3.67 and 2.91 times the 10-m/s responses. The altitude plot shows the opposite trend, with higher values than those expected from a linear scaling. The 20, 30 and 40-m/s altitudes are, respectively, 2.40, 3.86 and 5.06 times the 10-m/s response. Even though the gust disturbances could be considered large, the outputs examined remain within the equilibrium region of attraction, meaning that the states return to their trimmed values after the gust returns to zero.

To study the effect that varying stiffness parameters has on the aircraft gust response, various open loop response metrics are developed and plotted as a function of the flexible mode (bending, torsion, in-plane bending) frequencies for each of the simulation models described above. The gusts used for this study are DARPA profile gusts, as described in Section 2.3.2 with a 10-m/s reference velocity and 2-s, 4-s and 8-s gust durations. The results are also plotted as a function of the various ratios of these frequencies. Additionally, due to the fact that the phugoid frequency is also varying with the different aircraft models, the results are also plotted as a function of the ratio of the phugoid frequency to the three flexible mode frequencies. Linear fits are also plotted for all the data to help determine any

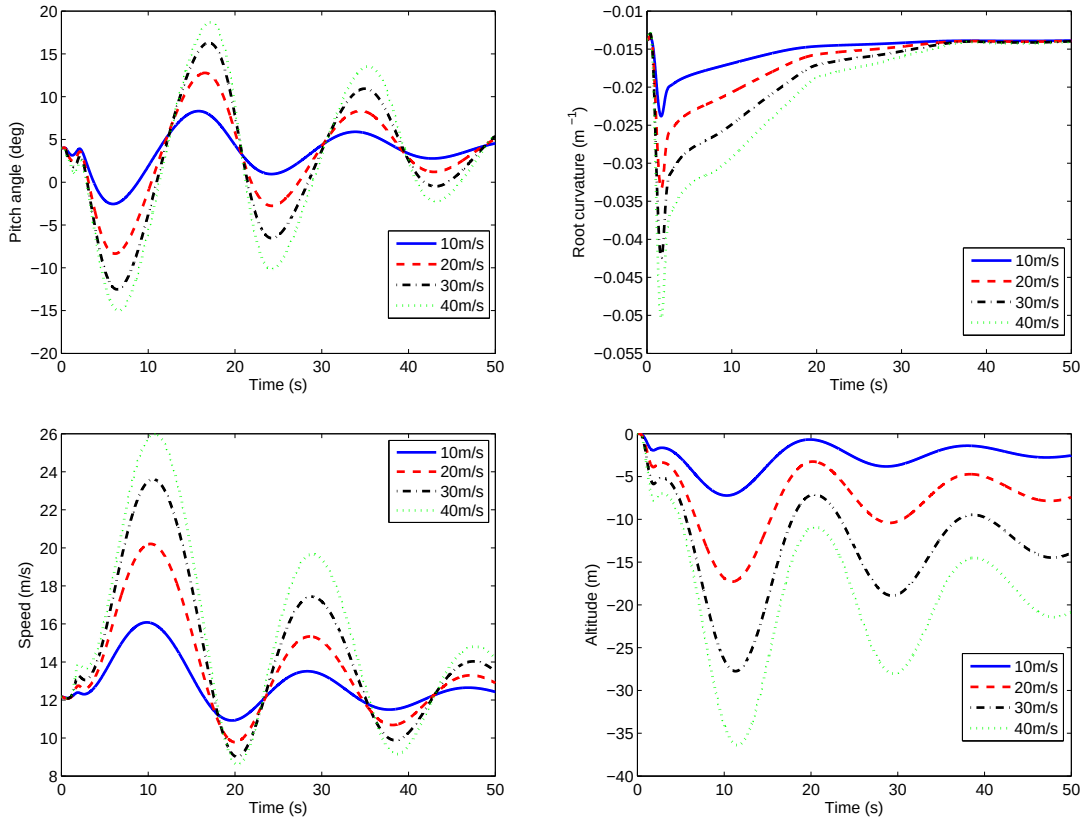

Figure 3.9: Gust response of baseline flying wing model to gust reference velocities of 10, 20, 30 and 40 m/s.

trends that may be present. To determine how well the linear fit is to the data, the coefficient of determination, R^2, is also shown on the plots. The coefficient of determination is given by [45]:

$$R^2 = \frac{\sigma_y^2 - \sigma_{y,x}^2}{\sigma_y^2}, \tag{3.4}$$

where σ_y is the standard deviation of y given by,

$$\sigma_y = \left[\frac{\sum_{i=1}^{n} (y_i - y_m)^2}{n-1} \right]^{\frac{1}{2}}, \tag{3.5}$$

and

$$\sigma_{y,x} = \left[\frac{\sum_{i=1}^{n} (y_i - y_{ic})^2}{n-2} \right]^{\frac{1}{2}}, \tag{3.6}$$

where y_i are the actual values of y, y_ic are the values computed using the linear fit and y_m is the mean values of all the samples of y. A value of $R^2 = 1$ indicates that the linear fit matches the measured data exactly, and $R^2 = 0$ indicates no correlation between the linear fit and the measured data.

The maximum pitch angle for each simulation, as well as the trim pitch angle in still air (denoted as no gust), are plotted in Fig. 3.10. Only the results which show identifiable trends are presented. The data show that as the ratio of the phugoid to the 1^{st} bending and in-plane bending ratios, as well as the ratio of the 1^{st} torsion to 1^{st} in-plane bending frequencies increase, the maximum pitch angle decreases. On the other hand, as the 1^{st} bending and 1^{st} in-plane bending frequencies increase, the maximum pitch angle also increases. VFA tend to have phugoid to 1^{st} bending frequencies that approach one, indicating that there could be coupling between elastic and rigid body modes. Combining these facts, it is clear that as the frequency ratios increase, indicating that the aircraft is becoming more flexible, the maximum pitch angle decreases. This is due to the fact that the gust disturbance has a finite amount of energy it can inject into the system. When the aircraft is less flexible, more of this energy is absorbed by the rigid body modes, resulting in a larger

pitch angle in this case. However, when the aircraft is more flexible, a larger portion of the energy is converted into the elastic modes.

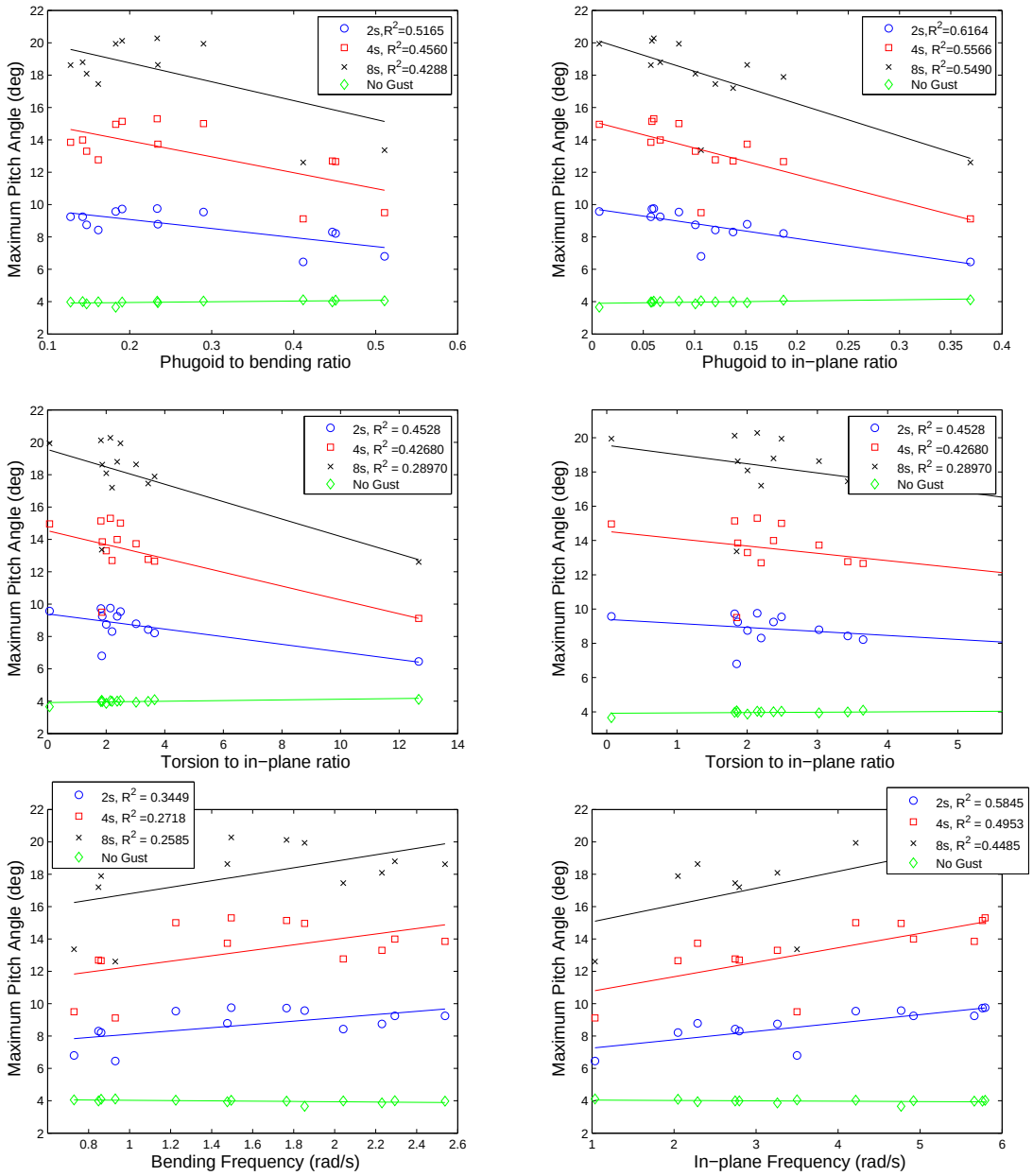

Figure 3.10: Maximum pitch angle for flying wing configuration.

Next, the maximum root curvature caused by the gust is studied. The data tend to be more scattered than the pitch angle plots, with most plots showing no discernible trends. The two plots which did show trends were the phugoid to 1^{st} bending frequency ratio and the 1^{st} bending frequency, which are shown in Fig. 3.11. The plots show that as the wing

becomes more flexible, a higher root curvature value is achieved, as expected for a vehicle with this payload. This trend can also be seen in the trimmed values, with higher trim curvature values found in the models with higher flexibility. The fact that only the plots directly related to the 1^{st} bending mode shown any real trend means that the root curvature achieved during an encounter with gust is fundamentally a function of the bending stiffness.

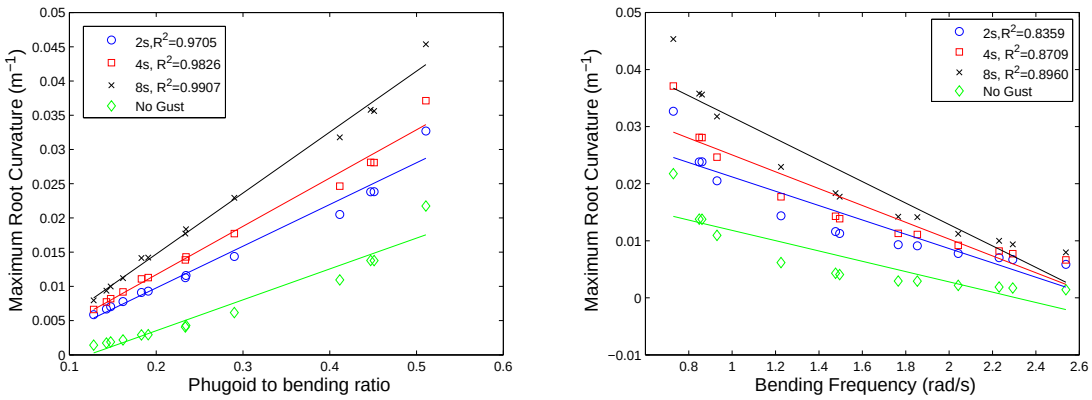

Figure 3.11: Maximum root curvature for flying wing configuration.

The results seen in the curvature plots are in direct contrast to the results seen in Fig. 3.10. In order to reduce pitch excursions during gust, a more flexible aircraft is desired, however, that will lead to larger curvature values, and, therefore, larger bending moments. This represents one of many tradeoffs that a VFA designer must make. It is reasonable to believe that the designers, in the absence of any additional information, would choose to make a stiffer wing and therefore accept the penalty of larger rigid body motion during an encounter with turbulence. It should also be noted that away from the ground, rigid body motions would probably present less of a safety of flight risk than large wing deformations.

To get a better idea the strength of the aircraft, the bending moment was plotted as a function of bending frequency, shown in Fig. 3.12. The trend is the opposite as is shown in Fig. 3.11. The stiffer models have larger bending moments than the more flexible models. This shows that the more flexible models are able to alleviate the gust energy by deforming more than the stiffer models for the same gust excitation.

To further explore the relationship of maximum pitch angle to maximum curvature of

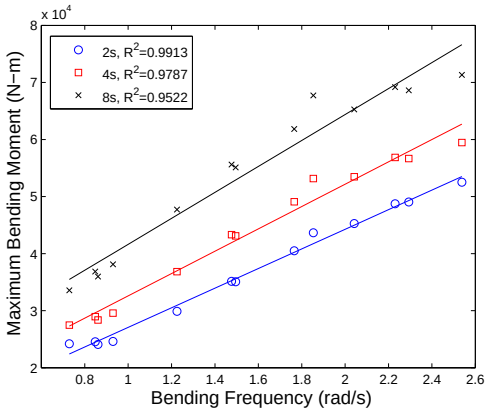

Figure 3.12: Maximum bending moment for flying wing configuration.

the simulation models during a gust encounter, the maximum pitch angle is plotted versus the maximum curvature in Fig. 3.13. The plots show a strong relationship between these two parameters with the models with the lowest maximum curvature having the highest pitch angle. This further illustrates the fact that the amount of gust energy converted to either rigid body or elastic modes is highly dependent on aircraft stiffness parameters.

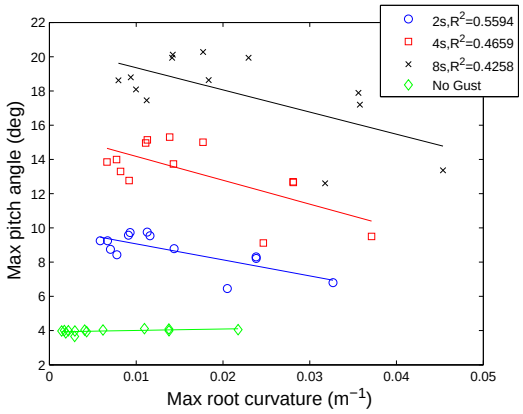

Figure 3.13: Maximum pitch angle versus maximum root curvature for the flying wing configuration.

An attempt was made to reproduce the results shown in Fig. 3.10, by modifying the worst performing model in pitch, model 10. The in-plane stiffness was lowered to 4 x 10^7 and the model was given an 8-s gust. The maximum pitch angle was only lowered from $20.28°$ to $19.82°$. When the in-plane stiffness was once again lowered to 2 x 10^7, the

maximum pitch angle was 20.19°, which is only slightly better than the original case, and worse than the case with an in-plane stiffness of 4 x 10^7. This shows that improving aircraft response is not as simple as modifying the flying wing properties based on the trends shown in the plots above.

3.2.4 X-HALE Open Loop Sensitivity

In order to examine the sensitivity of the X-HALE aircraft's stability and gust response to variations in stiffness properties, the stiffness matrix values were varied similarly to Section 3.2.1 to create X-HALE simulation models. The X-HALE stiffness variations used are shown in Table 3.8. Once again, there was a lower limit on the bending stiffness, below which an accurate trim of the aircraft could not be obtained.

Table 3.8: X-HALE Model Property Variations

PARAMETER	VARIATION	% CHANGE
Bending stiffness	30 - 1000 $N \cdot m^2$	26.7% - 893%
Torsional stiffness	5 - 550 $N \cdot m^2$	9% - 985%
In-plane bending stiffness	635 - 63500 $N \cdot m^2$	10% - 1000%

3.2.5 Stability Study

Unlike the flying wing model, the X-HALE flight dynamic modes are closer to the classical rigid body modes, consisting of the short period, phugoid, Dutch Roll, roll and spiral. Therefore, this gives two more frequencies, the short period and Dutch Roll, to examine. The torsional, bending, and in-plane bending stiffnesses were varied to study their effect on the flight dynamic modes. Variations in the in-plane bending stiffness only resulted in a negligible change in flight dynamic modes. The results for the torsional and bending stiffness are shown in Figs. 3.14 - 3.16. In these figures, the green squares represents the lowest value used, the red triangle represents the baseline value and the black diamond represents the rigid case.

The phugoid data shown in Fig. 3.14 indicate that an increase in torsional stiffness is destabilizing, while an increase in bending stiffness is stabilizing. The fact that an increase in torsional stiffness is destabilizing is counterintuitive. This is possibly due to the fact the the torsional and bending stiffnesses begin to approach each other allowing for an exchange in energy between the two modes, which would have a de-stabilizing effect. Additionally, variations in bending stiffness have a much larger affect on the phugoid mode than do variations in the torsional stiffness. In all cases, the phugoid remains stable. The phugoid frequency, given by the imaginary part of the poles, remains almost constant in both cases.

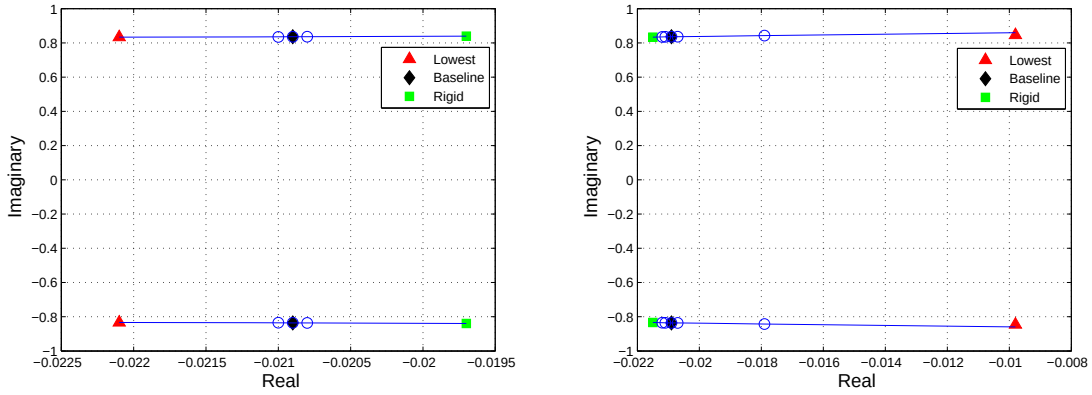

Figure 3.14: X-HALE phugoid poles as a function of torsional stiffness (left), bending stiffness (right).

The short period poles as the torsional and bending stiffness are varied are shown in Fig. 3.15. Similar to the phugoid poles, increased torsional stiffness causes a decrease in damping, while increased bending stiffness causes an increase in damping, although the poles remain well away from the stability boundary. The data also show that variations in torsional stiffness can result in small changes in short period frequency, while variations in bending stiffness can have a large effect on the short period frequency. In fact, the frequency corresponding to the lowest bending stiffness is approximately half that of the rigid case.

The Dutch Roll poles are shown in Fig. 3.16. Once again, increased torsional stiffness is destabilizing on the Dutch Roll mode, with the frequency remaining almost constant.

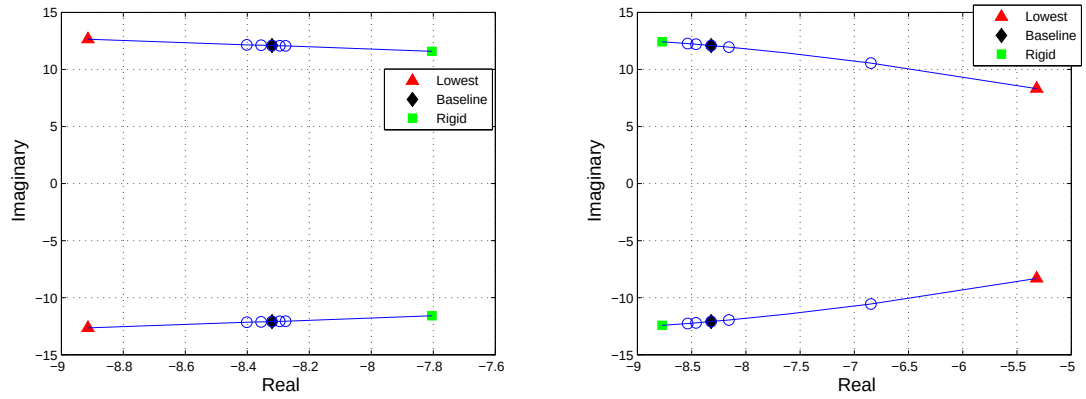

Figure 3.15: X-HALE short period poles as a function of torsional stiffness (left), bending stiffness (right).

Increased bending stiffness is destabilizing at first, but then below some stiffness value becomes stabilizing. The frequency of the poles also begins to decrease. This behavior is similar to what is seen with the flying wing model, indicating that as the X-HALE becomes more flexible in bending, its Dutch Roll behavior approaches that of the flying wing.

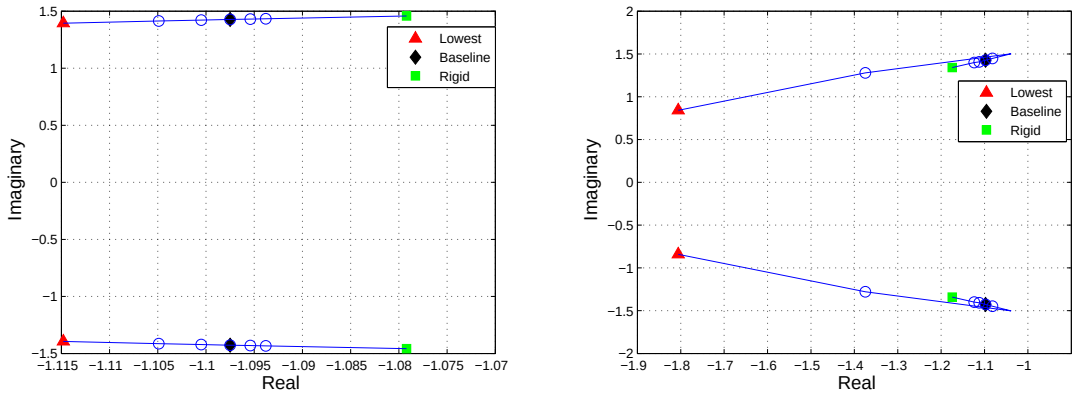

Figure 3.16: X-HALE Dutch Roll poles as a function of torsional stiffness (left), bending stiffness (right).

Once the upper and lower bound for the three stiffness parameters were determined, Latin hypercube sampling was once again used to create ten simulation models. The stiffness parameters for the aircraft models are shown in Table 3.9.

The flight dynamic modes for the various X-HALE models are shown in Table 3.10. With the exception of model 3, which corresponds to the lowest bending stiffness, all of

Table 3.9: X-HALE Stiffness Properties (Extensional = 2.14 x $10^6 N$)

MODEL	BENDING $(N \cdot m^2)$	TORSIONAL $(N \cdot m^2)$	IN-PLANE BENDING $(N \cdot m^2)$
Baseline	112.00	55.80	6350
1	355.05	81.28	13937
2	252.62	381.38	62827
3	33.20	192.24	40422
4	883.70	208.47	46218
5	569.03	285.62	7135
6	462.62	186.32	36474
7	696.39	485.53	56968
8	784.27	530.22	22707
9	907.27	92.53	5406
10	166.58	420.84	31420

the X-HALE models exhibit the classical phugoid, short period, and Dutch Roll modes. Model 3 has a pair of real poles for the Dutch Roll mode, similar to the flying wing model. With the exception of the spiral mode, all of the flight dynamic modes are stable. The spiral mode, characterized by a slow banking motion [42], is only stable for the baseline and model 3 aircraft, which are also the aircraft with the lowest bending stiffness. The flight dynamics for model 3 vary significantly from those of the other X-HALE models. It has a phugoid mode that is barely stable, a short period with a significantly lower frequency and damping than the other models, and a non-oscillatory Dutch Roll mode. An examination of the eigenvectors also shows that model 3 has more of a contribution from the first bending mode than of the phugoid mode.

Table 3.10: X-HALE Flight Dynamic Properties

MODEL	PHUGOID	SHORT PERIOD	DUTCH ROLL	ROLL	SPIRAL
Baseline	$-0.0209 \pm 0.836i$	$-8.320 \pm 12.096i$	$-1.098 \pm 1.427i$	-7.49	-0.0015
1	$-0.0214 \pm 0.834i$	$-8.668 \pm 12.376i$	$-1.149 \pm 1.373i$	-7.45	0.0291
2	$-0.0205 \pm 0.837i$	$-8.245 \pm 11.962i$	$-1.133 \pm 1.397i$	-7.32	0.0208
3	$-0.0030 \pm 0.871i$	$-4.725 \pm 7.203i$	$-2.3857, -1.7425$	-7.39	-0.0453
4	$-0.0213 \pm 0.833i$	$-8.736 \pm 12.417i$	$-1.165 \pm 1.359i$	-7.42	0.0385
5	$-0.0213 \pm 0.833i$	$-8.709 \pm 12.403i$	$-1.159 \pm 1.367i$	-7.43	0.0346
6	$-0.0213 \pm 0.834i$	$-8.695 \pm 12.394i$	$-1.155 \pm 1.370i$	-7.43	0.0322
7	$-0.0206 \pm 0.836i$	$-8.369 \pm 12.036i$	$-1.160 \pm 1.370i$	-7.27	0.0373
8	$-0.0207 \pm 0.836i$	$-8.375 \pm 12.040i$	$-1.162 \pm 1.369i$	-7.26	0.0383
9	$-0.0214 \pm 0.834i$	$-8.742 \pm 12.416i$	$-1.165 \pm 1.356i$	-7.44	0.0387
10	$-0.0203 \pm 0.838i$	$-8.104 \pm 11.851i$	$-1.116 \pm 1.1420i$	-7.34	0.0079

The fundamental elastic modes of the X-HALE models are shown in Table 3.11. The frequencies are generally higher than those of the flying wing models. The separation between the phugoid mode and the first bending frequency ranges from 0.18 Hz for model 3 to 1.55 Hz for model 9. In all cases, the bending frequency is the lowest and only model 5 has an in-plane bending frequency lower than its torsional frequency.

Table 3.11: X-HALE Fundamental Elastic Frequencies (Hz) about the Aircraft's Undeformed Configuration

MODEL	1^{st} BENDING	1^{st} TORSIONAL	1^{st}IN-PLANE BENDING
Baseline	0.59	2.62	4.04
1	1.06	3.17	6.31
2	0.89	6.86	7.38
3	0.32	4.89	11.00
4	1.67	5.07	10.6
5	1.34	5.99	4.29
6	1.21	4.79	7.66
7	1.48	7.73	12.20
8	1.57	7.78	8.17
9	1.69	3.32	3.65
10	0.72	7.18	9.47

The trim parameters for the X-HALE models are shown in Table 3.12. There is a large variation in trim shape of the models, as evidenced by the large variation in wingtip deflection. The values vary from 0.20 m for model 9, which is close to the jig shape value of 0.17 m, to 1.12 m for model 3, which is 31% of the half span in addition to the jig shape value. The models with the larger tip deflections also have larger angles of attack which are needed to account for the larger component of the lift acting in the horizontal direction. The exception is model 9, which has a relatively large angle of attack, despite having the smallest trim tip deflection. Model 9 has also torsional and in-plane bending frequencies which are close to each other, with the lower being the in-plane bending frequency. For all the models the elevator deflection is negative indicating trailing edge up.

Table 3.12: X-HALE Trim Parameters

Model	Angle of Attack (deg)	Elevator Deflection (deg)	Thrust per Motor (N)	Wingtip Deflection (m)	Half span Deflection %
Baseline	1.71	-0.15	1.3	0.38	12.7
1	1.38	-0.13	1.31	0.24	8.0
2	0.95	-0.26	1.31	0.28	9.3
3	1.92	-0.51	1.30	1.12	37.3
4	1.02	-0.18	1.31	0.23	7.7
5	0.97	-0.20	1.31	0.22	7.3
6	1.06	-0.19	1.31	0.23	7.7
7	0.87	-0.22	1.31	0.21	7
8	0.89	-0.22	1.31	0.21	7
9	1.30	-0.12	1.31	0.20	6.7
10	0.98	-0.30	1.31	0.34	11.3

3.2.6 Gust Response Study

In a similar fashion to Section 3.2.1, the models were simulated with gust disturbances of 2 s, 4 s, and 8 s and a reference velocity of 5 m/s. For the X-HALE models, the gust was considered to be constant along the span. In this case, the results were plotted as a function of not only the phugoid mode, but also the short period and Dutch Roll, as well as the elastic frequencies and various frequency ratios.

The maximum pitch angle for each simulation is shown in Fig. 3.17. As opposed to the flying wing model, the X-HALE models have the largest pitch angle response to a 2-s gust. This is because of the fact that the phugoid frequencies of the X-HALE are closer to the frequency of the gust. The torsional frequency also plays a much larger role than it did in the flying wing models. The maximum pitch angle shows a strong dependence on the phugoid-to-torsion and short period-to-torsion ratios. The maximum pitch angle decreases as the torsional, bending, and in-plane bending frequencies increase, indicating that the stiffer models have lower maximum pitch angles, although the data are somewhat scattered in the bending and in-plane bending cases. Additionally, an increase in the bending-to-torsional frequency ratio causes an increased maximum pitch angle.

The maximum root curvature of the X-HALE models during the gust disturbances is

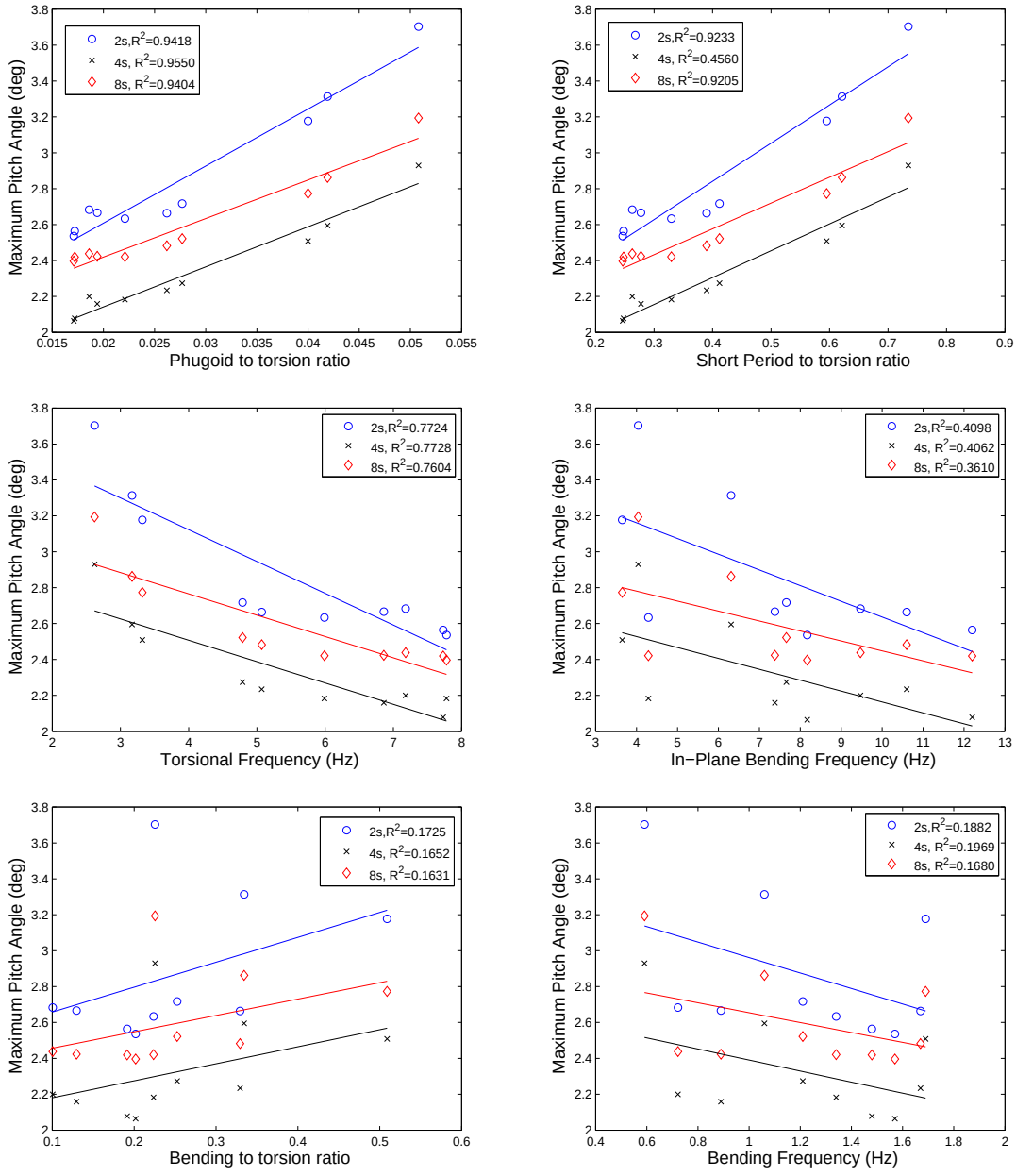

Figure 3.17: Maximum pitch angle for X-HALE models under uniform gust disturbances.

shown in Fig. 3.18. The maximum root curvature has a very strong dependence on the bending stiffness. As the models get more flexible in bending, the maximum root curvature increases, as expected. Additionally, as the phugoid frequency increases, the maximum root curvature also increases. For all three gust disturbances, model 9 had the lowest root curvature and pitch angle.

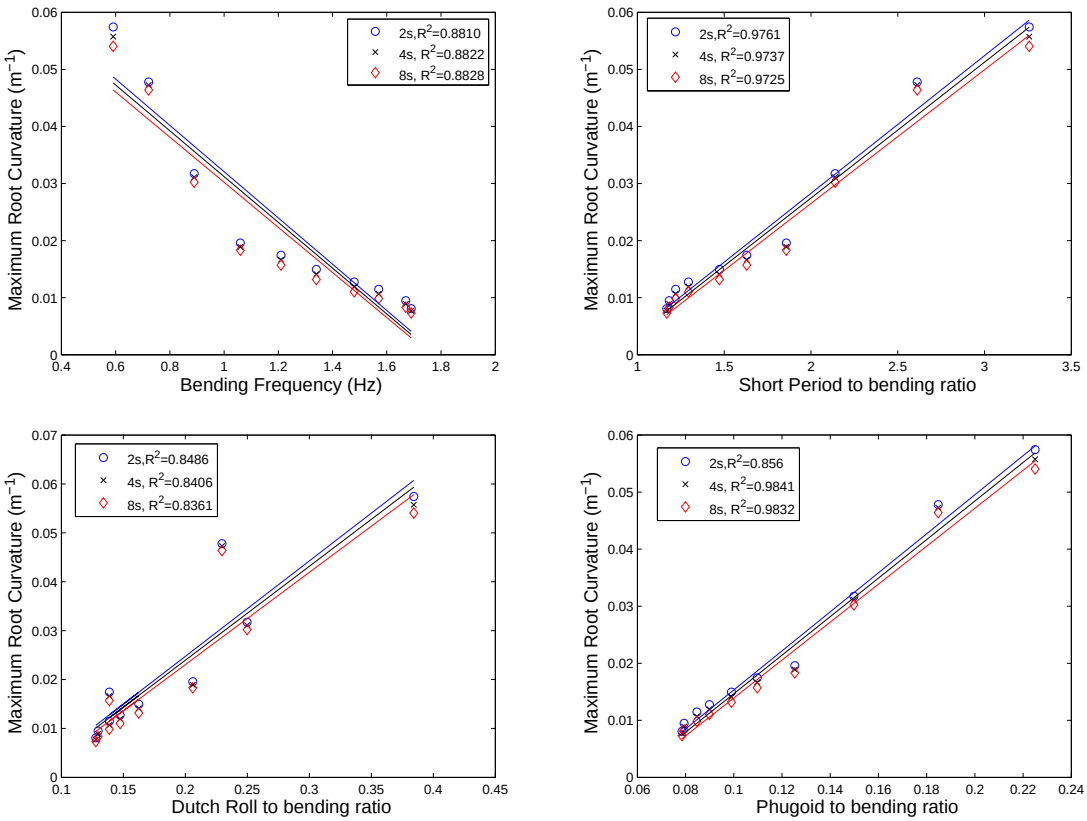

Figure 3.18: Maximum root curvature for X-HALE.

Next, the maximum pitch angle is plotted as a function of the maximum root curvature in Fig. 3.19. The plot shows that, unlike in the flying wing model, the lowest pitch angle and root curvature occur in the same model, model 8. Examining Table 3.9, model 8 has a high bending stiffness, which accounts for the low curvature value, and the highest torsional stiffness values. Fig. 3.17 shows that models with a higher torsional stiffness have smaller maximum pitch angles, as confirmed by model 8 response. This is due to the fact that assuming the elastic axis is not the same as the aerodynamic center, an aircraft

that has a lower torsional stiffness will have a larger elastic twist for the same aerodynamic load, necessitating a larger pitch angle to make up for the loss of lift due to the larger deformation.

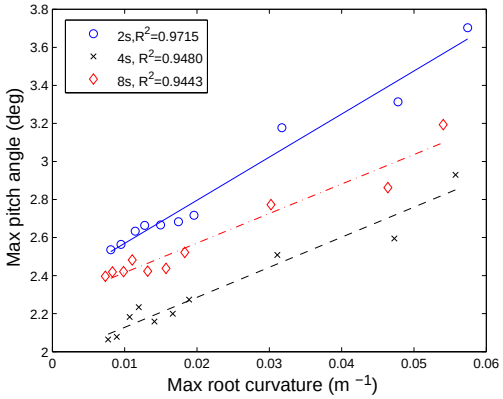

Figure 3.19: Maximum pitch angle as a function of maximum root curvature for X-HALE under gust disturbances.

Similarly to what was done for the flying wing, an attempt to re-create the results in Figs. 3.17 and 3.18 was made. First, the in-plane stiffness of the baseline model was raised, but this resulted in virtually no change to the maximum pitch angle or maximum root curvature. Next, the torsional stiffness was incresed from 55.8 to 400 N-m. As predicted by Fig. 3.17, this resulted in a decrease in pitch angle form the original value of $3.703°$ to $2.744°$, a decrease of 26%. Additionally the maximum root curvature was decreased from 0.0046 to 0.0031 m^{-1} a decrease of 31%.

3.3 Closed Loop Sensitivity

Due to the fact that the VFA are most likely going to be unmanned, as well as for other reasons, the aircraft will be flying under feedback control. Therefore, various measures of closed loop performance for the simulation models are also studied.

3.3.1 Flying Wing Closed Loop Sensitivity

The size of the flying wing model, 531 states, presented problems for the numerical linearization routine within UM/NAST, and an accurate linearized model could not be obtained. The linearization computed analytically by UM/NAST contained multiple high frequency, unstable modes which made linear simulations impossible. We note that these unstable modes were not observed in nonlinear simulations. Therefore, the MATLAB system identification toolbox was used to fit 20^{th} -order linear models to the nonlinear simulation data. The gust inputs used in the identification are the same as those described in Sec. 3.2.1 , along with three 50-s duration sine sweeps with beginning frequencies ranging from 0.05 - 0.11 Hz and final frequencies ranging from 0.06 - 0.39 Hz. The models each have three control inputs: the elevators, which are constrained to move as a single surface, as well as the ailerons, which can move independently of each other. The elevator and ailerons were identified using 1-s and 5-s control surface doublets. The choice of 20^{th} -order models was made as a tradeoff between nonlinear data matching and the desire to use the lowest order possible. For each model, several different linearizations were created, with the one matching the nonlinear data best chosen. At first, there was some difficulty matching curvature data due to scaling of output units. The curvature values were at least two orders of magnitude lower than the other outputs. To correct this, the curvature values were multiplied by 100, the identification performed, then the resulting C matrix rows were divided by 100 to remove this bias. A comparison between nonlinear data and the linearized model is presented in Fig. 3.20. The linear model captures the nonlinear behavior fairly well, although the magnitude of the minimum for both the root curvature and the pitch angle is underestimated by the linear model.

One measure of controllability for a linear system is the control effort required to drive the aircraft from an initial pitch angle of 0° to a final pitch angle of 10°. To derive the control effort required, consider an LTI system representing model linearization at a selected

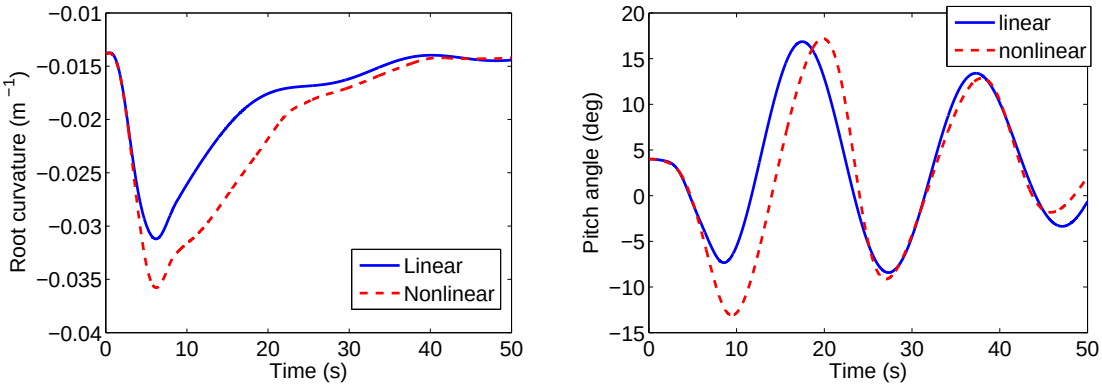

Figure 3.20: Comparison between nonlinear and linearized data of baseline flying wing model with 8-s duration gust.

operating point,

$$\dot{x} = Ax + Bu \tag{3.7}$$

$$y = Cx + Du \tag{3.8}$$

$$x(0) = x_0 \tag{3.9}$$

where x ais the vector state of the system and u is the control input vector. A state of Eq. 3.7 is said to be controllable if there exist a control, u, such that an arbitrary final state can be achieved from this initial state over a given time interval [46]. The system in Eq. 3.7 is called completely controllable if all states are controllable. One test for controllability is that the controllability gramian, W satisfies:

$$W = \int_0^\infty e^{A\tau} B B^T e^{A^T \tau} d\tau > 0 \tag{3.10}$$

where the greater-than sign denotes positive definiteness. Many texts present Eq. 3.10 in a slightly different manner by saying that W must be nonsingular. These two definitions are equivalent because W is always semi-definite, therefore it is positive definite if, and only if, it is non-singular [47]. In most control applications, the full set of states is not available for feedback, but rather only a subset of outputs. Therefore, the notion of output controllability

is useful. Similar to the definition of state controllability, an output is controllable if there exists a control such that an arbitrary final state can be achieved from an initial output at the origin in finite time. One test for output controllability is that the output controllability gramian, defined as

$$W_{output} = CWC^T, \tag{3.11}$$

is positive definite.

The minimum control effort (in an internal square sense) required to drive a system from the origin to a specified final state, x_f, assuming free arrival time, is given by [48]

$$E = x_f^T W^{-1} x_f \tag{3.12}$$

If one is interested in driving the system from an initial zero output to a final output y_f, the output control effort can be defined as:

$$E_{output} = y_f^T W_{output}^{-1} y_f. \tag{3.13}$$

The quantity in Eq. 3.13 can be useful when the states lose their physical meaning (e.g., after system identification or when normal modes are used).

The control effort needed to move the aircraft models from an initial pitch angle of 0° to a final pitch angle of 10° was calculated based on Eq. 3.13. The results, normalized to the largest value, are plotted in Fig. 3.21, using the same models as were used for the open loop study. The data for model 1 is not included on the plots, because it was a significant outlier. The data are somewhat scattered, but there are some trends. The output control effort is dependent on the models bending stiffness. As the bending stiffness decreases, the control effort increases. A model that is more flexible in bending, will convert more control energy into the elastic modes than a stiffer model. Therefore, to cause a change in a rigid body mode, such as pitch angle, more control energy must be injected into the

system. Additionally, the data show that output control effort increases as the phugoid-to-1^{st} in-plane bending frequency ratio increases and it decreases with an increase in the 1^{st} bending-to-1^{st} torsion frequency ratio.

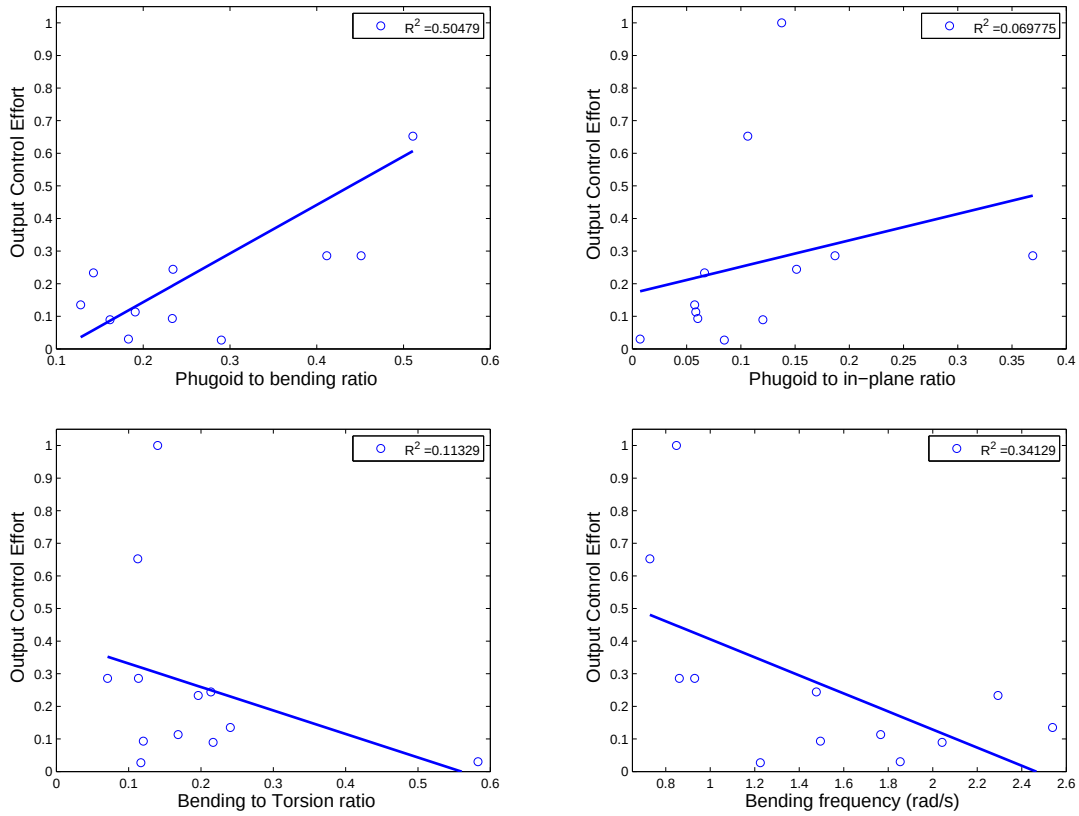

Figure 3.21: Output control effort to move flying wing aircraft models from 0° to 10° pitch angle.

In order to get a measure of the relative closed loop controllability of the aircraft models, a pitch tracking LQG with an integrator added on pitch error was created for each aircraft model. The controller was first tuned on the baseline model in order to minimize the overshoot and settling time to pitch angle commands. State cost was applied to all outputs with the cost of the pitch angle half that of other outputs. Once acceptable performance was obtained on the baseline model, separate controllers were then created for each aircraft model using the same Q and R matrices. An alternative approach, which could perhaps give a better comparison of aircraft controllability, would have been adjusting R until the value of the control cost is the same as for the reference model, but this was not pursued.

The Q used was equal to all zeros, with the weight on the pitch angle error integral state equal to 10^4 and R was set to 10^{-3}.

The aircraft were then given a pitch step command of amplitude 2°. As an example of the aircraft response, a plot of the two models with the highest and lowest overshoot are shown in Fig 3.22. Neither actuator dynamics were included nor control surface deflection or rate limits were considered, allowing for high bandwidth control response of a linear model.

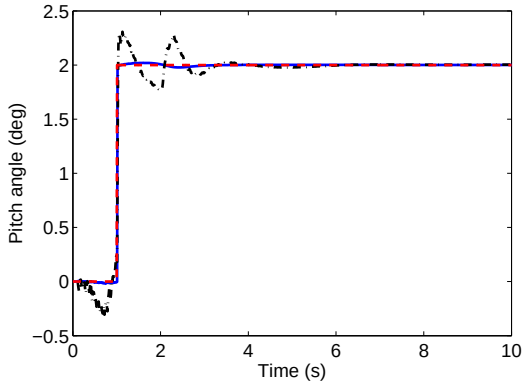

Figure 3.22: Pitch tracking response of linear flying wing aircraft models with highest and lowest overshoot.

The first closed loop parameter studied is the maximum overshoot, which is shown in Fig. 3.23. For these cases the data were scattered, but there were some trends that were evident. The plots show that as the 1^{st} bending-to-1^{st} in-plane bending, as well as the 1^{st} bending-to-1^{st} torsion frequency ratios increase, the maximum overshoot also increases. Assuming the bending frequency was set, this means that a designer could reduce overshoot to longitudinal pitch commands by making the aircraft structure stiffer in either torsion or in-plane bending.

The next parameter of the aircraft model response studied was the settling time, which is defined to be the time when the aircraft pitch angle enters and stays within an area bounded by $\pm 2\%$ of the desired response. The settling time results are shown in Fig. 3.24. The settling time decreases as the ratio of the phugoid to all three frequency ratios increases. It also

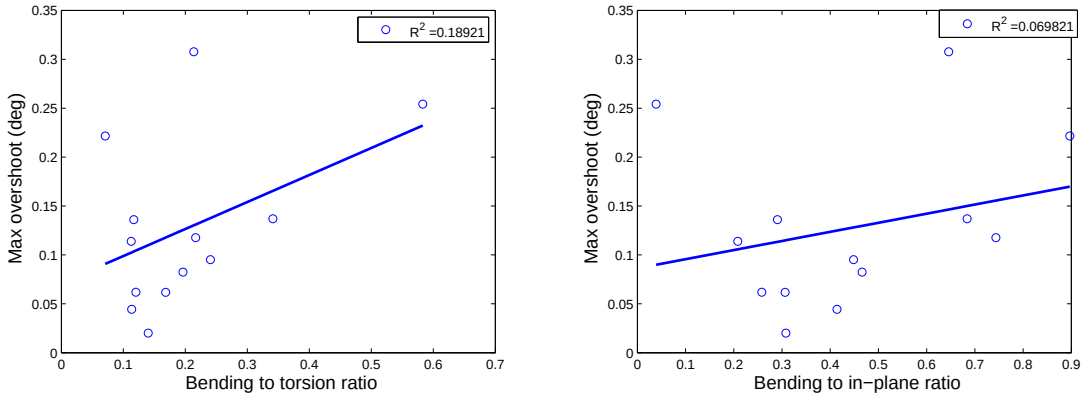

Figure 3.23: Maximum overshoot of linearized flying wing model to a 2° pitch command using LQG control.

shows that settling time increases with an increase in 1^{st} bending frequency. It is hypothesized that as the aircraft model gets stiffer, the settling time increases; the wing flexibility tends to act as a damper in the more flexible aircraft allowing for smaller oscillations.

3.3.2 X-HALE Closed Loop Sensitivity

In contrast to the flying wing model studied in Section 3.3.1, UM/NAST was able to find an analytical linearization for the X-HALE model. A comparison between the linearized and nonlinear responses to a 1° elevator step command are shown in Fig. 3.25. There is a very good agreement between the linear and nonlinear models for the pitch angle, θ, and the flight speed. The agreement is not as good for the root curvature: the linearized response does match the overall trends, but the amplitude of the oscillations is an order of magnitude smaller. The amplitude of the oscillations is not important to the current study, because none of the metrics used take this into account. Only the maximum root curvature is used, and while the linear model does under-predict this value, the fit was deemed good enough for use in this study.

The output control effort needed to move the X-HALE models from an initial pitch angle of 0° to final pitch angle of 10° was calculated in a similar fashion to Section 3.3.1. The results are shown in Fig. 3.26 with the values normalized such that the maximum output

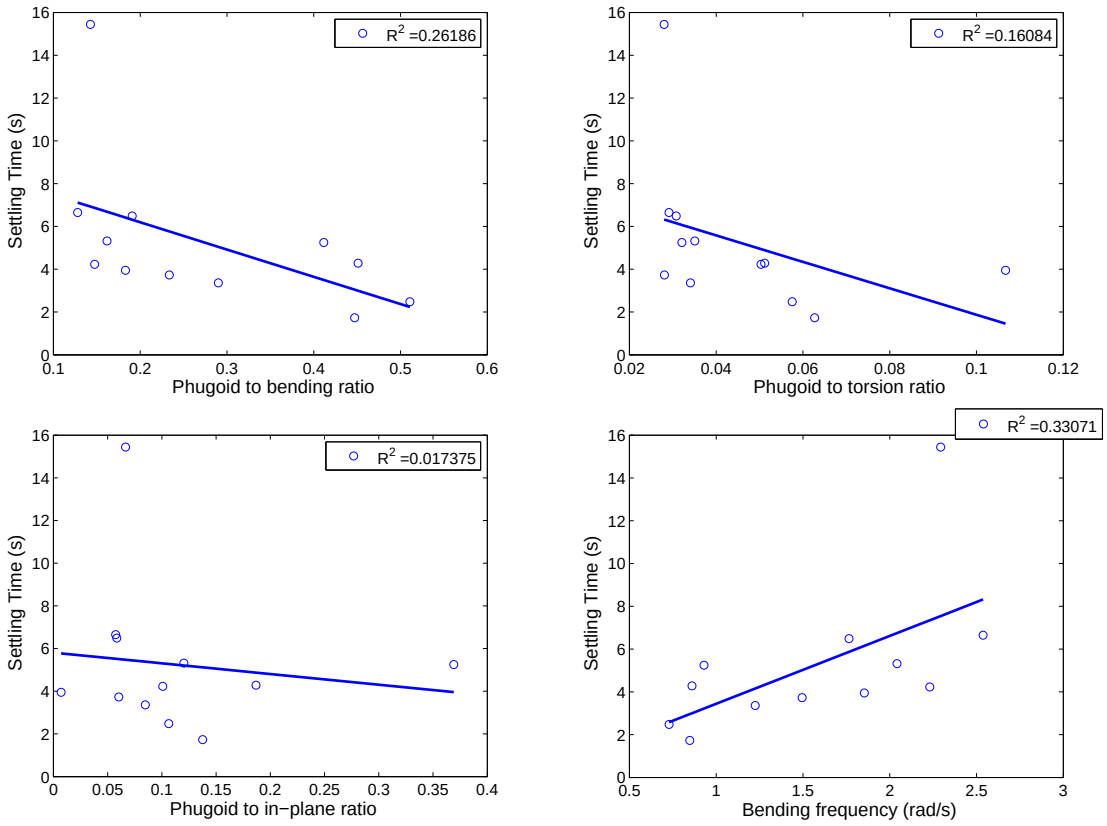

Figure 3.24: Settling time of linearized flying wing model to a 2° pitch command using LQG control.

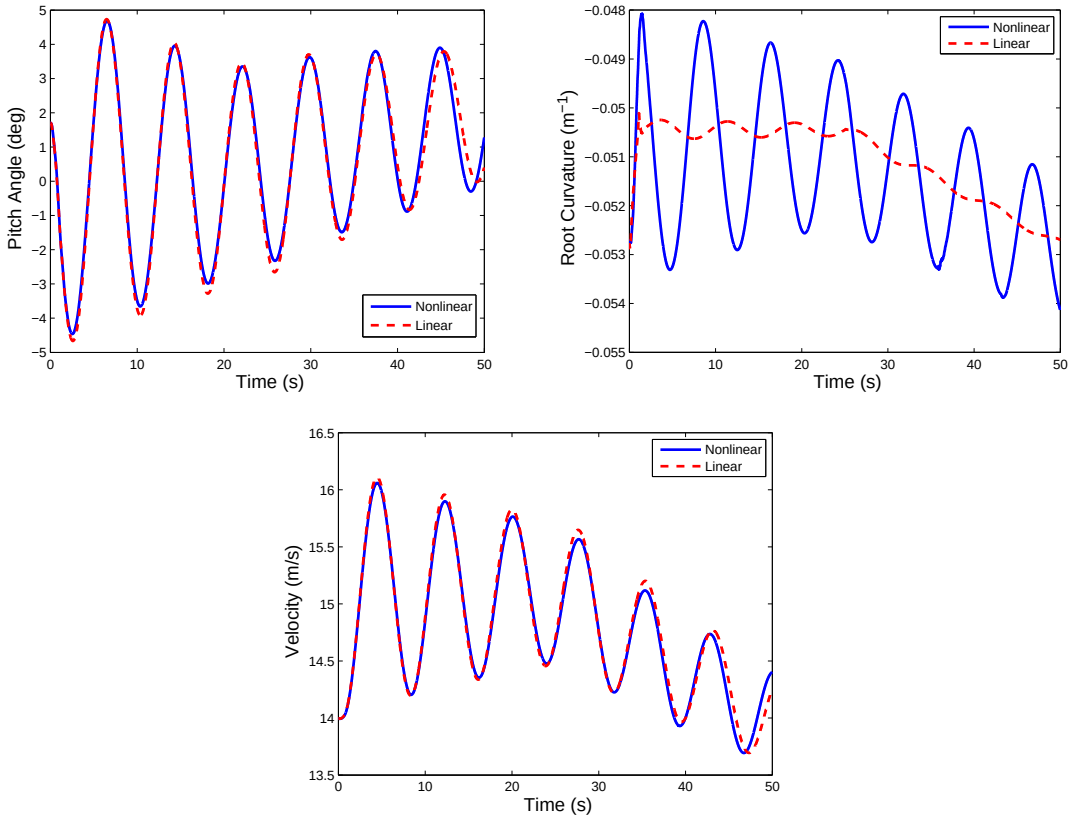

Figure 3.25: Comparison of X-HALE linearized and nonlinear response to 1° elevator deflection.

control effort equals one. There is one outlier, model 10, whose output control effort is over double that of the other models and it was neglected. The in-plane bending frequency, and some of the frequency ratios involving it, seems to play a large part in the output control effort, with models being more flexible having lower control effort. When compared to the in-plane bending frequency, the opposite trend is shown for the bending frequency, with more flexible models requiring more control effort. Additionally, models with lower bending to torsion ratios have higher control effort. These results are consistent with those in Fig. 3.21 for the flying wing aircraft. The trends seen for the bending frequency, bending to torsion ratio and phugoid to bending ratio are the same.

Pitch angle tracking LQRs, with an integrator added on pitch angle, were then designed for all of the models to measure the closed loop controllability of the linear models. The controller gain matrices, Q and R, were tuned on the baseline model in order to get good performance in terms of overshoot and settling time when responding to a 10° pitch angle step command. Once an acceptable controller was found for the baseline models, separate controllers were then created for each aircraft model using the same Q and R matrices as the baseline model. The Q matrix was set to all zeros, with the weight on the pitch angle integral state equal to 1 x 10^4 and for the R matrix, the weight on the elevators was 1 and the weight on the motors was 1 x 10^{-2}. The tracking performance of the various models is shown is Fig. 3.27. Most of the models show good tracking of the command. Model 2 is overdamped and responds very slowly and model 4 is more oscillatory and somewhat slower responding to the commands than the other models.

Even though most of the models have similar pitch angle tracking performance, the control inputs, thrust and elevator deflection, used to achieve those results are very different. The thrust commanded by the linear models while tracking pitch angle is shown in Fig. 3.28. The linearized model has no limits on thrust, so in these simulations it is assumed that negative thrust may be feasible. Additionally, the thrust is integrated to get a measure of the control energy used in the tracking. The absolute value of the thrust integral was then

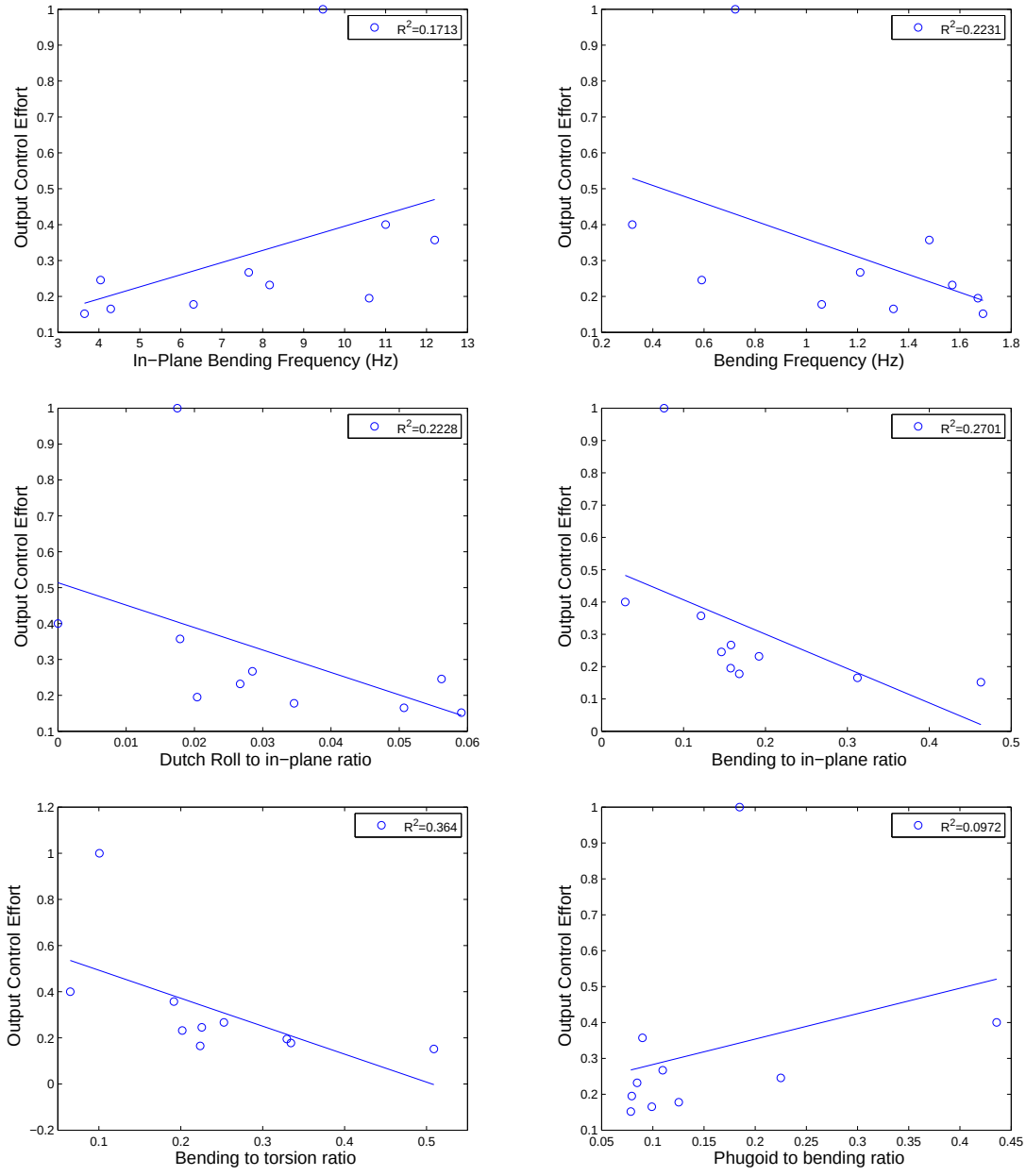

Figure 3.26: X-HALE output control effort to go from 0° to 10° pitch angle.

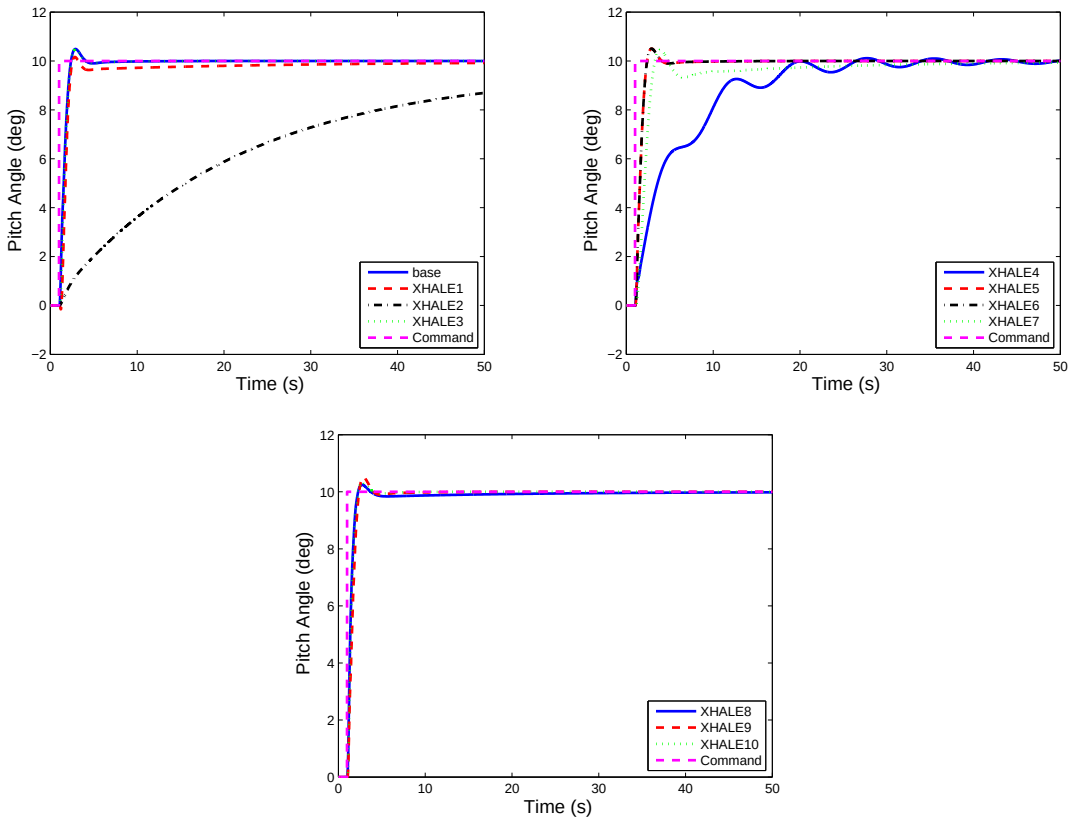

Figure 3.27: X-HALE linear models' tracking performance.

plotted as a function of the various frequencies and frequency ratios. The absolute value is used for two reasons. First, because it is assumed that it will take the same amount of energy to spin the propeller in either direction. Also, these are linear simulations meaning a negative value is with respect to the nonlinear equilibrium (trim) value. The results for the thrust integral are shown in Fig. 3.29, with the baseline model denoted by a red diamond. Additionally, the data for models 1 and 2 are excluded from the plots because the thrust integral was at least an order of magnitude larger for these models than the others. The data tended to be very scattered, with only the bending frequency and short period-to-bending ratio plots showing any trends. They show that a larger flexibility in bending results in a lower thrust.

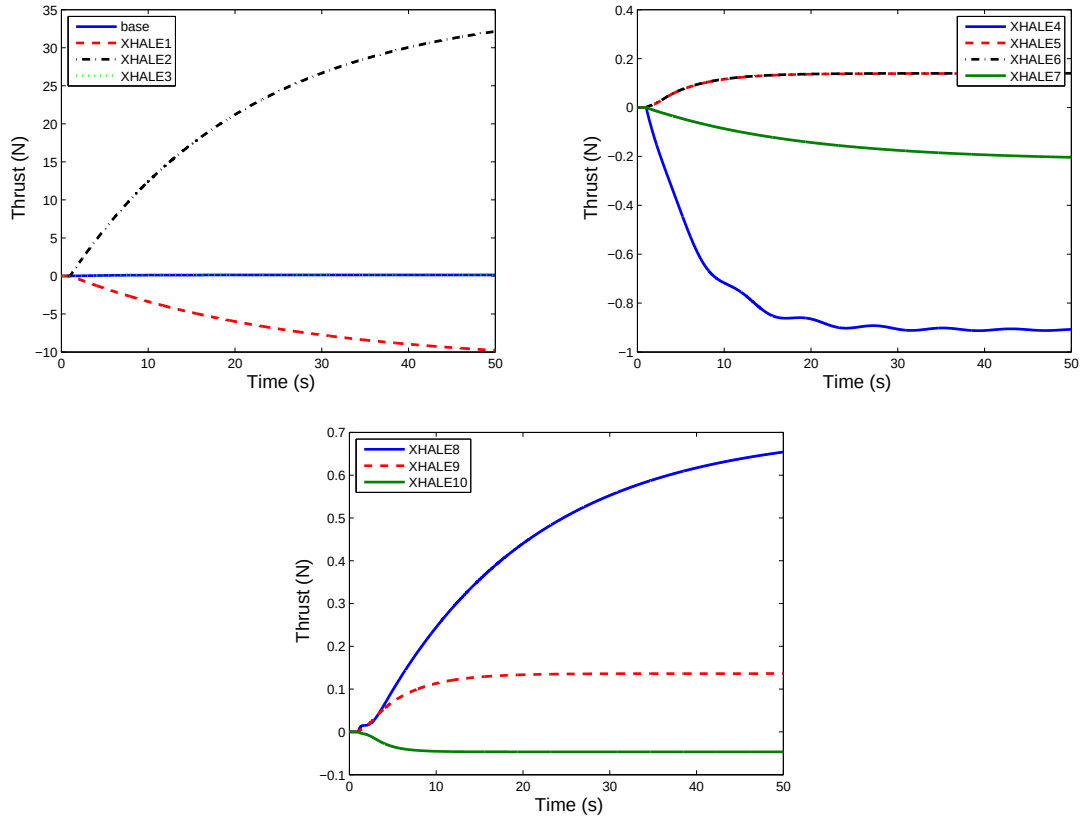

Figure 3.28: X-HALE linear models' thrust about trim state during pitch angle tracking (red diamond shows baseline case).

Next, the elevator deflection angle during the pitch angle tracking is shown in Fig. 3.30.

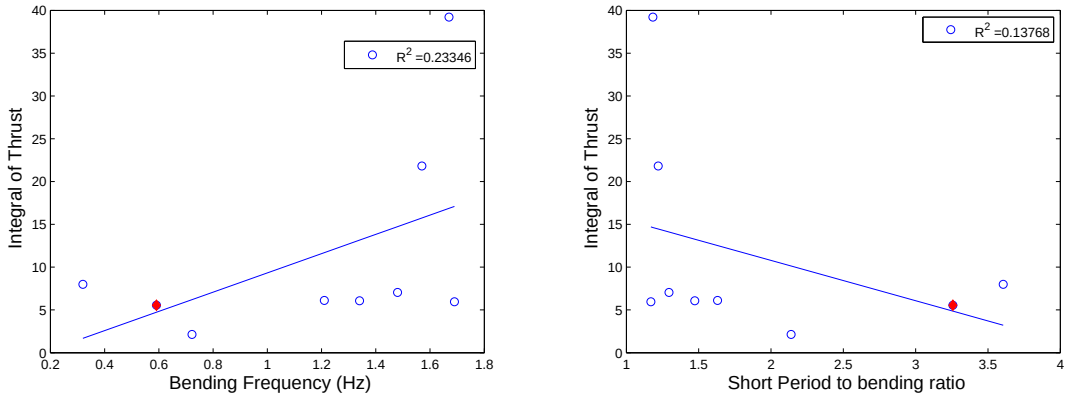

Figure 3.29: Integral of X-HALE thrust during pitch angle tracking.

Once again, the elevator deflections are significantly different across the various models, despite the tracking performance being similar. The absolute value of the elevator deflection angle is plotted in Fig. 3.31, excluding models 1 and 2 as above. The bending frequency shows the same trend as in the thrust integral, with the more flexible models needing less elevator deflection. The in-plane bending frequency, as well as the short period-to-in-plane and phugoid-to-in-plane frequency ratios, also shows to be an important contributor. The larger the in-plane bending stiffness, the larger the elevator deflection.

To get a measure of the total control energy used, the sum of the elevator deflection and thrust integrals was plotted, with the results shown in Fig. 3.32. The data show that as the models become stiffer in all three directions, bending, torsion, and in-plane bending, the total control integral increases. Comparing this to the control effort plotted in Fig. 3.26, one sees similar trends for in-plane bending, but the opposite trend in the bending frequency plots, although the data in Fig. 3.26 are somewhat scattered.

The maximum overshoot is plotted in Fig. 3.33. The data are scattered, but once again are a function of various in-plane bending frequency ratios. The maximum overshoot increases as the bending-to-in-plane, short period-to-in-plane, and phugoid-to-in-plane bending frequencies increases. The data for settling time were also plotted, but no trends were evident.

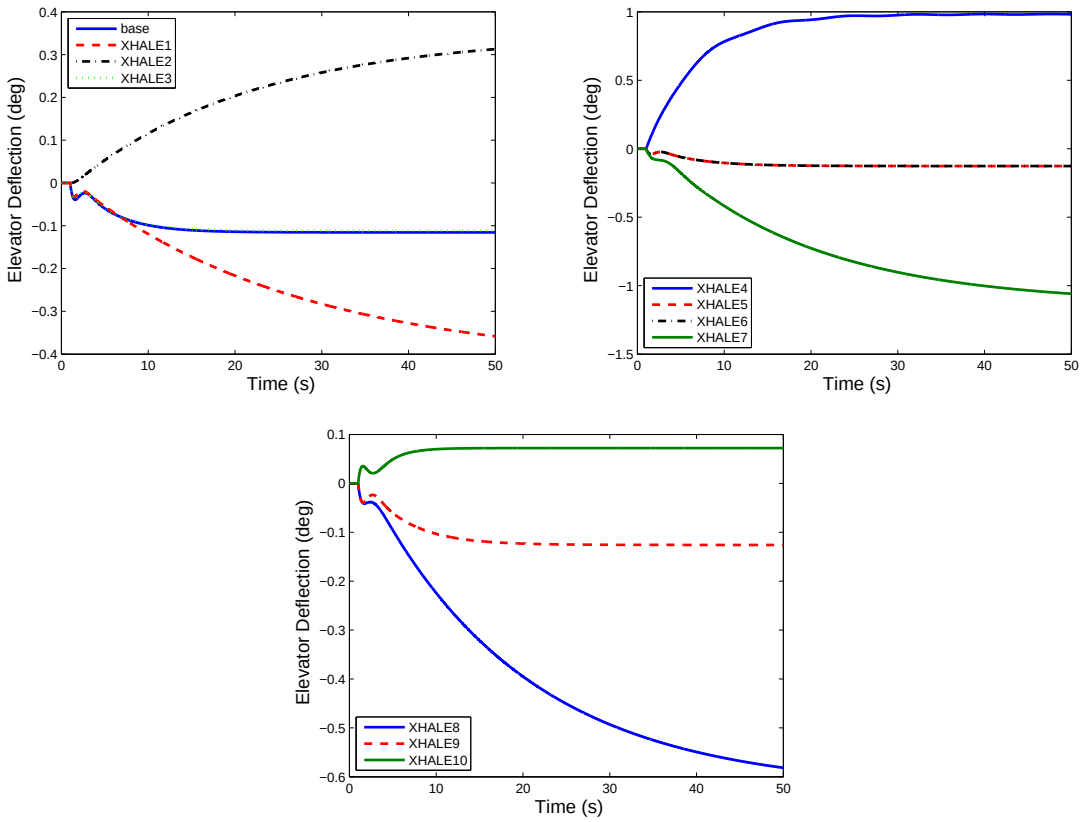

Figure 3.30: X-HALE linear models' elevator deflection about trim state during pitch angle tracking.

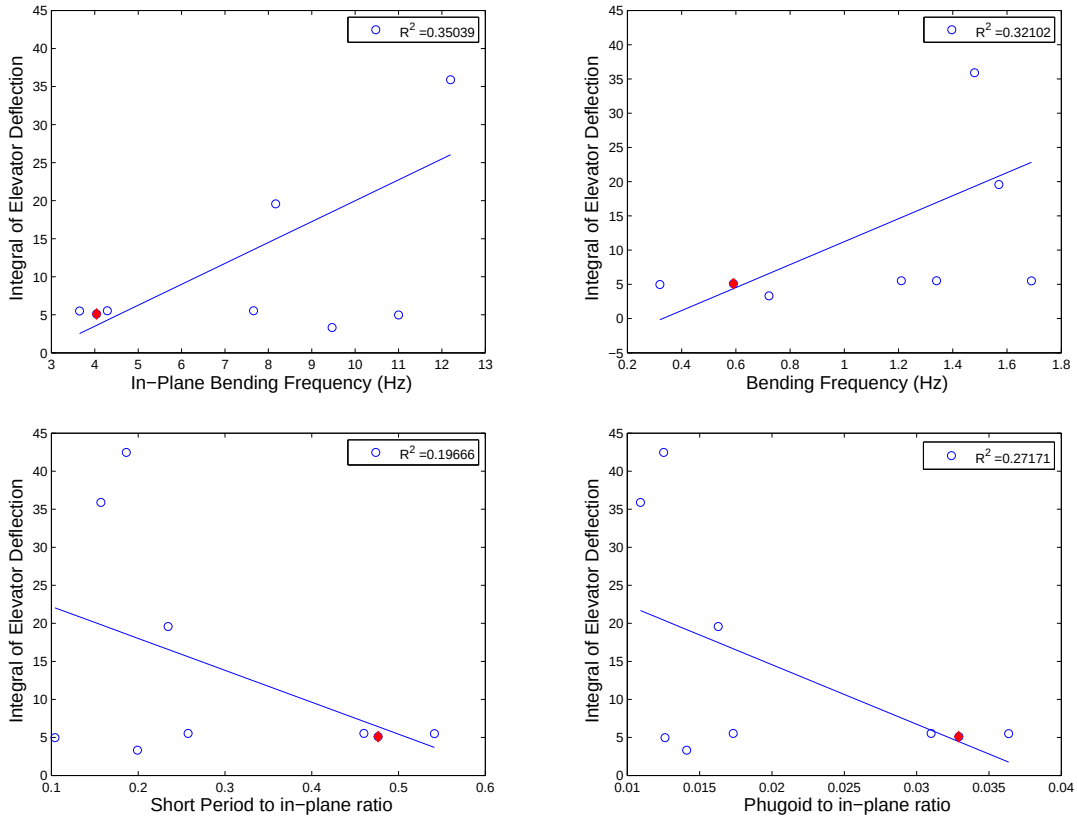

Figure 3.31: Integral of X-HALE elevator deflection during pitch angle tracking (red diamond shows baseline case).

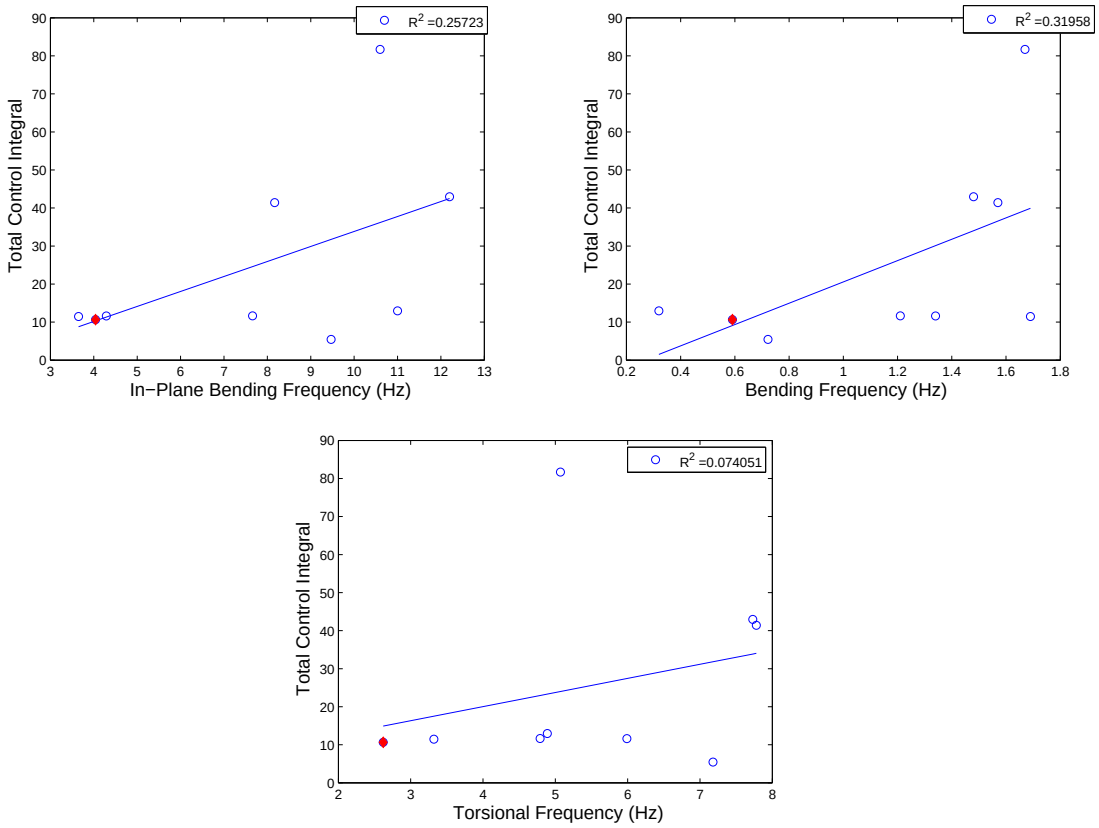

Figure 3.32: X-HALE linear models' total control integral about trim state during pitch angle tracking (red diamond shows baseline case).

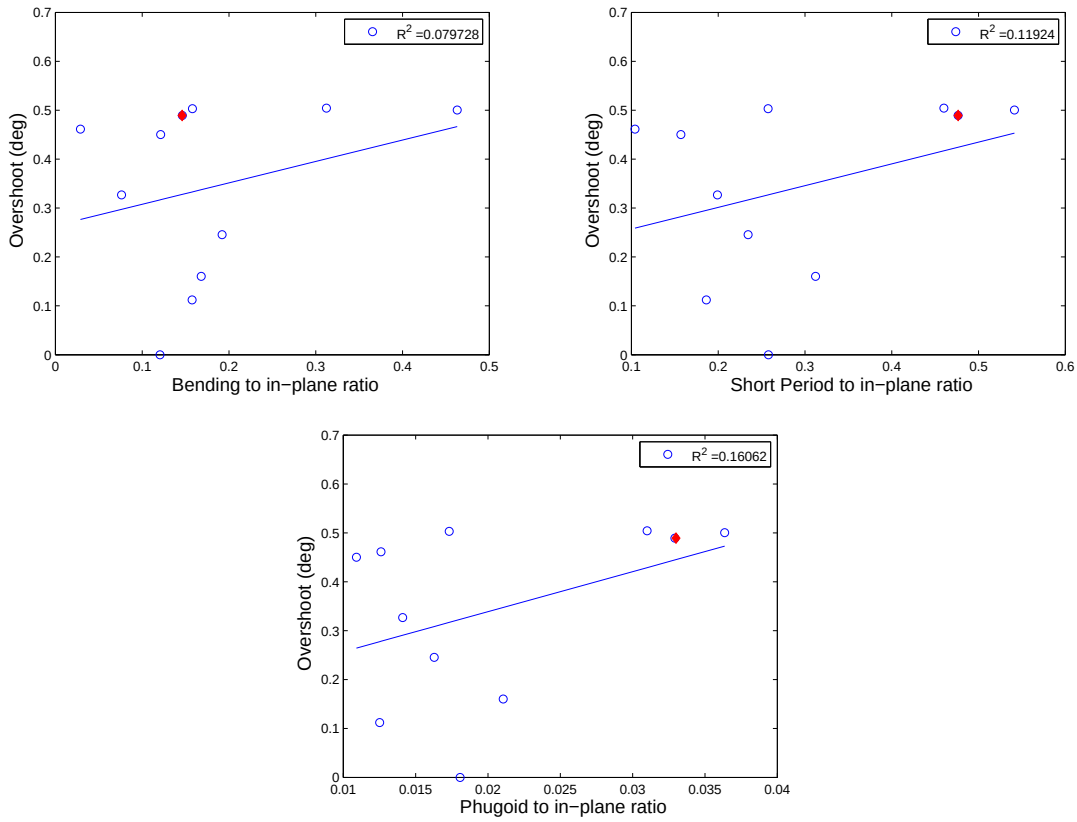

Figure 3.33: X-HALE maximum overshoot to 10° pitch step command (red diamond shows baseline case).

3.3.3 Gust Response Sensitivity Concluding Remarks

The sensitivity of open and closed loop response to changes in stiffness parameters was studied for both the flying wing model and X-HALE model. For the flying wing, it was shown that during an open loop gust encounter one could not simultaneously minimize both root curvature and pitch angle by adjusting aircraft parameters, while this could be done on the X-HALE. In general, the flying wing results showed that stiffer aircraft has larger pitch angle excursion in gust, while the opposite was seen in the X-HALE model simulations. An increase in in-plane stiffness from the X-HALE model with the largest pitch angle resulted in little change. Additionally, the torsional stiffness was found to be an important parameter in pitch angle response for the X-HALE model. The baseline aircraft's maximum pitch angle was reduced by 26% and its maximum root curvature was reduced by 31% when the torsional stiffness was increased. Similar trends were seen in the two aircraft when examining the maximum root curvature, with the lowest bending stiffness models having the largest root curvature values. The output control effort metric of both aircraft showed that the more flexible in bending the models were, the larger the output control effort that was required. The in-plane bending stiffness also played a large role in the output control effort for the X-HALE.

While the frequency separation between the elastic and flight dynamic modes was not addressed directly, the phugoid to bending frequency ratio gives a feel for the amount of separation. Most of the time, a lower phugoid to bending frequency ratio, indicating a larger frequency separation, resulted in better aircraft performance for both aircraft. The maximum root curvature and control effort metrics were lower for the models with a larger frequency separation. The only exception to this was the flying wing models with a lower phugoid to bending ratio that had a higher maximum pitch angle.

The open and closed loop response of the aircraft models showed that it was a function of all three stiffness parameters. Additionally, the trends found were dependent on aircraft configuration and currently no generalization can be made.

CHAPTER 4

Trajectory Control in Gust

This chapter presents control strategies to track longitudinal and lateral trajectory commands in the presence of gust disturbances. A method for longitudinal control based on a method developed by Shearer and Cesnik in [16] is modified and demonstrated in nonlinear simulations on the X-HALE aircraft model in still air and then with various gust disturbances. A novel technique for lateral control is introduced and demonstrated in both still air and with gust disturbances. Finally, the capability to track simultaneously the longitudinal and lateral commands in the presence of gust disturbances is demonstrated. The following assumptions are made in [16] and are continued here:

1) The angle of sideslip is zero;

2) The Euler roll angle ϕ is used in place of the bank angle μ;

3) Total velocity V_t is prescribed and constant;

4) The angle of attack, α, is proportional to $\cos\phi$.

4.1 Longitudinal Control

The control architecture used for the longitudinal control is a two-loop scheme based on a method developed by Shearer and Cesnik [16], with a block diagram shown in Fig. 4.1. The outer loop is designed to mimic the actions of a human pilot. A stable inner loop is used to track body velocities, denoted by β and is augmented with appropriate error and

integral states. The inner loop controller was tuned first, and after acceptable β tracking was accomplished, the outer loop was tuned.

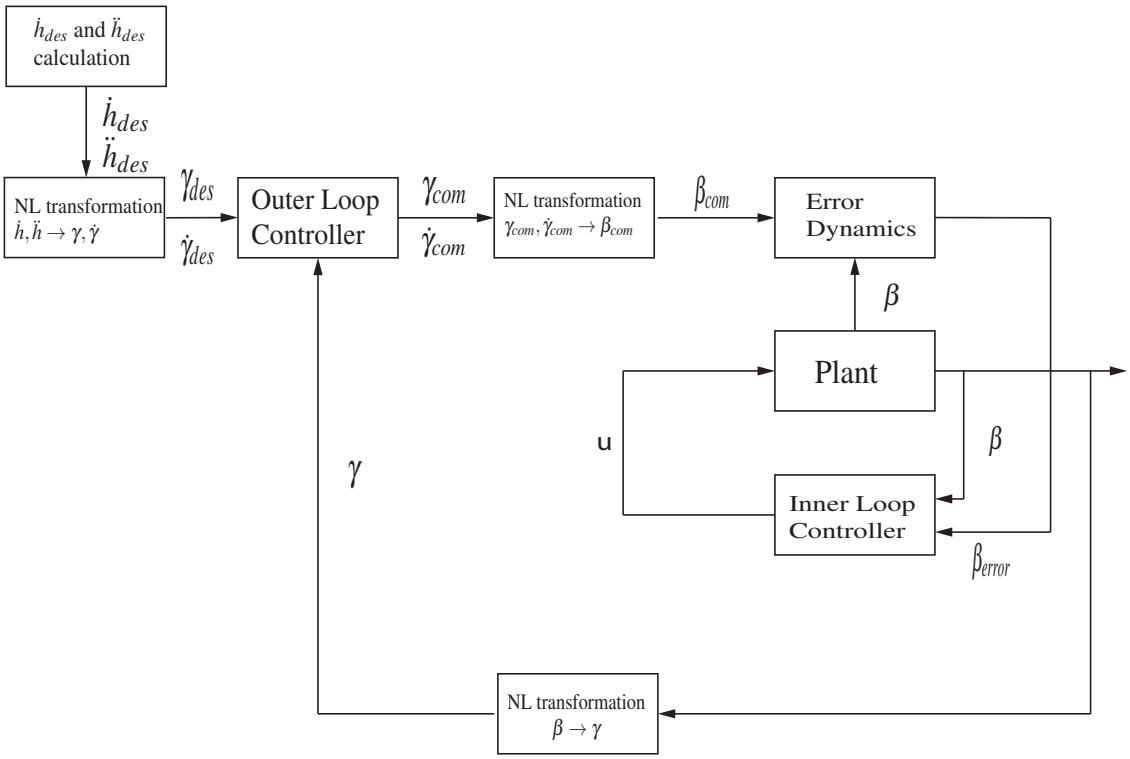

Figure 4.1: Longitudinal control architecture [16].

4.1.1 Longitudinal Inner Loop

The longitudinal inner loop controller is based on a nonlinear dynamic inversion (DI) control scheme developed in [16]. Dynamic Inversion is a control technique that uses nonlinear transformations and feedback control to convert a nonlinear system model to a linear system model, to which linear control techniques can be applied [49]. Consider a nonlinear system model in control affine form,

$$\dot{x} = f(x) + g(x)u, \tag{4.1}$$

$$y = h(x), \tag{4.2}$$

where x is the state vector, u is the control vector, and y is the output vector. It is assumed that y and u have the same dimension. The derivative of the output vector, $\dot{y}$, is given by

$$\dot{y} = \frac{\partial h}{\partial x} f(x) + \frac{\partial h}{\partial x} g(x) u. \tag{4.3}$$

If the matrix $\left[\frac{\partial h}{\partial x} g(x)\right]^{-1}$ is invertible, the control input u is

$$u = \left[\frac{\partial h}{\partial x} g(x)\right]^{-1} \left(v - \frac{\partial h}{\partial x} f(x)\right), \tag{4.4}$$

leading to $\dot{y} = v$. The pseudo-input, v, can be calculated using

$$v = -Ky, \tag{4.5}$$

where K is a gain matrix, which can be determined using linear control techniques.

To derive the DI controller for use on the X-HALE model, consider the EOM, Eqs. 2.34 - 2.35, re-written in matrix form,

$$\begin{bmatrix} M_{FF} & M_{FB} \\ M_{BF} & M_{BB} \end{bmatrix} \begin{bmatrix} \ddot{\varepsilon} \\ \dot{\beta} \end{bmatrix} = - \begin{bmatrix} C_{FF} & C_{FB} \\ C_{BF} & C_{BB} \end{bmatrix} \begin{bmatrix} \dot{\varepsilon} \\ \beta \end{bmatrix} - \begin{bmatrix} K_{FF}\varepsilon \\ 0 \end{bmatrix} + \begin{bmatrix} R_F \\ R_B \end{bmatrix}. \tag{4.6}$$

Using Eq. 4.6, it follows that $\ddot{\varepsilon}$ and $\dot{\beta}$ are

$$\ddot{\varepsilon} = -C_{11}\dot{\varepsilon} - C_{12}\beta - Q_M K_{FF}\varepsilon + R_{F1}, \tag{4.7}$$

$$\dot{\beta} = -C_{22}\beta - C_{21}\dot{\varepsilon} + R_{B1}, \tag{4.8}$$

where

$$Q_M = \left(M_{FF} - M_{FB}M_{BB}^{-1}M_{BF}\right)^{-1}, \tag{4.9}$$

$$C_{11} = Q_M C_{FF} - Q_M M_{FB} M_{BB}^{-1} C_{BF}, \tag{4.10}$$

$$C_{12} = Q_M C_{FB} - Q_M M_{FB} M_{BB}^{-1} C_{BB}, \tag{4.11}$$

$$C_{21} = -M_{BB}^{-1}M_{BF}Q_M C_{FF} + \left(M_{BB}^{-1}M_{BF}Q_M M_{FB}M_{BB}^{-1} + M_{BB}^{-1}\right) C_{BF}, \tag{4.12}$$

$$C_{21} = -M_{BB}^{-1}M_{BF}Q_M C_{FB} + \left(M_{BB}^{-1}M_{BF}Q_M M_{FB}M_{BB}^{-1} + M_{BB}^{-1}\right) C_{BB}, \tag{4.13}$$

$$R_{F1} = Q_M R_F - Q_M M_{FB} M_{BB}^{-1} R_B, \tag{4.14}$$

$$R_{B1} = -M_{BB}^{-1}M_{BF}Q_M R_F + \left(M_{BB}^{-1}M_{BF}Q_M M_{FB}M_{BB}^{-1} + M_{BB}^{-1}\right) R_B. \tag{4.15}$$

Then the generalized force vectors R_{F1} and R_{B1} can be re-written in control affine form leading to a new form for Eq. 4.8

$$\dot{\beta} = f_\beta + g_\beta u_{long}, \tag{4.16}$$

where u_{long} is the longitudinal control vector. The control inputs used in this study for longitudinal control are the elevators, which are constrained to move together, and the thrust on the center three motors, which are also constrained to move together. Thus the vector, u_{long} is two dimensional. The dynamic inversion controller can now be derived based on Eq. 4.16. The output vector, y_{long}, for this control setup are the forward velocity, v_{By}, and the pitch rate, ω_{Bx}. The output vector, y_{long}, can be formed in terms of the body velocity vector, β, as

$$y_{long} = C_{long}\beta, \tag{4.17}$$

where

$$C_{long} = \begin{bmatrix} 0 & 1 & 0 & 0 & 0 & 0 \\ 0 & 0 & 0 & 1 & 0 & 0 \end{bmatrix}. \tag{4.18}$$

The control vector is prescribed in terms of the pseudo-control v_{long} as

$$u_{long} = g_{\beta}^{-1} \left(v_{long} - f_{\beta} \right), \tag{4.19}$$

leading to $\dot{y} = v_{long}$. The pseudo-control v_{long} is found by applying LQR techniques to the linear system model augmented with the integral states

$$\begin{bmatrix} \dot{y} \\ \dot{z}_{long} \end{bmatrix} = \begin{bmatrix} 0 & 0 \\ C_{long} & 0 \end{bmatrix} \begin{bmatrix} \beta \\ z_{long} \end{bmatrix} + \begin{bmatrix} I \\ 0 \end{bmatrix} v_{long} - \begin{bmatrix} 0 \\ I \end{bmatrix} \begin{bmatrix} v_{By,com} \\ \omega_{Bx,com} \end{bmatrix}, \tag{4.20}$$

where $v_{By,com}$ and $\omega_{Bx,com}$ denote, respectively, the commanded forward velocity and the commanded pitch rate, while z_{long} denotes the integral state vector. Additionally, it should be noted that f_{β} and g_{β} in Eq. 4.19 are calculated at every time step based on the current aircraft states.

Although only the rigid body dynamics are being inverted, the aircraft is not assumed to be rigid and the flexibility effects are still included. Examining Eq. 4.8, one sees that the current value of $\dot{\varepsilon}$ is included in the dynamics. Additionally, the matrices C_{21}, C_{22}, and R_{B1} are updated at every time step with C_{21} and C_{22} being dependent on ε and $\dot{\varepsilon}$ and R_{B1} is a function of ε, $\dot{\varepsilon}$ and $\ddot{\varepsilon}$.

Thus the above design assumes the knowledge of current elastic state values. These states could be measured using strain gauges and/or cameras. Approaches to perform dynamic inversion using assumed trim or zero values of elastic states have also been tried but have not led to successful designs.

4.1.2 Longitudinal Outer Loop

The outer loop is designed to act similarly to a human pilot and consists of nonlinear transformations and an outer loop controller. Referring to Fig. 4.1, suppose the outer loop is given an altitude change command. The aircraft is then commanded to climb at a constant

climb rate, $\dot{h}$, until 90% of the climb has been completed, and the desired flight path angle, γ, necessary to achieve this $\dot{h}$ is calculated. After 90% of the climb has been completed, the controller switches to computing the $\dot{\gamma}$ and γ required to reduce the altitude error to zero in a given amount of time. These desired values of $\dot{\gamma}_{des}$ and γ_{des}, as well as the current values,$\dot{\gamma}$ and γ, are then passed through an outer loop controller, which calculates the commanded values of $\dot{\gamma}$ and γ, denoted by γ_{com} and $\dot{\gamma}_{com}$ in Fig. 4.1. These commanded values are then passed though a nonlinear transformation which converts them to commanded β values, β_{com}, that are then passed to the inner loop controller.

The nonlinear transformation converts the flight path angle γ and roll angle ϕ as well as their time derivatives $\dot{\gamma}$ and $\dot{\phi}$ to body velocities. It begins by calculating the current angle of attack, α as well as $\dot{\alpha}$ [16]:

$$\alpha = \frac{1}{\cos\phi}\alpha_0, \tag{4.21}$$

$$\dot{\alpha} = \tan\phi \ \sec\phi\alpha_0\dot{\phi}, \tag{4.22}$$

where α_0 is the trimmed, wings-level angle of attack. Next the body translational velocities, with the assumption of $v_x = 0$, are found using [16]

$$v_z = -V_t \sin\alpha, \tag{4.23}$$

$$v_y = \sqrt{V_t^2 - v_z^2}, \tag{4.24}$$

where $V_t = \sqrt{v_x^2 + v_y^2 + v_z^2}$ is the total aircraft velocity. Next, the Euler pitch angle and its time derivative are calculated based on the following relationships [16]

$$\sin\gamma = \cos\alpha\sin\theta - \cos\phi\sin\alpha\cos\theta, \tag{4.25}$$

$$\dot{\theta} = \frac{\cos\gamma\dot{\gamma} + \left(\sin\alpha\sin\theta + \cos\phi\cos\alpha\cos\theta\right)\dot{\alpha}}{\cos\alpha\cos\theta + \cos\phi\sin\alpha\sin\theta} - \frac{\sin\phi\sin\alpha\cos\theta\dot{\phi}}{\cos\alpha\cos\theta + \cos\phi\sin\alpha\sin\theta}. \tag{4.26}$$

Then the body angular velocities are found by simultaneously solving the following system of equations [16] for ω_x, ω_y, and ω_z

$$\dot{\phi} = (\tan\theta \sin\phi)\,\omega_x + \omega_y - (\tan\theta \cos\phi)\,\omega_z, \tag{4.27}$$

$$g \sin\phi \cos\phi = v_z \omega_y - v_y \omega_z, \tag{4.28}$$

$$\dot{\theta} = \cos\phi \omega_x + \sin\phi \omega_z, \tag{4.29}$$

where g is the magnitude of the gravity vector.

The current values of γ and $\dot{\gamma}$, as well as the desired values, γ_{des} and $\dot{\gamma}_{des}$, are then passed to an outer loop controller. In [16], the following outer loop control structure is employed

$$\gamma_{com} = K_\gamma \Delta\gamma + K_{I\gamma} \int_0^t \Delta\gamma d\tau + K_{II\gamma} \int_0^t \left(\int_0^\tau \Delta\gamma ds \right) d\tau + K_{d\gamma} \Delta\dot{\gamma}, \tag{4.30}$$

$$\dot{\gamma}_{com} = K_{\dot{\gamma}} \Delta\dot{\gamma} + K_{I\dot{\gamma}} \Delta\gamma + K_{II\dot{\gamma}} \int_0^t \Delta\gamma d\tau + K_{III\dot{\gamma}} \int_0^t \left(\int_0^\tau \Delta\gamma ds \right) d\tau, \tag{4.31}$$

where $\Delta\gamma = \gamma - \gamma_{des}$ and $\Delta\dot{\gamma} = \dot{\gamma} - \dot{\gamma}_{des}$. We refer to Eqs. 4.30 and 4.31 as a (non-standard) PID controller. The other control approach used in this study for the outer loop controller is augmented with a sliding mode controller. This controller is derived based on the assumed model

$$\ddot{\gamma} = u, \tag{4.32}$$

where u is $\dot{\gamma}_{com}$ in Fig. 4.1 and γ_{com} is set to γ_{des}. We rely on the sliding mode control robustness to compensate for unmodeled dynamics.

The goal of sliding mode control is to force the trajectories of a system to a user-defined

sliding surface. The sliding surface is defined by $S = 0$, where

$$S = \lambda\left(\gamma - \gamma_{des}\right) + \left(\dot{\gamma} - \dot{\gamma}_{des}\right). \tag{4.33}$$

Choose a candidate Lyapunov function of the form

$$V(x) = \frac{1}{2}S^2, \tag{4.34}$$

then from Eqs. 4.32 - 4.34 it follows that

$$\dot{V}(x) = S\dot{S} \tag{4.35}$$

$$= S\left[\lambda\left(\dot{\gamma} - \frac{d}{dt}\gamma_{des}\right) + \left(\ddot{\gamma} - \frac{d}{dt}\dot{\gamma}_{des}\right)\right] \quad = S\left[\lambda\left(\dot{\gamma} - \frac{d}{dt}\gamma_{des}\right) + u - \frac{d}{dt}\dot{\gamma}_{des}\right]. \tag{4.36}$$

Selecting

$$u = -\left[\lambda\left(\dot{\gamma} - \frac{d}{dt}\gamma_{des}\right) - \frac{d}{dt}\dot{\gamma}_{des}\right] - Ksign(S), \tag{4.37}$$

with $K > 0$ ensures that $\dot{V} = -K|S| < 0$ and that S converges to zero in finite time. Therefore $\gamma(t) \to \gamma_{des}(t)$ and $\dot{\gamma}(t) \to \dot{\gamma}_{des}(t)$ as $t \to \infty$.

One problem with implementing a sliding mode controller is that it is discontinuous and the closed loop system is prone to chattering [50]. To address this, a boundary layer of width Φ is created around $S = 0$ so that u is given by [50]

$$u = -\left[\lambda\left(\dot{\gamma} - \frac{d}{dt}\gamma_{des}\right) - \frac{d}{dt}\dot{\gamma}_{des}\right] - Ksat\left(\frac{S}{\Phi}\right), \tag{4.38}$$

where $sat(\cdot)$ is the saturation function.

4.1.3 Longitudinal Control Numerical Studies

The first step in implementing the longitudinal control architecture described above was to tune the inner loop controller. The tuning parameters available were gains on the two control signals, elevators and thrust, gains on the two integrator states, forward velocity and pitch rate, and v_{long} in Eq. 4.20, which could be modified by adjusting the LQR parameters. The inner loop tracking performance was determined by giving the inner loop a velocity step command and a $1 - \cos$ pitch rate command, with the results shown in Fig. 4.2. The velocity command is tracked well, and the pitch rate command is also tracked well after the transient response caused by the change in speed.

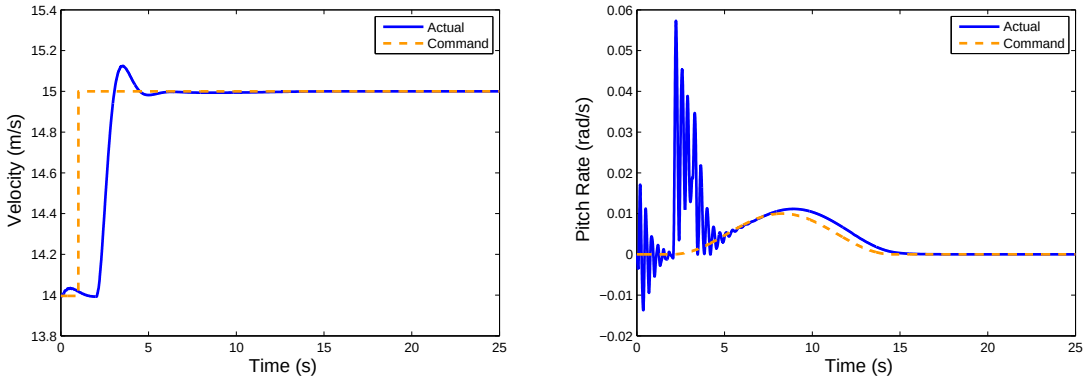

Figure 4.2: Inner loop tracking.

The aircraft was given a climb command, in still air, of 20 m, which is 100 chord lengths, with a desired climb rate of 0.432 m/s. This is the climb rate the Helios aircraft had on its mishap flight [2]. The response with the original PID outer loop controller from [16] is shown in Fig. 4.3. The aircraft follows the climb command well, but begins to diverge when it attempts to level off. Examining the inner loop plots, one can see that the aircraft is tracking the velocity and pitch rate commands well, even while the motion is diverging. Additionally, γ and γ_{com} seem to be out of phase. This provided an indication that the outer loop was causing this issue.

Two approaches were pursued to increase the robustness of the outer loop controller, and provide a stable tracking response. The first approach was to increase the PID gains

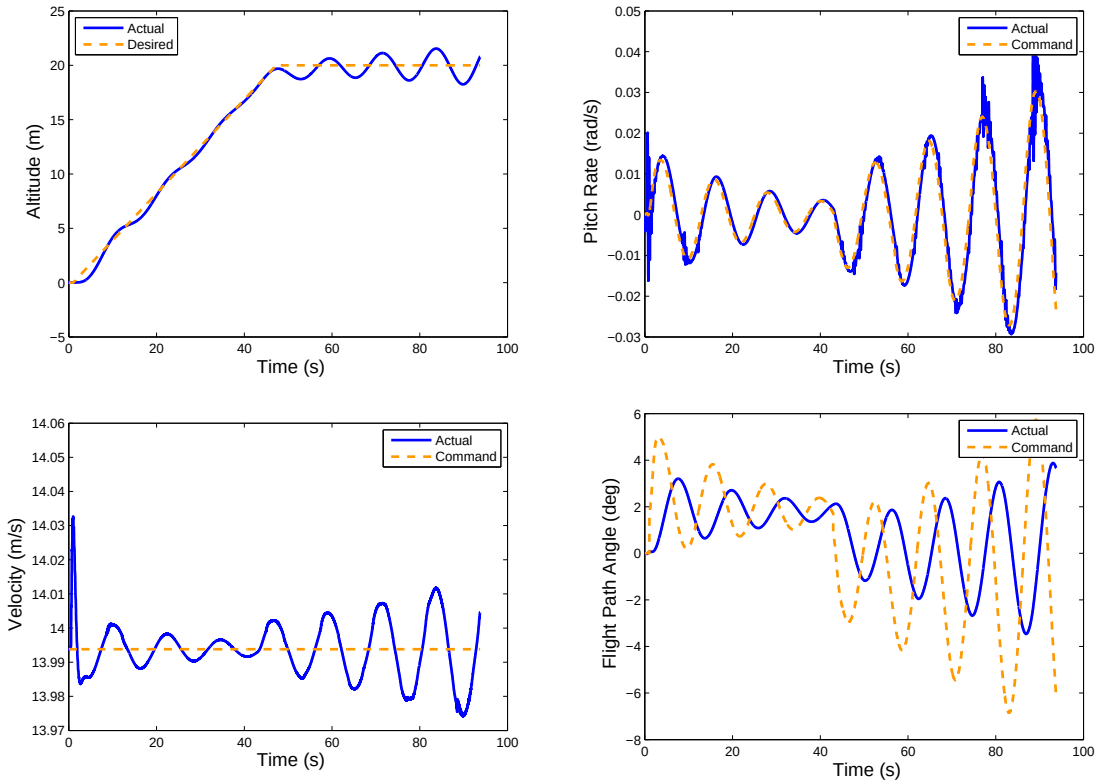

Figure 4.3: Response to altitude change command with original PID outer loop controller.

after the aircraft had completed 90% of the climb and was about to level off. We refer to this approach as the Higher Gain PID controller. The second approach was to design a sliding mode controller for the leveling-off phase after 90% of the climb. The aircraft response with the various outer loop controllers is shown in Fig. 4.4. The higher gain PID and sliding mode controllers both track the altitude command well in the level off phase. The sliding mode controller has larger control inputs and induces a larger velocity deviation, but at only approximately 0.2 m/s it is still acceptable. From examining the responses, one could deduce that the higher gain PID controller would be preferable to the sliding mode controller, but the higher gain PID controller does not have the stability margins that the sliding mode controller possesses. Therefore, for slightly different aircraft configurations and/or gust profiles, the higher gain PID controller may be unstable. This means that the sliding mode outer loop controller could be preferable.

The aircraft was then given the same 20-m altitude climb command in the presence of

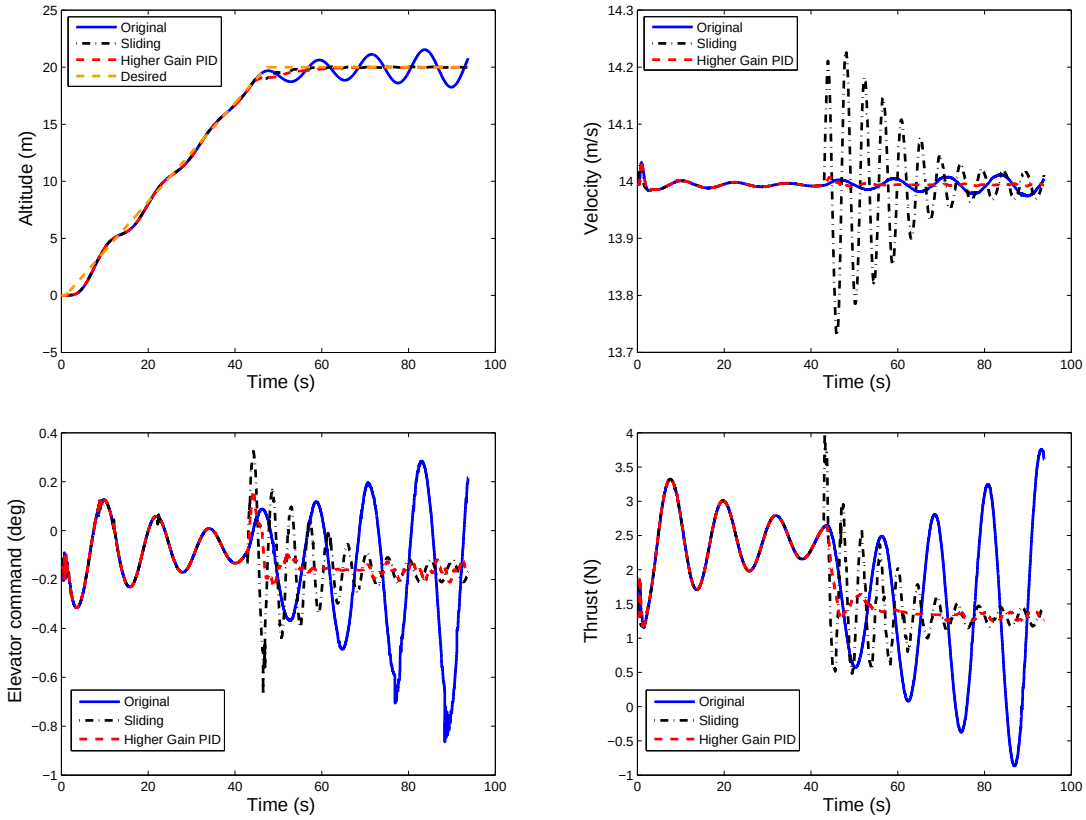

Figure 4.4: Comparison of outer loop controllers.

a 2-s duration, repeating gust disturbance. Originally, the control input was calculated at 10 Hz, but the performance was significantly worse than the simulations in still air. The control update rate was then doubled to 20 Hz. A comparison between the responses for the same controller updated at 10 and 20 Hz is shown in Fig. 4.5. The 20-Hz controller is able to track the altitude command better. The control signals are significantly smaller with a 20 Hz control time, and the speed and altitude response is better, with smaller deviations.

Next, gust disturbances of 2-s, 4-s, and 8-s as well as a Dryden gust profile were added to the 20-m climb command simulation. The altitude tracking performance for both the sliding mode and higher gain PID outer loop controllers is shown in Fig. 4.6. The performance with both outer loop controllers is similar, with both controllers tracking the altitude commands well in all the gust conditions.

The root curvature on the right side of the wing during altitude tracking in the presence of gust disturbances is shown in Fig. 4.7. The curvature is an important measure because it is proportional to bending moment. The sliding mode controller has a much lower root curvature with the 2-s gust, but a higher root curvature with the other three gusts simulated, when compared to the higher gain PID controller.

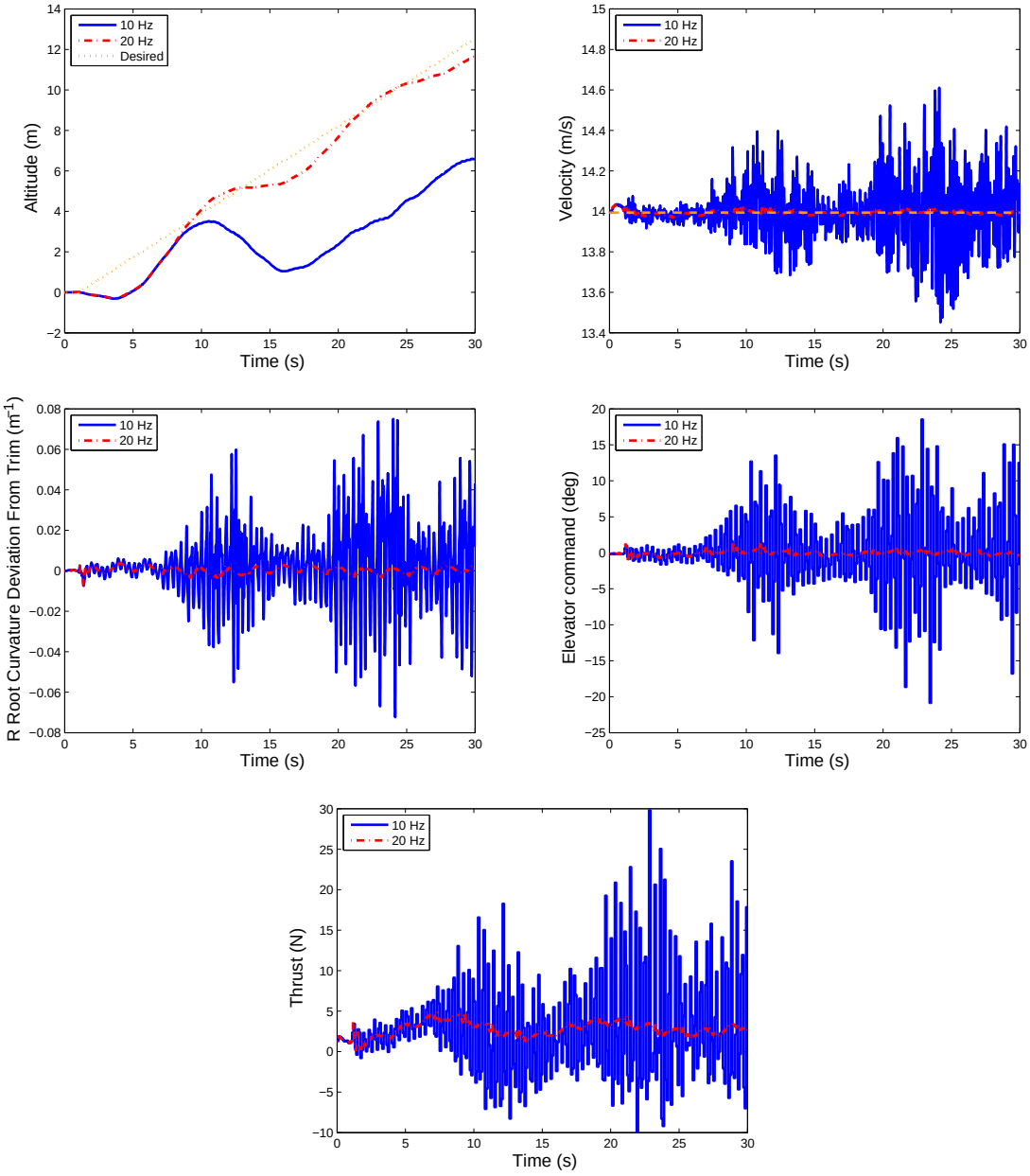

Figure 4.5: Altitude tracking performance for two different control update rates in the presence of wind gusts.

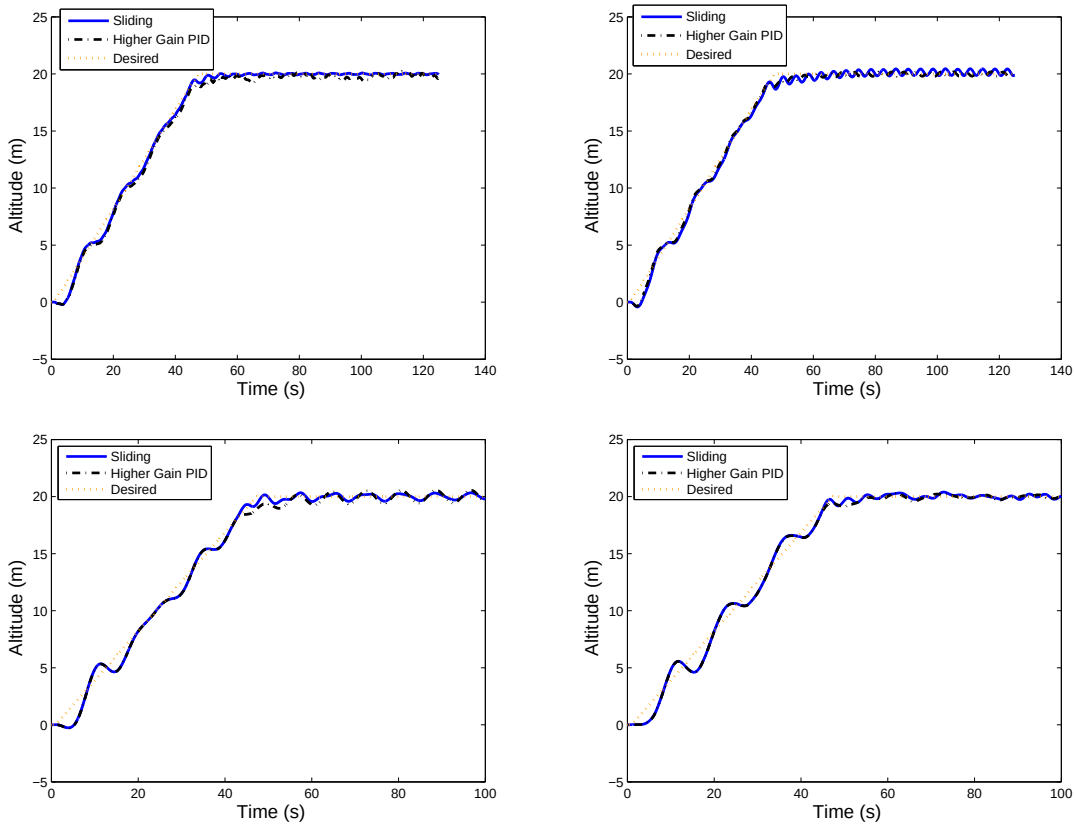

Figure 4.6: Altitude tracking response with 2-s (top left), 4-s (top right), 8-s (bottom left) and Dryden gust (bottom right).

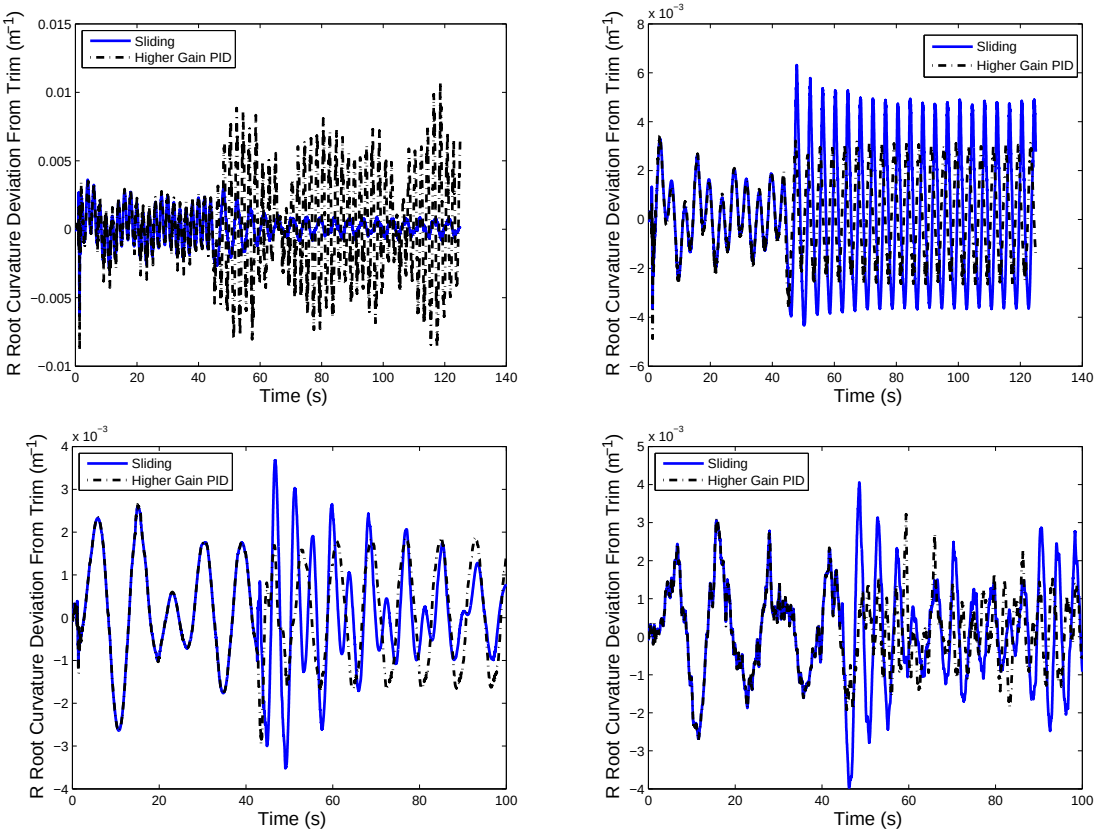

Figure 4.7: Root curvature response on the right wing during altitude tracking response with 2-s (top left), 4-s (top right), 8-s (bottom left) and Dryden gust (bottom right).

4.2 Lateral Control

Dynamic inversion was not attempted for the lateral controller for a couple of reasons. First, the lateral modes are more coupled with the elastic modes, meaning the entire system dynamics would need to be inverted, which would be difficult due to the large dimensionality. Also, dynamic inversion works best for "square" systems where the number of tracked set-points is equal to the number of controls, eliminating the need to use pseudo-inverses.

The lateral controller was designed using a reduced order linear model of the aircraft. The reduced order linear model was obtained using the balanced truncation approach [48]. Balanced truncation allows one to reduce the order of a linear system while retaining the system's input-output properties. Given a system model in the form

$$\dot{x} = Ax + Bu, \tag{4.39}$$

$$y = Cx + Du, \tag{4.40}$$

where x is the state vector and u is the control vector. The controllability and observability gramians, P and Q, respectively, are given by:

$$P = \int_0^\infty e^{A\tau} B B^T e^{A^T \tau} d\tau, \tag{4.41}$$

$$Q = \int_0^\infty e^{A^T \tau} C^T C e^{A\tau} d\tau. \tag{4.42}$$

The gramians are solutions to the following Lyapunov equations [48],

$$AP + PA^T + BB^T = 0, \tag{4.43}$$

$$A^T Q + QA + C^T C = 0. \tag{4.44}$$

A balanced realization of the system is an asymptotically stable, minimal realization for which the gramians are equal, i.e., $P = Q$. The Hankel singular values, σ_i, of the system

are defined as [48]

$$\sigma_i = \sqrt{\lambda_i(PQ)}, \tag{4.45}$$

where λ_i denotes the eigenvalues of the system. The Hankel singular values provide a measure of the relative contributions of each state to the input-output behavior of the entire system. The balanced truncation method simply removes the states with the lowest Hankel singular values, leaving a lower order system with similar input-output behavior to the original system.

The reduced order linear model of the aircraft is then used to create an LQG controller. A Linear Quadratic Gaussian (LQG) controller combines a Linear Quadratic Regulator (LQR) controller that assumes full state measurement with a Kalman filter, used for state estimation. The LQG design problem, applied to Eqs. 4.39 and 4.40, is to find the control matrix, K, that minimizes the cost function:

$$J = \lim_{T\to\infty} \frac{1}{T} E\left\{ \int_0^T (x^T Q x + u^T R u) dt \right\}, \tag{4.46}$$

with the control input u given by [51]

$$u = -K\hat{x}, \tag{4.47}$$

The state estimate, $\hat{x}$, determined by the Kalman filter,i.e.,

$$\dot{\hat{x}} = A\hat{x} + Bu + L\left(y - C\hat{x}\right), \tag{4.48}$$

where L is the optimal observer gain calculated using

$$L = \Sigma C^T R^{-1}, \tag{4.49}$$

Σ is the positive semi-definite solution of the algebraic Riccatti Equation,[48]:

$$A\Sigma + \Sigma A^T + Q_o - \Sigma C^T R_o^{-1} C\Sigma = 0, \tag{4.50}$$

and Q_o and R_o are the intensity matrices of the process and sensor noise.

The LQR methodology provides a systematic way to choose a state feedback gain matrix K in Eq. 4.47 by minimizing the cost function:

$$J = \int_0^\infty (x^T Q x + u^T R u) dt, \tag{4.51}$$

where Q is a positive semi-definite state weighting matrix and R is a positive definite control weighting matrix. A matrix P is found by solving the algebraic Riccati Equation,

$$PA + A^T P + Q - PBR^{-1}B^T P = 0. \tag{4.52}$$

Then the optimal gain matrix is found using

$$K = R^{-1}B^T P. \tag{4.53}$$

A lateral LQG is designed using the reduced order linear model of the aircraft. The output vector, y, is given by

$$y = \begin{bmatrix} \kappa_{y,rroot} & \kappa_{y,lroot} & v_x & \omega_y & \omega_z & \psi & \phi & \kappa_{y,rmid} & \kappa_{y,lmid} \end{bmatrix}^T. \tag{4.54}$$

where κ_y is the wing curvature, r and l denote right and left, respectively, $root$ and mid are measured at the root and mid-span of the wing, ψ and ϕ are the Euler yaw and roll angles. The choice to use four wing curvature values along the wing was made in order to allow the controller to get accurate information of the entire wing shape, which will not be symmetric during roll maneuvers while keeping the dimension of y small. Integrators were

also added on roll and yaw angles to improve tracking performance and ensure zero steady state error. The four control inputs are the left and right ailerons, and the left and right outboard motors, with all four able to move independently. One advantage of this approach over the lateral controller used in [16], where an LQR assuming full elastic state feedback was used, is that this approach only needs to measure κ_y in four locations along the wing, as opposed to measuring the entire ε vector all along the aircraft.

4.2.1 Lateral Control Numerical Studies

Here the aircraft is given a single period square wave roll angle command with a 5° amplitude. The yaw angle is commanded to stay at zero. One would normally calculate the desired yaw angle so that the sideslip angle remained at zero. In this formulation we do not have a direct output for sideslip angle, so we command yaw angle directly to verify the control architecture. A method for tracking the yaw angle needed to maintain zero sideslip will be added in the future. The response is shown if Fig. 4.8. The aircraft matches the roll commands well and has a maximum yaw angle of less than 1°. The root curvature values are much larger than those for the longitudinal tracking cases. The control inputs for this lateral tracking simulation are shown in Fig. 4.9. The thrust from the right and left motors are almost opposite of each other, while the right and left aileron deflections are in the same direction, with the right aileron having slightly less magnitude.

Next, the aircraft was given the same lateral commands in the presence of a 2-s repeating "1 - cos" gust, with the results shown in Fig. 4.10. The roll response is almost identical to the case with no gust. The yaw and root curvature response are also similar to the still air case, although the responses with the gust disturbance are more oscillatory. The lateral control inputs for the gust case are shown in Fig. 4.11. They show that the two ailerons are deflected similarly, but that the outboard motors act in opposite directions. The control inputs for the still air and gust simulations are shown in Fig. 4.12. All of the control inputs are similar, but with more oscillations in the gust simulation.

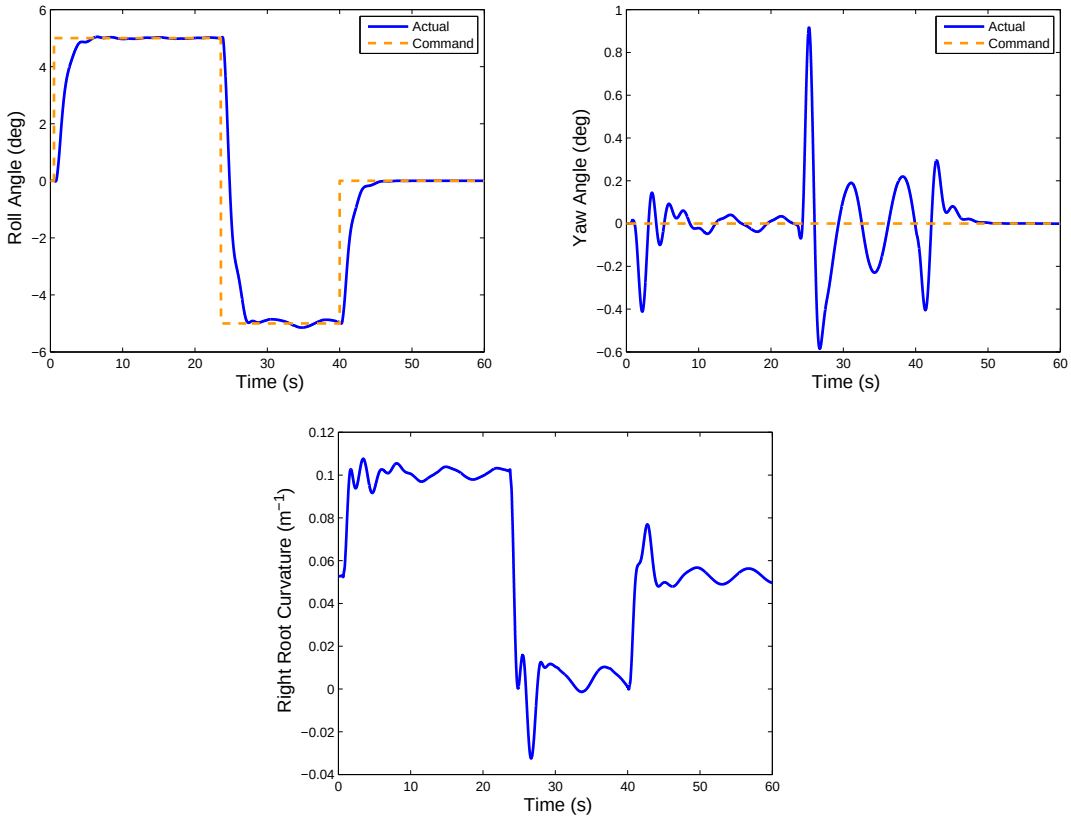

Figure 4.8: Lateral tracking response.

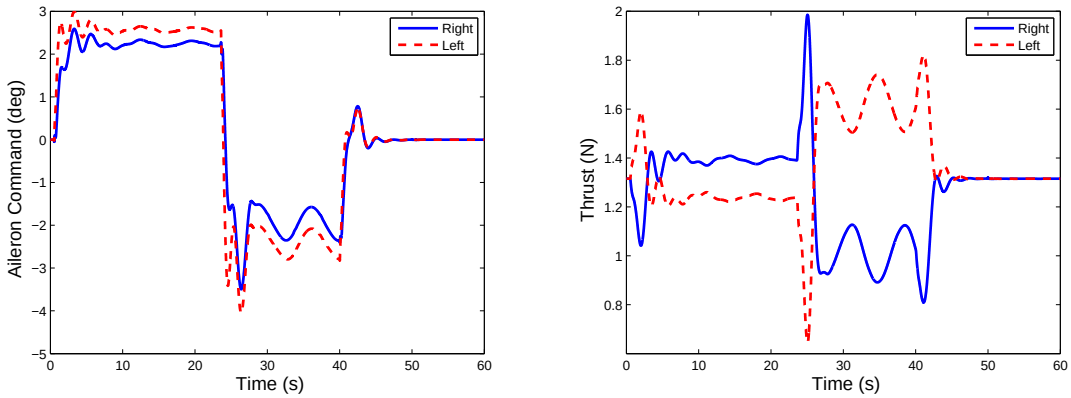

Figure 4.9: Lateral tracking control inputs.

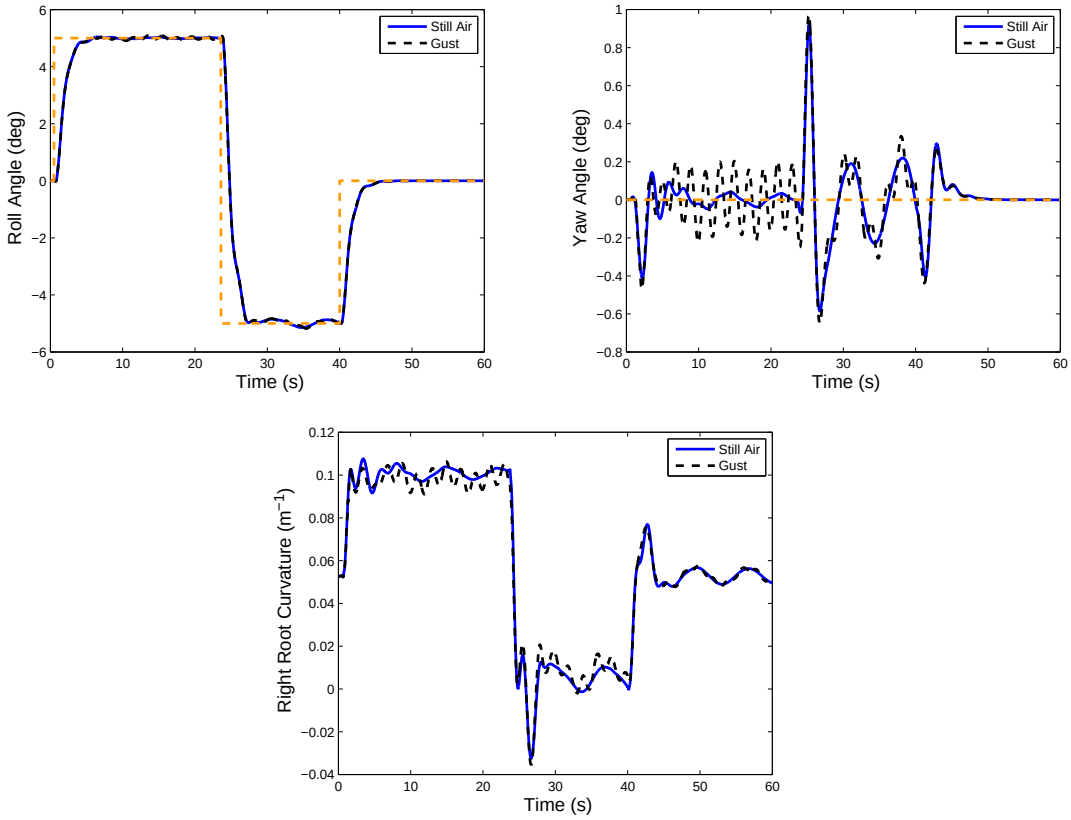

Figure 4.10: Lateral tracking response with 2-s duration, repeating gust disturbance.

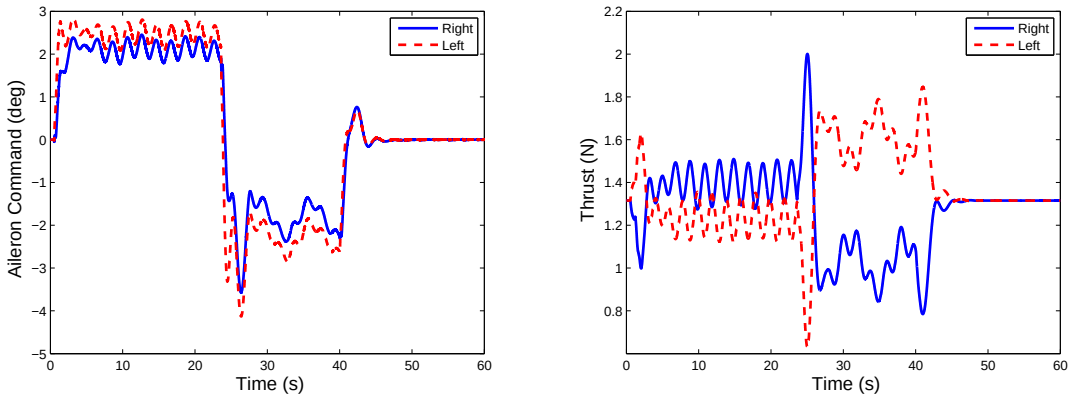

Figure 4.11: Lateral tracking control inputs with 2-s duration, repeating gust disturbance.

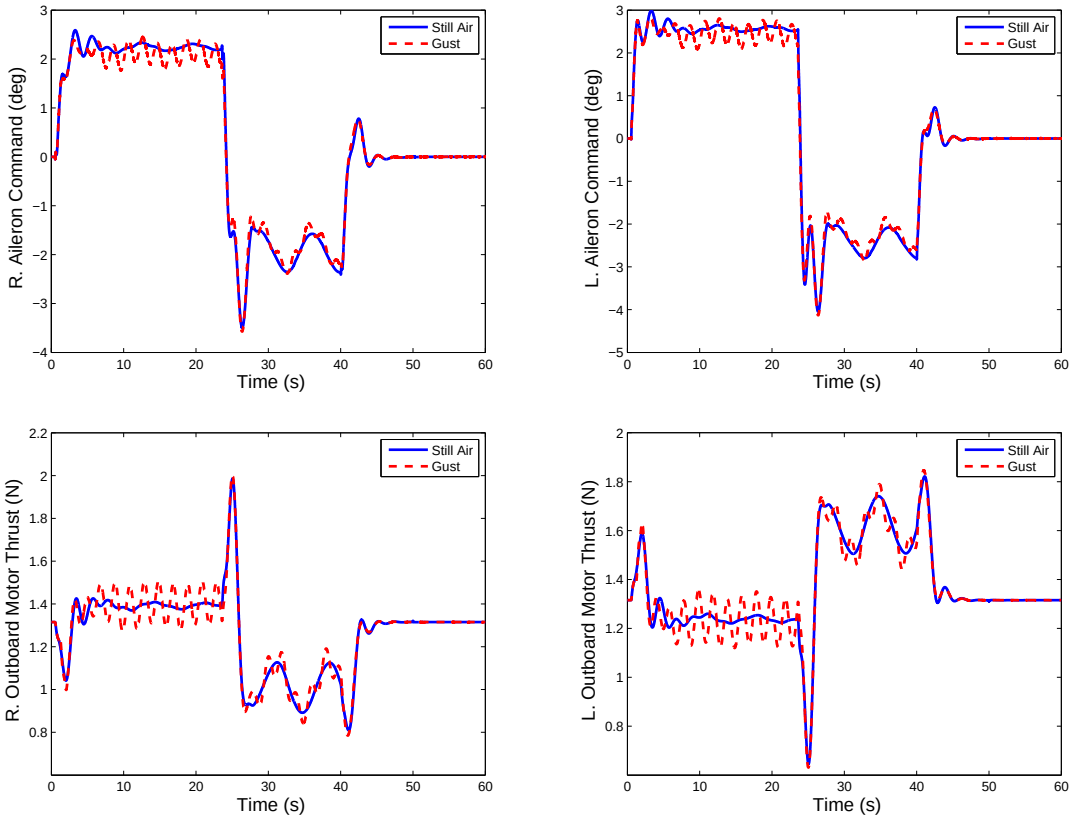

Figure 4.12: Comparison between lateral control inputs in still air and with 2-s gust.

4.3 Combined Control Numerical Studies

In order to demonstrate the ability to simultaneously track lateral and longitudinal commands, the aircraft was given the same longitudinal and lateral commands as in Sections 4.1.3 and 4.2.1. The results, with both the sliding and higher gain PID longitudinal outer loop controllers, are shown in Fig. 4.13. The aircraft tracks all the commands well. The altitude response is slightly worse than in the longitudinal only simulations, but is still acceptable. The roll and yaw tracking shows almost no degradation in performance from the lateral only tracking. The control signals are shown in Fig. 4.14 and are similar to those in the separate longitudinal and lateral simulations.

The aircraft was then given larger longitudinal and lateral commands. The altitude change command was raised to 100m at a climb rate of 1 m/s. The roll angle command was raised to 20°. Instead of commanding a step input in roll as before, the aircraft was given a constant roll rate increase of 1 deg/s. The results are shown in Fig. 4.15. The aircraft matches all the commands well. The velocity excursions are actually smaller than in previous simulations, and are less than 0.25 m/s. The control inputs for this simulation are shown in Fig. 4.16. The control inputs are similar to previous simulations, and all remain relatively small.

The aircraft was then given the same, larger commands in the presence of a 2-s repeating gust, with the results in Fig. 4.17. The altitude and roll angle are virtually identical in still air and with the gust. The gust simulation has significantly larger yaw excursions. The velocity excursions for the gust simulation are also larger after the aircraft has leveled off. The root curvature looks similar, with the gust response being more oscillatory. A comparison between the control signals in the still air and gust simulations is shown in Fig. 4.18. The aileron controls are similar, with the gust being slightly more oscillatory. However the other controls all show more control effort needed in the gust simulations than in the still air case.

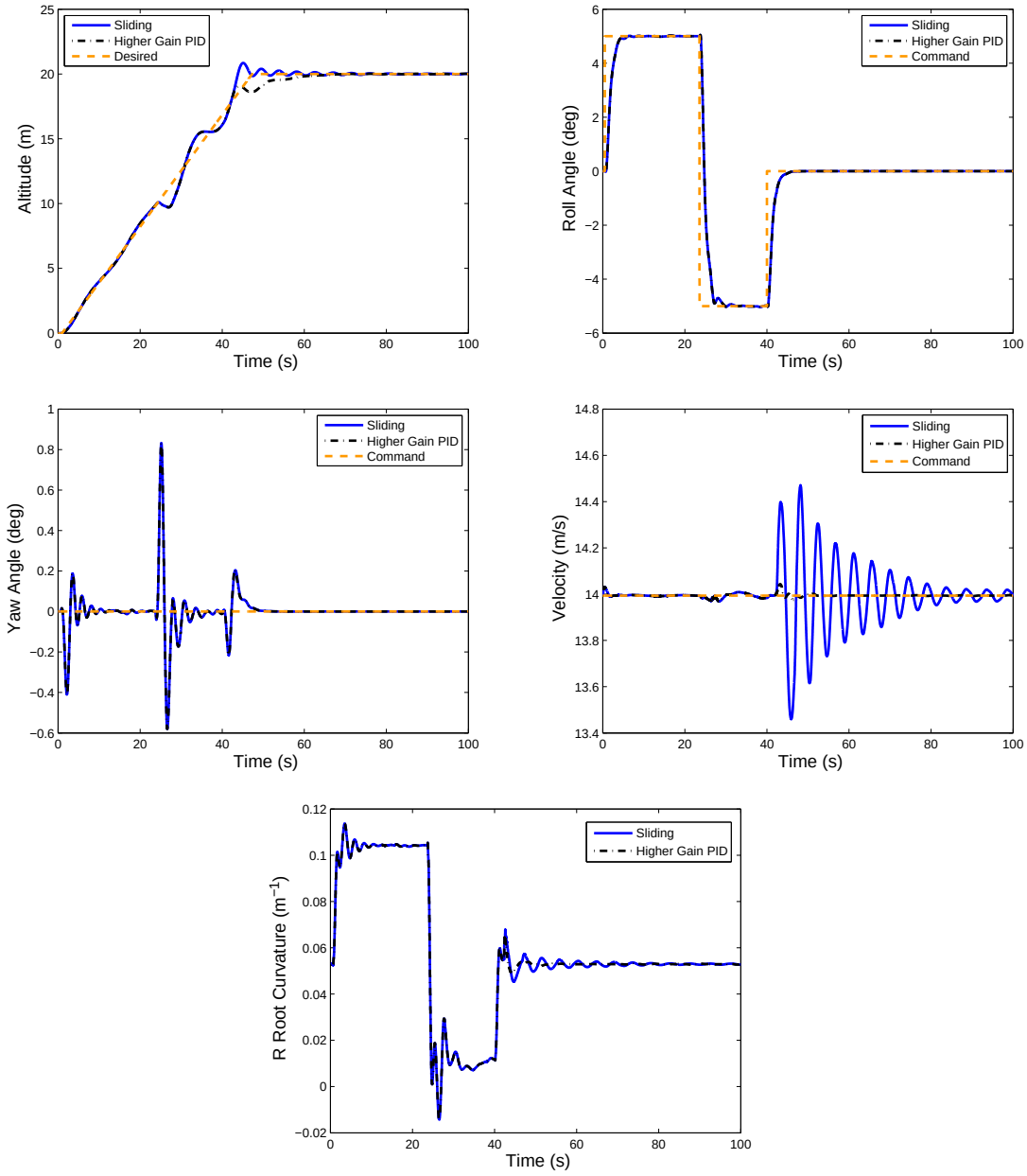

Figure 4.13: Combined longitudinal and lateral tracking response.

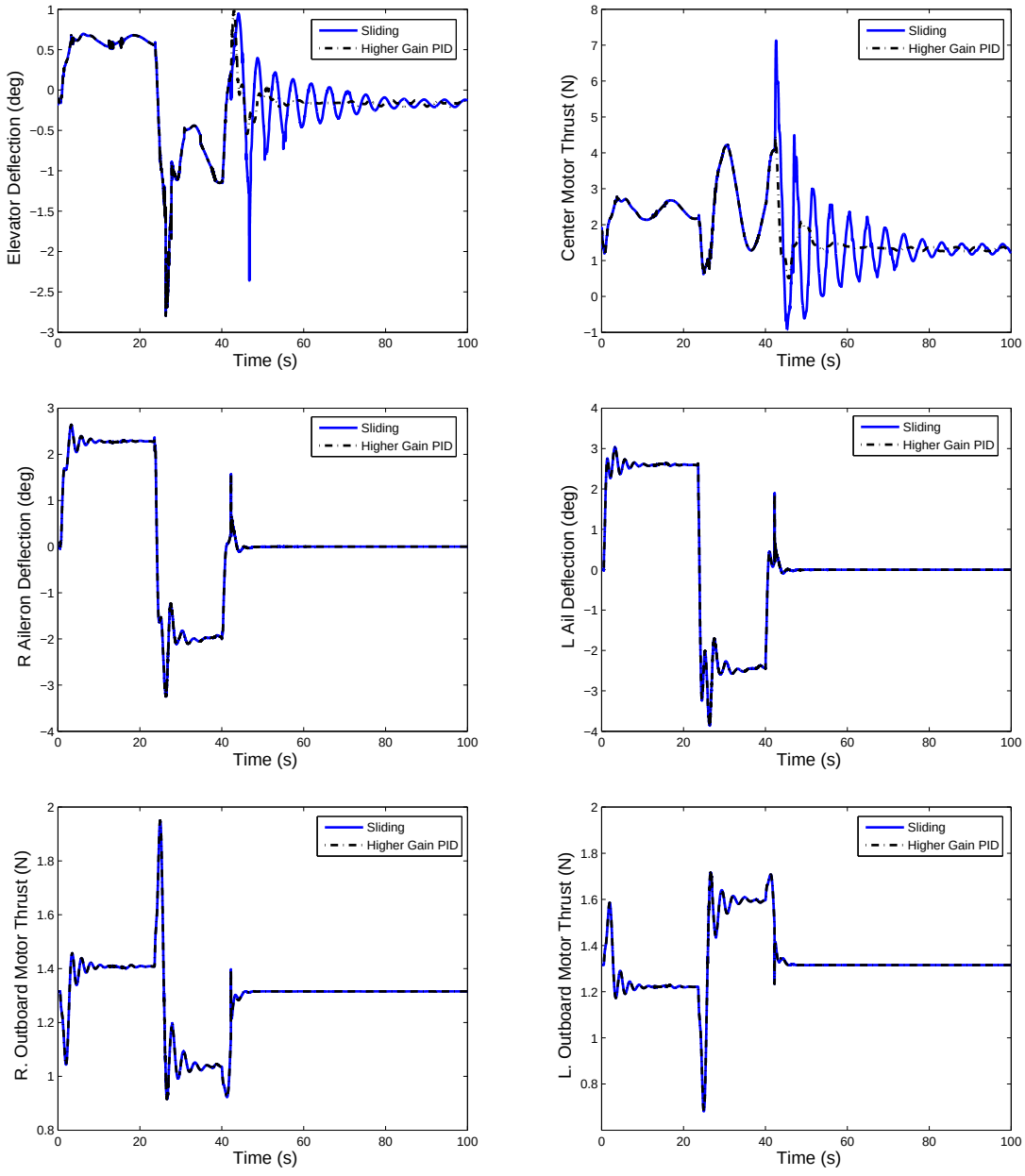

Figure 4.14: Combined longitudinal and lateral tracking control inputs.

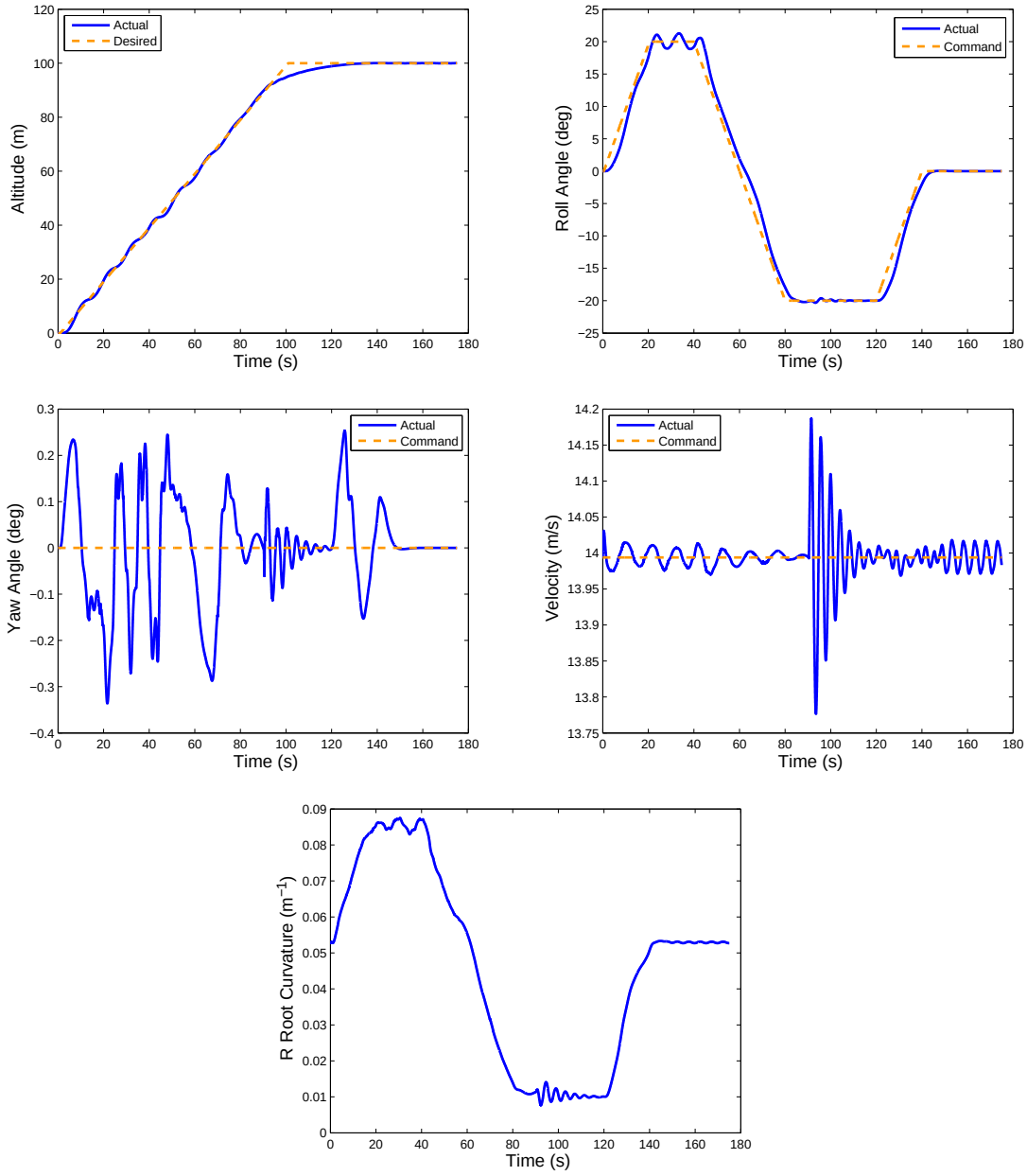

Figure 4.15: Combined longitudinal and lateral tracking response with larger commands.

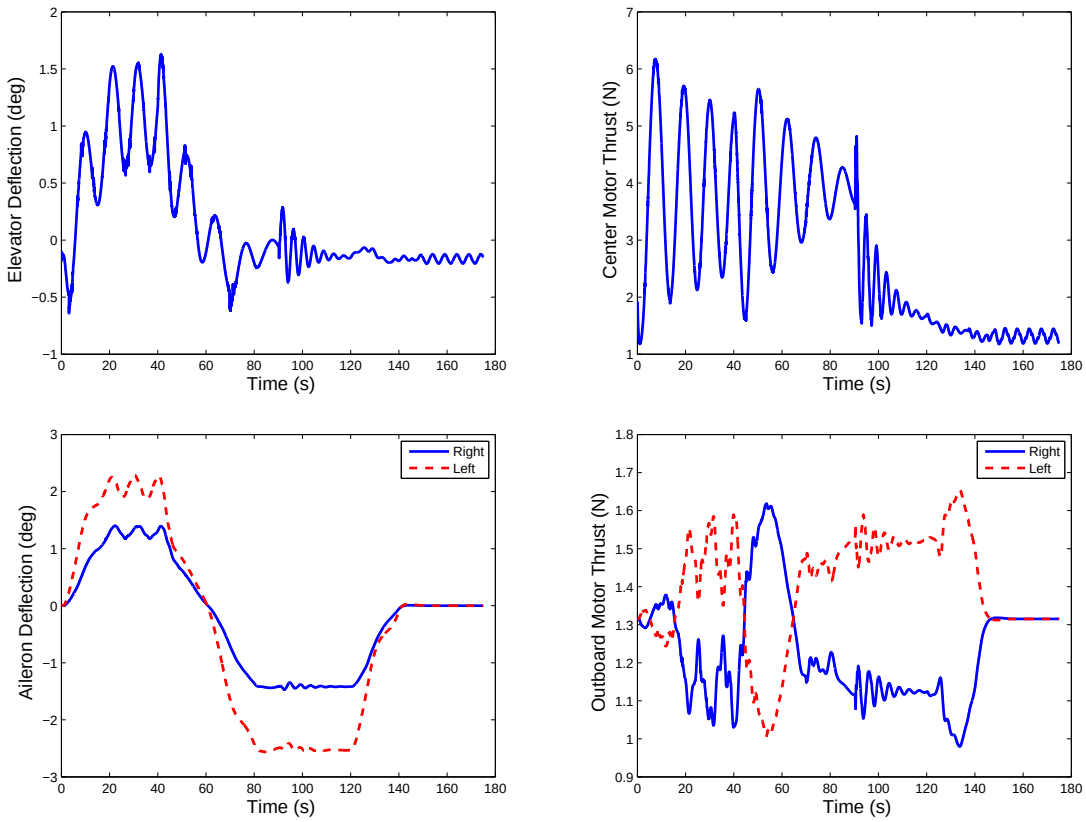

Figure 4.16: Combined longitudinal and lateral tracking with larger commands control inputs.

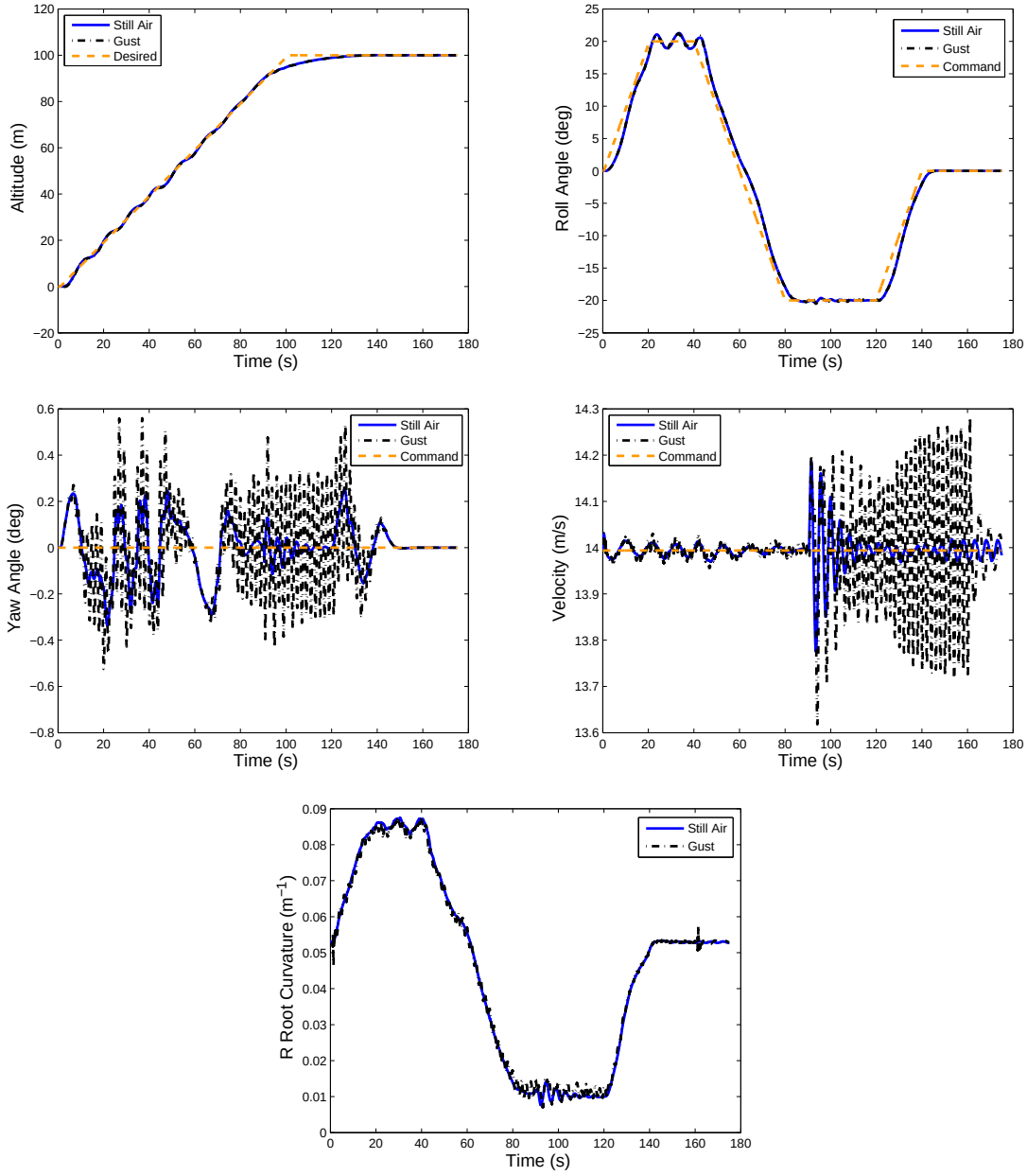

Figure 4.17: Combined longitudinal and lateral tracking response with larger commands and 2-s gust.

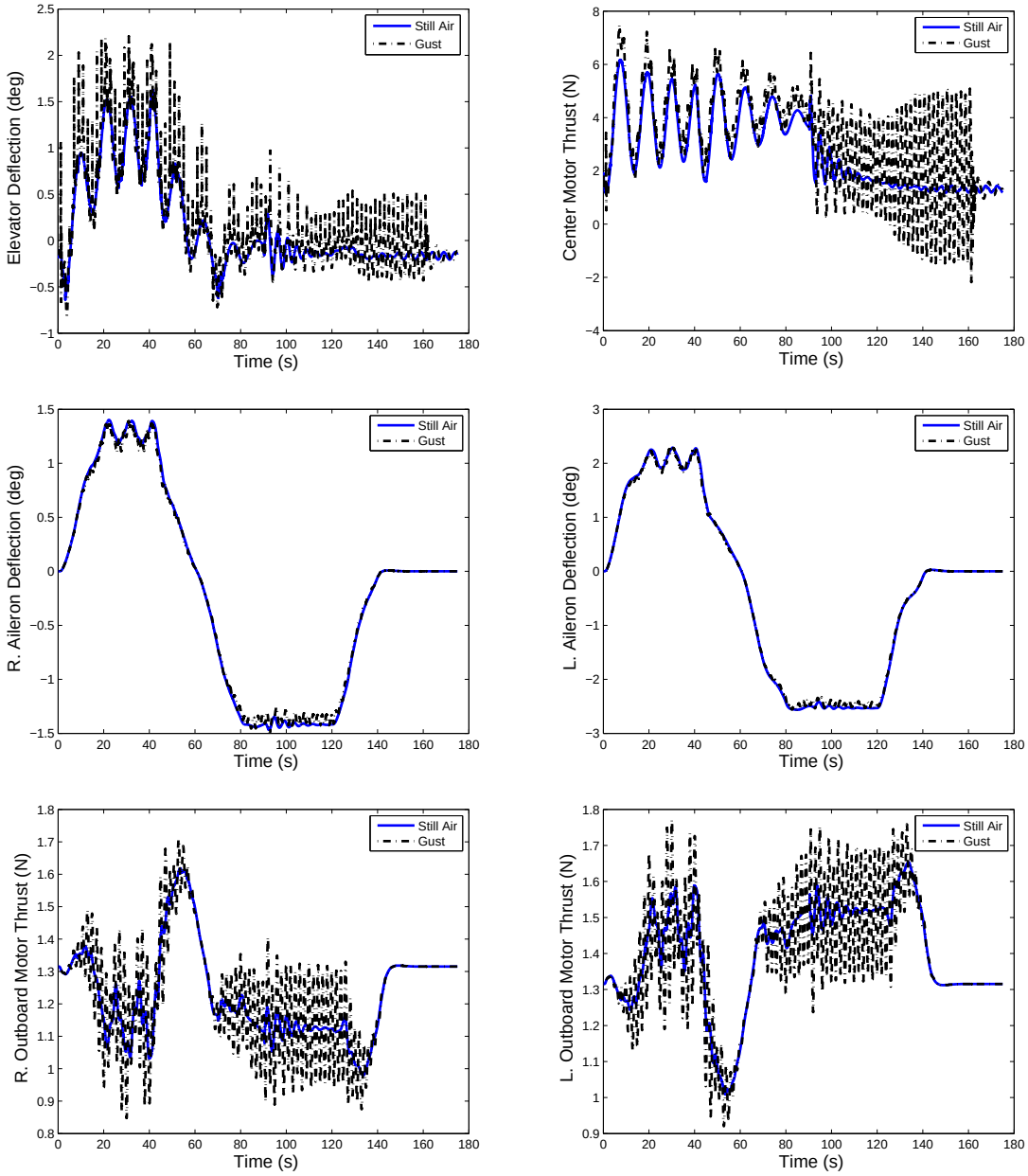

Figure 4.18: Combined longitudinal and lateral tracking with larger commands control inputs and 2-s gust.

4.4 Trajectory Control in Gust Concluding Remarks

A method for tracking longitudinal and lateral trajectory commands has been demonstrated on the X-HALE aircraft model. The PID-type outer loop controller in the two-loop longitudinal control architecture developed by Shearer and Cesnik [16] was shown to be unstable for the X-HALE model. Two different outer loop controllers, one that switches to a higher gain PID controller in the leveling off phase and one that uses a sliding mode controller in the leving off phase, were shown to be effective. The longitudinal control scheme was also demonstrated to perform well in the presence of various gust disturbances. The controller was shown to track longitudinal commands with the gust disturbances as long as the control update time was increased to at least 20 Hz. A lateral LQG controller designed using a reduced order linear aircraft model was shown to effectively track lateral commands, with the response in gust more oscillatory than still air, but still acceptable. Finally, tracking of simultaneous longitudinal and lateral commands, in still air and in gust, was demonstrated.

CHAPTER 5

Curvature Reducing Control

This chapter presents two approaches for reducing the wing curvature, and therefore the bending moment, of the aircraft in maneuvering flight with gust disturbances. The first approach is based on LQR control theory applied to coordinated aileron control. The second approach uses reference and extended command governors to modify the set point commands to enforce hard limits on the curvatures. While these developments are based on several assumptions, such as the availability of the entire vector of elastic states for feedback in the first approach, they clearly demonstrate the feasibility of curvature reduction control through novel use of actuators and control algorithms.

5.1 Curvature Reducing LQR

In this section, an approach which utilizes coordinated control of ailerons to reduce wing curvatures induced by maneuvering flight and by the gusts is presented. The controller is an LQR that uses the entire vector of elastic states as well as integrators on deviations from trim values of the right and left root curvatures for feedback. The cost functional weights tracking errors and control effort by ailerons. Since the wing curvatures are proportional to bending moment, this approach reduces the bending moments of the aircraft. All of the elastic states also use the trim values as the baseline, meaning the goal of the controller is to have the aircraft remain at the trimmed shape while maneuvering with a

gust disturbance. Alternatively, the trim shape corresponding to the predicted mean value of the gust could have been used as a baseline.

The aircraft was given the same 20 m climb command in the presence of the four gust disturbances as in Section 4.1.3, with the ailerons coordinated by the LQR controller to reduce the curvature. The results comparing performance with and without the curvature reducing LQR in the presence of a 2-s gust disturbance are shown in Fig. 5.1. The same longitudinal controller described in Section 4.1 is used to control the climb by coordinating the elevator inputs and thrust of the three inboard motors. The difference in altitude tracking between the two controllers is negligible. However, there is a large difference between the root curvatures with the two controllers. The maximum root curvature deviation from trim value is reduced by 31% with the curvature reducing controller. When examining a zoomed in view of the root curvature as shown in Fig. 5.2, one can see the original controller peaks up and down quickly, also resulting in two peaks with the curvature reducing controller. If these peaks are excluded, the curvature reducing benefit increases to 54%.

The comparison plots for the 4-s, 8-s and Dryden gust disturbances, with and without the curvature reducing controller, are shown in Figs. 5.3 - 5.5. The plots show virtually identical altitude tracking with and without the curvature reducing controller for all of the gust disturbances. The curvature reducing controller works well with all the gusts, and the root curvature is reduced by 66%, 40% and 76%, respectively, for the 4-s, 8-s and Dryden gusts. Due to the relatively small tip deflections, the maximum of which is approximately 0.015m, the aileron deflections are kept small, with the largest value across all simulations of approximately 0.4°.

The use of the curvature reducing LQR was then tested using the larger combined trajectory tracking commands that include roll and yaw commands. The aileron commands from the curvature reducing LQR were added to those from the lateral controller. Note that the lateral controller also uses outboard motors as actuators. At first, the results were very poor, but then the gains were lowered significantly, with the results shown in Fig. 5.6. The

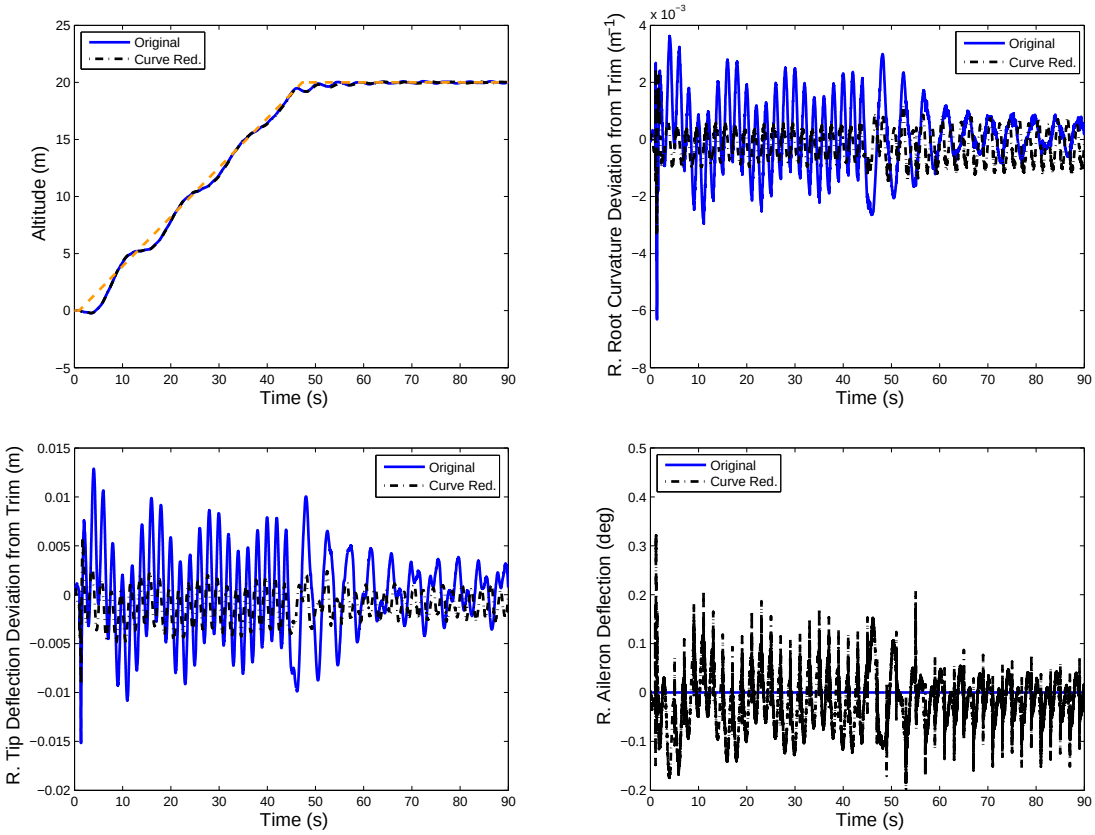

Figure 5.1: Comparison of altitude tracking with and without curvature reducing controller in 2-s duration gust.

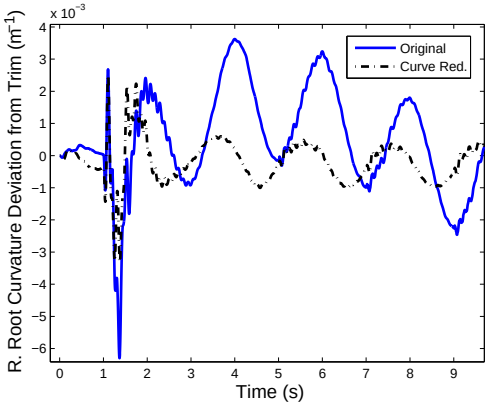

Figure 5.2: Zoomed in view of root curvature with and without curvature reducing controller.

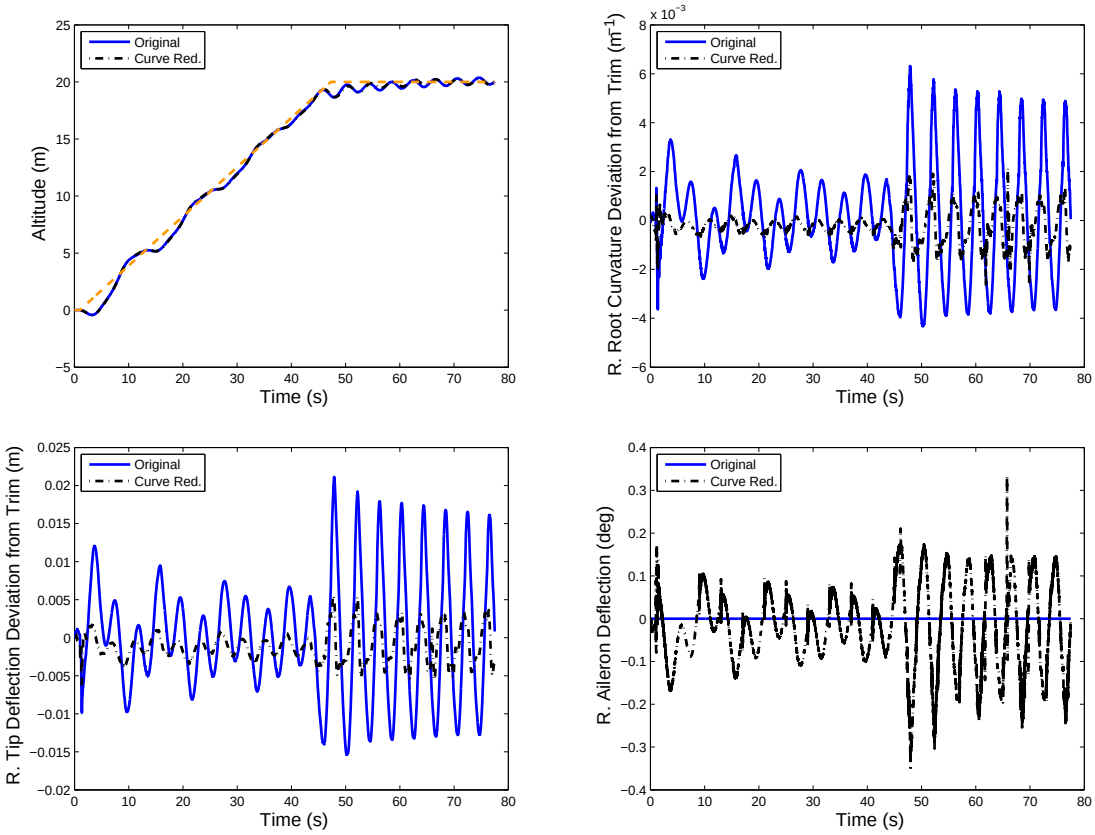

Figure 5.3: Comparison of altitude tracking with and without curvature reducing controller in 4-s duration gust.

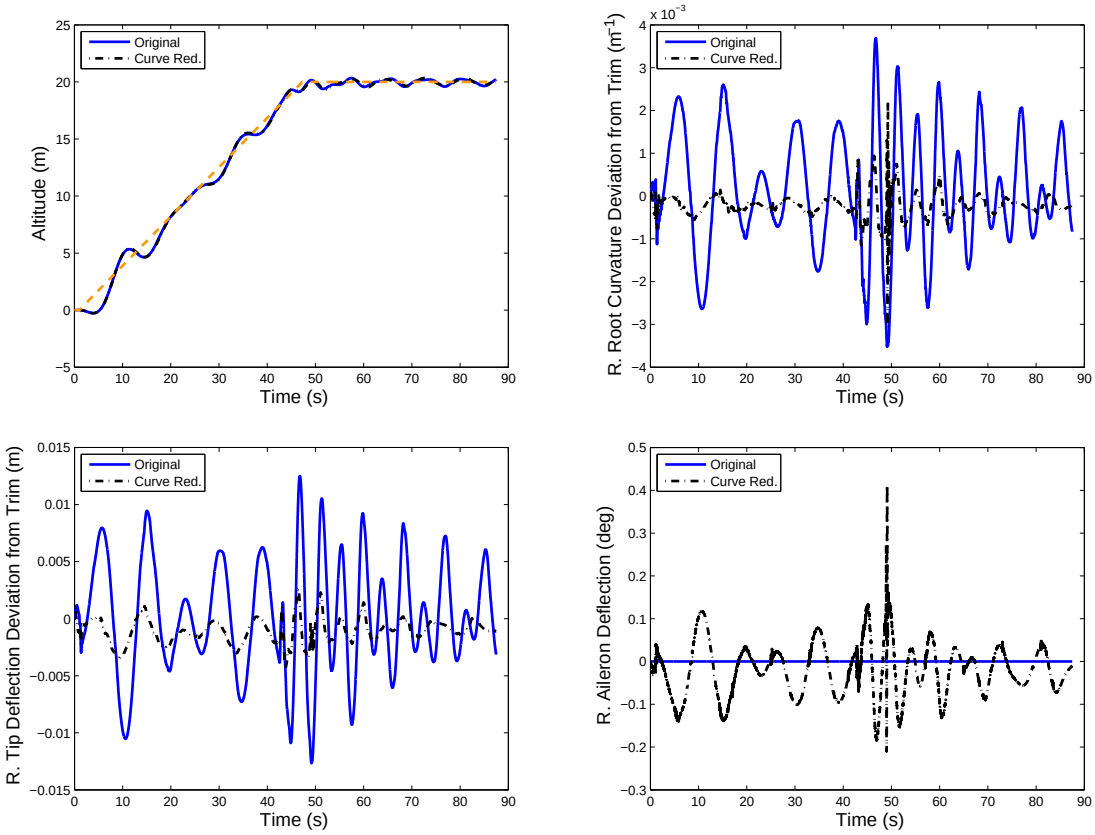

Figure 5.4: Comparison of altitude tracking with and without curvature reducing controller in 8-s duration gust.

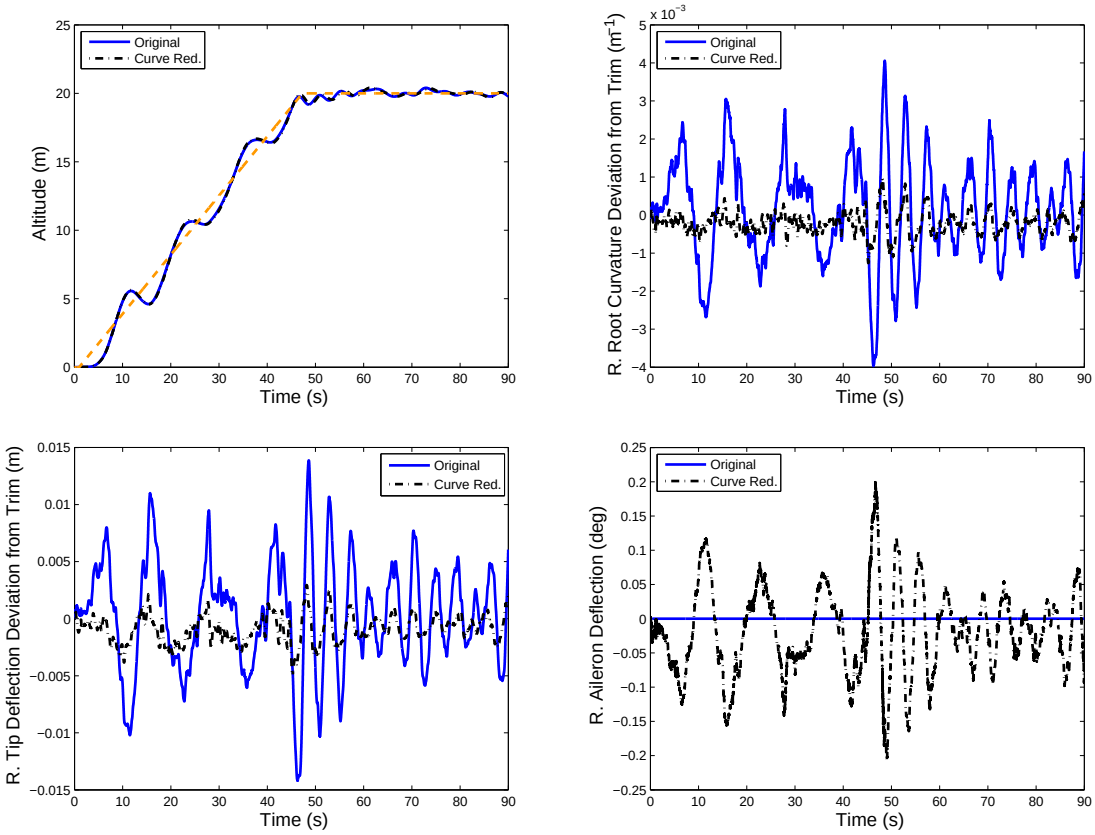

Figure 5.5: Comparison of altitude tracking with and without curvature reducing controller in Dryden gust.

aircraft initially has a larger root curvature with the curvature reducing controller, but then the curvature reducing controller is able to reduce the root curvature. The same behavior is seen when the aircraft rolls from 20° to -20°. Examining the aileron responses gives an idea of why this is happening. The controllers are essentially working against each other. In order to roll the aircraft, the ailerons deflect, causing an increase in curvature. This increase then causes an increased aileron command from the curvature reducing controller. After the aircraft has completed the roll, the curvature reducing controller can then effectively reduce the curvature values. Further development of the architecture of the combined lateral and curvature reducing controller is left to future work.

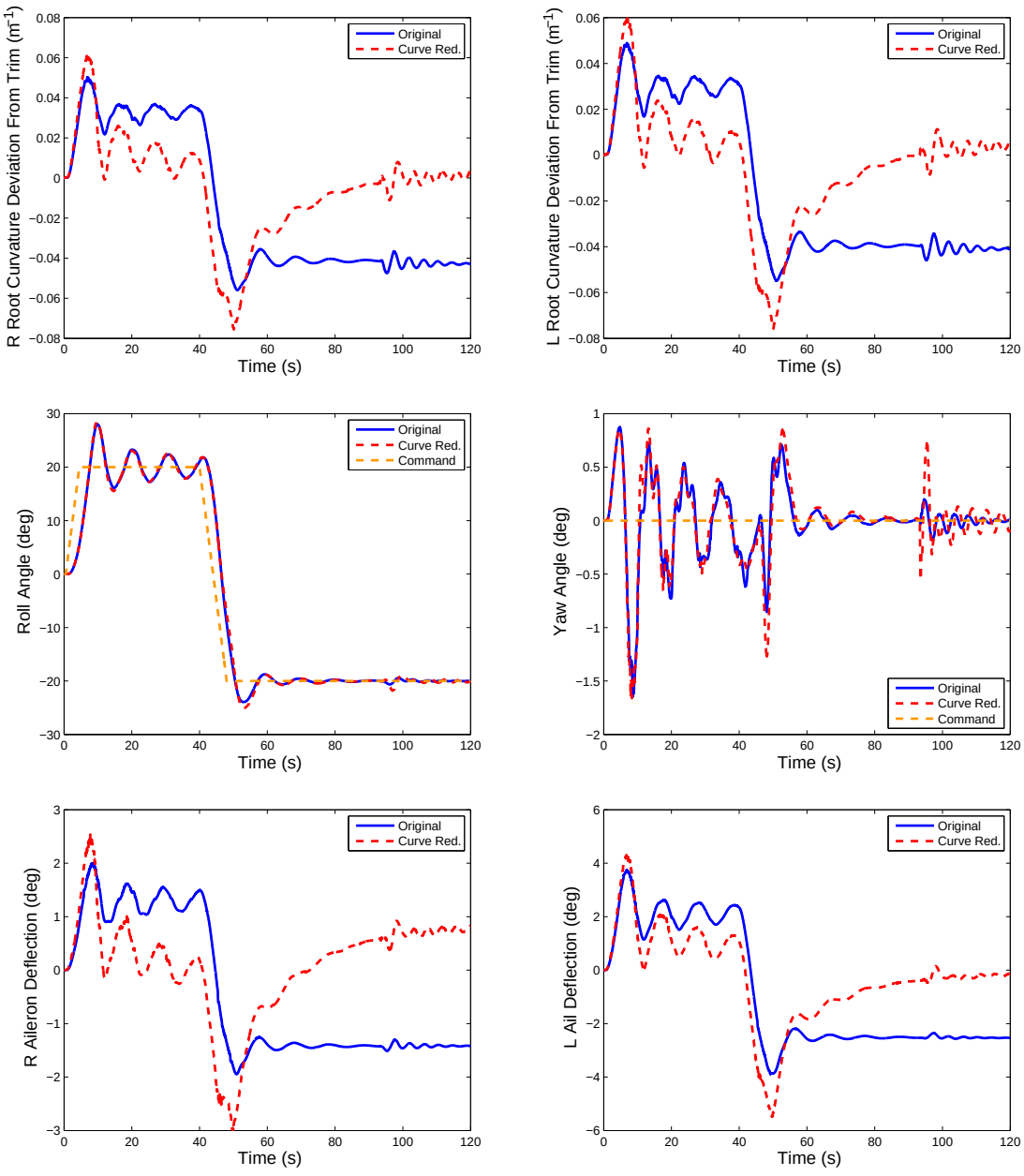

Figure 5.6: Comparison of response with and without curvature reducing controller.

5.2 Reference and Extended Command Governors

5.2.1 Reference Governor

A reference governor (RG) is a method for enforcing limits on states and controls by modifying the reference commands[52]. The RG is applied to constrained discrete-time linear time-invariant closed loop systems with disturbances [53],

$$x(t+1) = Ax(t) + Bv(t) + B_w w(t), \tag{5.1}$$

$$y(t) = Cx(t) + Dv(t) + D_w w(t) \in Y,\ \forall t \in \mathbb{Z}_+ \tag{5.2}$$

where $x(t) \in \mathbb{R}^n$ is the state vector of the closed-loop system, $v(t) \in \mathbb{R}^m$ is the set point, $w(t) \in \mathbb{R}^q$ is the disturbance input, $Y \subset \mathbb{R}^p$ is a convex-polyhedral constraint set, and $\mathbb{Z}_+$ is the set of all non-negative integers. The disturbance is unmeasured and set-bounded, meaning $w(t) \in W$.

Since Eqs. 5.1 and 5.2 represents the dynamics of the closed loop system, Eq. 5.2 can represent combined state and control input constraints with appropriate choice of $y(t)$.

When using an RG, Eqs. 5.1 and 5.2 normally represents a closed loop system containing both the plant and controller, with asymptotically stable dynamics. The RG generates a command input to the closed loop system, $v(t)$, based on the current state estimate, $x(t)$, and desired command input, $r(t) \in \mathbb{R}^m$, which is assumed to be constant over the prediction horizon. The command input is generated with the help of the set of all safe initial-state/constant-input pairs,

$$O_\infty = \{(x(0), v) : v(t) \equiv v, \text{(5.1)-(5.2) are satisfied for all } w(t) \in W\}. \tag{5.3}$$

Given a state measurement or estimate, $x(t)$, the RG determines $v(t)$ so that,

$$(x(t), v(t)) \in P \subset O_\infty, \tag{5.4}$$

where P is a finitely-determined approximation of O_∞ which can be expressed as a set of linear inequalities [54],

$$P = \{(x, v) : H_x x + H_r v \leq h\}. \tag{5.5}$$

The command input to be passed to the closed loop system is then determined by [52],

$$v(t) = v(t-1) + \kappa(t)(r(t) - v(t-1)), \tag{5.6}$$

where $0 \leq \kappa(t) \leq 1$ is a scalar parameter maximized so that Eq. 5.4 is satisfied; this optimization is explicitly solvable and because $\kappa(t)$ is the only parameter that is optimized online, this greatly simplifies the computational complexity versus alternative constraint enforcing schemes such as Model Predictive Control.

If the RG determines that, based on the current state, a constant reference input, $r(t) \equiv r$, will not violate the constraints for any future time, the RG will pass $v(t) = r$ to the closed loop system, thereby not interfering with the system. The RG modifies the reference signal only if it predicts constraint violation, and makes sure that the reference input is modified as little as possible while preventing constraint violation.

5.2.2 Extended Command Governor

The Extended Command Governor (ECG) approach is an extension of the RG and was first introduced in [55]. The ECG determines $v(t)$ according to,

$$v(t) = \bar{C}\bar{x}(t) + \rho(t), \tag{5.7}$$

where $\bar{x}(t) \in \mathbb{R}^{\bar{n}}$ is an auxiliary state variable with the following dynamics,

$$\bar{x}(t+1) = \bar{A}\bar{x}(t), \tag{5.8}$$

and $\rho(t)$ is assumed to be constant over the prediction horizon.

Coupled with Eqs. 5.1 and 5.2, the complete system dynamics are,

$$\begin{bmatrix} x(t+1) \\ \bar{x}(t+1) \end{bmatrix} = \begin{bmatrix} A & B\bar{C} \\ 0 & \bar{A} \end{bmatrix} \begin{bmatrix} x(t) \\ \bar{x}(t) \end{bmatrix} + \begin{bmatrix} B \\ 0 \end{bmatrix} \rho(t) + \begin{bmatrix} B_w \\ 0 \end{bmatrix} w(t), \tag{5.9}$$

$$y(t) = \begin{bmatrix} C & D\bar{C} \end{bmatrix} \begin{bmatrix} x(t) \\ \bar{x}(t) \end{bmatrix} + D\rho(t) + D_w w(t), \tag{5.10}$$

where the output is constrained as with the RG,

$$y(t) \in Y, \ \forall t \in \mathbb{Z}_+. \tag{5.11}$$

Defining an augmented version of Eq. 5.4,

$$O_\infty^{aug} = \{(x(0), \bar{x}(0), \rho) : \rho(t) \equiv \rho, \text{(5.9)-(5.11) are satisfied for all } w(t) \in W\}, \tag{5.12}$$

a new constraint is formed,

$$(x(t), \bar{x}(t), \rho(t)) \in P^{aug} \subset O_\infty^{aug}, \tag{5.13}$$

$$P^{aug} = \{(x, \bar{x}, \rho) : H_x x + H_{\bar{x}} \bar{x} + H_r \rho \leq h\}. \tag{5.14}$$

Given Eq. 5.13, the pair $(\bar{x}(t), \rho(t))$ is calculated by solving a minimization problem,

$$(\bar{x}(t), \rho(t)) = \underset{(x(0), \bar{x}, \rho)}{\arg\min} \ ||\bar{x}||_{\bar{S}}^2 + ||\rho||_S^2, \tag{5.15}$$

where $S = S^{\mathrm{T}} > 0$ and $\bar{S} > 0$ satisfies the condition, $\bar{A}^{\mathrm{T}}\bar{S}\bar{A} - \bar{S} < 0$. With this choice, the ECG has properties similar to the RG, such as constraint admissibility and finite-time convergence to a constant reference.

The matrices $\bar{A}$ and $\bar{C}$ are chosen to generate orthogonal Laguerre sequences,

$$\bar{A} = \begin{bmatrix} \alpha I & \gamma I & -\alpha\gamma I & \alpha^2\gamma I & \cdots \\ 0 & \alpha I & \gamma I & -\alpha\gamma I & \cdots \\ 0 & 0 & \alpha I & \gamma I & \cdots \\ 0 & 0 & 0 & \alpha I & \cdots \\ \vdots & \vdots & \vdots & \vdots & \ddots \end{bmatrix}, \tag{5.16}$$

$$\bar{C} = \sqrt{\beta}\begin{bmatrix} I & -\alpha I & \alpha^2 I & \cdots & (-\alpha)^{\bar{n}/m-1} I \end{bmatrix}, \tag{5.17}$$

where $0 \leq \alpha < 1$ is the eigenvalue of the $\bar{x}(t)$ dynamics, $\gamma = 1 - \alpha^2$, and $I \in \mathbb{R}^{m\times m}$ is the identity matrix. The parameters α and $\bar{n}$ are design choices. As compared to the RG, an ECG can provide a larger constrained domain of attraction and faster transient response.

5.2.3 Disturbance Handling

The regular treatment of disturbances in RG and ECG design is conservative, because it assumes that $w(t)$ can take any value in the set W for all $t \in \mathbb{Z}_+$. In the RG and ECG designs pursued in this work, we instead assume that $w(t)$ stays constant over the prediction horizon. Specifically, these designs are based on modifying Eqs.5.5 and 5.14 to

$$P(w) = \{(x, v) : H_x x + H_r v \leq h - H_w w\}, \tag{5.18}$$

$$P^{aug}(w) = \{(x, \bar{x}, \rho) : H_x x + H_{\bar{x}}\bar{x} + H_r\rho \leq h - H_w w\}, \tag{5.19}$$

where we pass $w = w(t)$ and H_w is calculated according to the system dynamics, similarly to the rest of the inequality matrices. Furthermore, this work assumes that the current

value of w is known, but assumes no knowledge of future values. For implementation on an actual aircraft, the current value of w could be measured using on-board sensors or possibly estimated from aircraft states.

The constant disturbance does not guarantee constraint admissibility or recursive feasibility. It is therefore possible for the system to violate the constraints in the future if $w(t)$ does not stay constant. Although such a situation does not arise in the subsequent simulations, it can be alleviated through the use of "soft" constraint adherence, where a slack variable measures the amount of constraint violation and is minimized in the same way as a reference variable in order to minimize constraint violation.

5.3 RG and ECG Numerical Results

5.3.1 Flying Wing Model RG and ECG Numerical Results

In order to validate the RG and ECG approach on VFA models, the approach was first tried on the Flying Wing Model described in Chapter 3. The aircraft model was reduced to a single input-single output (SISO) system with elevator deflection as the input and pitch rate as the output. The dynamic inversion controller described in Chapter 4 was used, but since the system was modeled as a SISO system, Eqn 4.18 was modified to,

$$C_{long} = \begin{bmatrix} 0 & 0 & 0 & 1 & 0 & 0 \end{bmatrix}. \tag{5.20}$$

In this case, Eqn. 4.20 becomes,

$$\begin{bmatrix} \dot{\beta} \\ \dot{z}_{long} \end{bmatrix} = \begin{bmatrix} 0 & 0 \\ C_{long} & 0 \end{bmatrix} \begin{bmatrix} \beta \\ z_{long} \end{bmatrix} + \begin{bmatrix} 1 \\ 0 \end{bmatrix} v_{long} - \begin{bmatrix} 0 \\ 1 \end{bmatrix} \omega_{Bx,com}, \tag{5.21}$$

A wind gust similar to the gust described in Section 3.2.1 was used. It is a $1 - \cos$ discrete gust with a two second durations, after which it remains at zero. The gust also has

a sinusoidal spanwise distribution. The aircraft was given a single period flight path angle square wave command with amplitude of one degree. A comparison between the aircraft response in still air and gust is shown in Fig. 5.7. In still air, the aircraft tracks the command well, with the response being slightly damped, due to the flexibility of the aircraft. The gust causes the aircraft to first develop a negative flight path angle. The controller is then able to act and forces the flight path angle back in the correct direction, but this aggressive change in flight path angle also causes a significant overshoot. After this initial overshoot dies down the aircraft response is similar to that of the still air simulation.

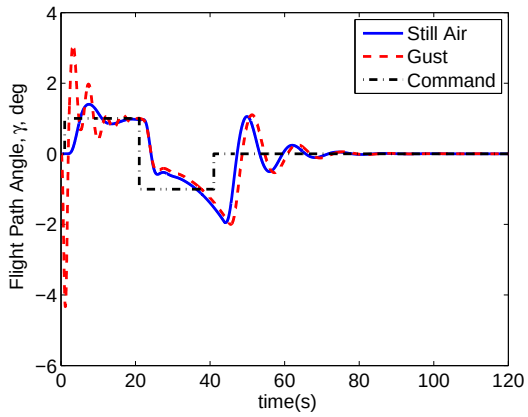

Figure 5.7: Flight path angle command tracking in still air and with gust disturbance.

Both the RG and ECG implementation require a linear model of the closed loop system. As described in Section 3.2.1, it was not possible to obtain an accurate linearization of the open loop aircraft analytically. Therefore, system identification was used to identify a linear model of the *closed loop* dynamics of the system. The input to the closed loop system is the commanded flight path angle and the output is the root curvature on the right side of the aircraft. Only the root curvature on one side of the aircraft is needed due to the assumed symmetric form of the maneuver and gust. Separate linear models were identified in MATLAB using various tools in the System Identification Toolbox for the root curvature in still air and in gust using nonlinear data obtained from UM/NAST. A comparison between nonlinear and linear simulation response is shown in Figs. 5.8. There

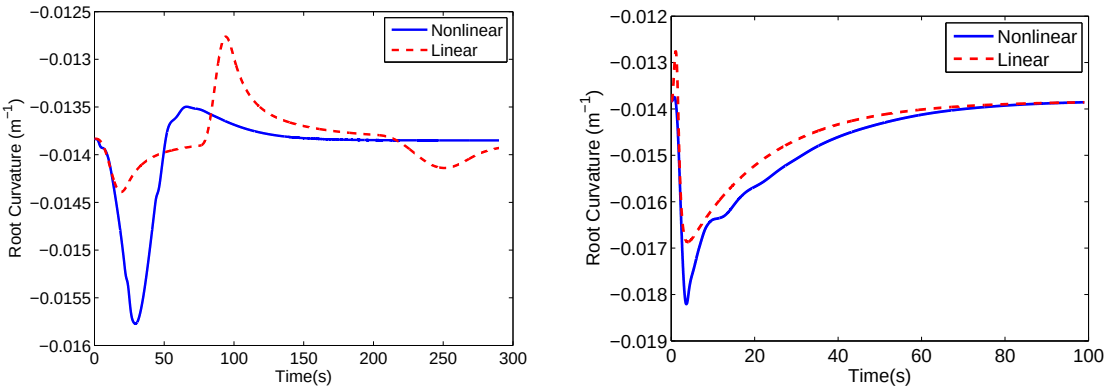

Figure 5.8: Root curvature comparison in still air (left) and in gust (right).

is not a good correlation between root curvature values during maneuvering flight in still air, but the agreement is better for root curvatures caused by the gust.

The aircraft was given a single period, square wave flight path angle command in still air. The simulations were first run without a governor included, and then repeated with an RG or an ECG in the loop to enforce constraint limits on root curvature. When a RG or an ECG is included, the linearized closed loop model is used to predict whether a constraint violation would occur. The constraint value on the root curvature was set to 0.001. This value was somewhat arbitrarily chosen so that the constraint would be violated without the RG or ECG intervening. This formulation only considered the wing curvature at one point on the wing, but could be extended to include additional points.

The RG and ECG require a complete state vector to determine if the constraints will be violated. The states used in this formulation have no physical meaning because the linearization was obtained using system identification. Therefore a state estimator has to be used to construct an estimate of the current state vector. This will induce some errors into the system, as well as the errors caused by the fact that a linearized system is used to approximate the nonlinear dynamics. To account for these errors, a variable is introduced which characterizes the difference between the current output of the nonlinear model (i.e.

actual system) and its prediction based on the linear model, [56]:

$$\tilde{y} = y_{NL} - y_{Lin}. \tag{5.22}$$

Then $\tilde{y}$ is used to modify the sets P and P^{aug} which are the finite approximations of O_∞. Eqns. 5.18 and 5.19 then become

$$P(w) = \{H_x x + H_r v \leq h - H_w w - \tilde{y}\}, \tag{5.23}$$

$$P^{aug}(w) = \{H_x x + H_{\bar{x}} \bar{x} + H_r \rho \leq h - H_w w - \tilde{y}\}, \tag{5.24}$$

This modification essentially allows P and P^{aug} to be expanded and contracted to account for the modeling errors. the approach effectively corresponds to assuming that the same output error will remain over the prediction horizon.

The results for the still air simulation with curvature limits are shown in Fig. 5.9. The RG successfully enforces the curvature limits, but in order to do so, significantly modifies the flight path angle command. The RG determines that there will be a constraint violation in steady state, and therefore it restricts the maximum flight path angle to values that will not violate the constraint. The conservative reponse of RG is perhaps not surprising given that the linearized model obtained via system identification does not represent a good fit. On the other hand, the ECG restricts the command much less and is able to fully recover it in steady state. It also exhibits a slight constraint violation. This violation can be handled by imposing a slightly more conservative limit.

An ECG was unsuccessfully used to attempt to modify the aircraft's zero degree flight path angle to alleviate the curvature caused by the gust. In fact, modifying the flight path angle command does not appear to be an effective way to reduce root curvature. To informally illustrate this, the aircraft was given a 2-s duration one minus cosine elevator inputs with peak magnitudes of one and five degrees in order to cause a flight path angle change. The root curvature value caused by this elevator deflection was then measured and the re-

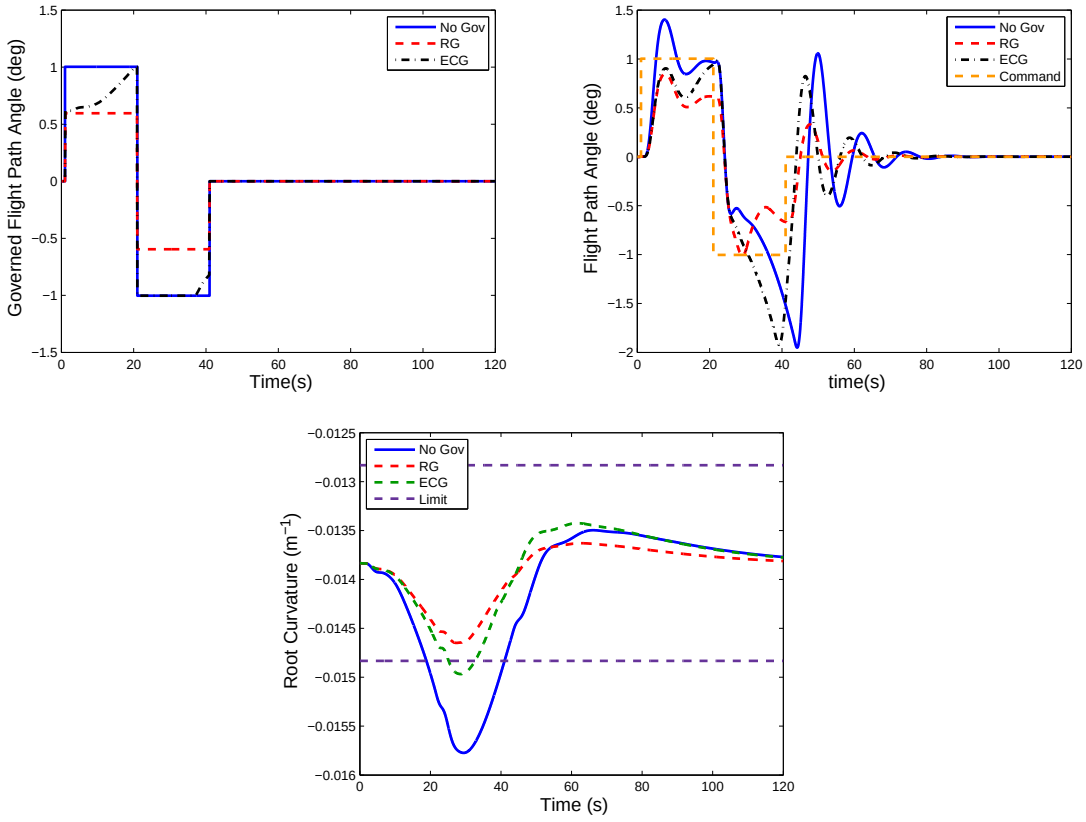

Figure 5.9: Comparison of flight path angle tracking with RG, ECG and no governor in still air simulation.

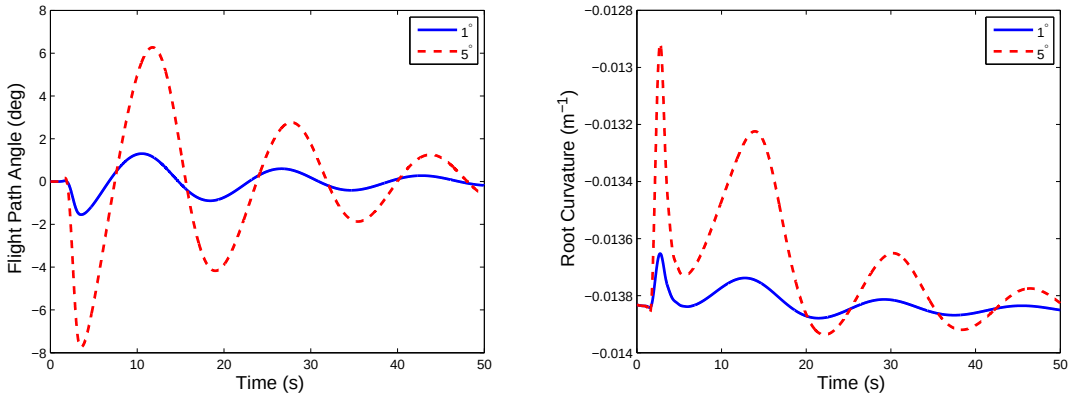

Figure 5.10: Response to $1 - \cos$ elevator inputs.

sults are shown in Fig. 5.10. In both simulations, the maximum change in root curvature per degree of flight path angle command was found to be approximately $0.0001\frac{m^{-1}}{deg}$. The maximum root curvature change caused by the gust was $0.0044m^{-1}$ and it occurred at 1.8 seconds. This suggests that to alleviate the curvature change caused by the gust, a flight path angle change of $44°$ in 1.8 seconds would be required, which is unreasonable for this type of aircraft. The use of coordinated ailerons, as shown in Section 5.1, thus emerges as a more effective approach to limit curvature changes caused by gust disturbances.

5.3.2 X-HALE RG and ECG Numerical Results

As described in Section 3.2.4 an accurate analytical linearization for X-HALE can be created using UM/NAST. This is beneficial for several reasons. First, a system identification approach need not be used. Second, the states of the linearization have physical meaning and are the same states used in the nonlinear simulations. Finally, the linearization tends to be more accurate than system identification based linearization, at least for small deviations. A comparison between the linear and nonlinear responses to the larger lateral tracking command from the combined tracking simulation is shown in Fig. 5.11. The root curvature was assumed to be caused by the lateral commands, and therefore only the lateral portion of the commands were used in the linear simulation. This was due to the fact that the lateral command tracking simulations showed much larger curvatures, and because it is

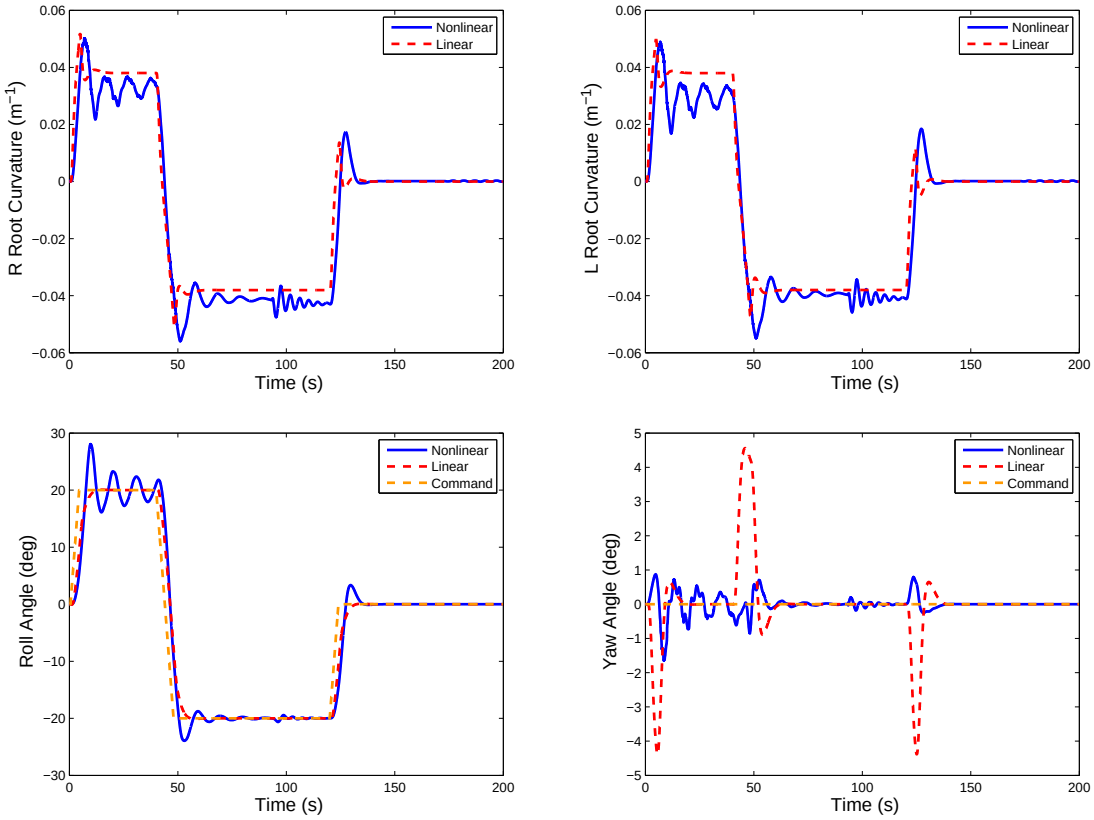

Figure 5.11: Comparison between linear and nonlinear X-HALE response to lateral commands.

very difficult to run a linear simulation using a nonlinear controller and multiple nonlinear transformations. There is a good agreement between the linear and nonlinear simulations in the root curvature and roll angle plots, although the linear simulations do not capture the oscillations well. Additionally, the linear models slightly under-predict the minimum value of the curvature occurring around 50 s. There is also some error in the yaw angle data, but this is of less importance in this work because yaw angle changes do not cause much, if any, curvature changes.

The RG and ECG were first simulated using the linear aircraft models. The strain limits were set at 0.04 and -0.045 so that the curvatures violated the limits at some time intervals during the simulations, but were within the limits in steady state. The results are shown in Fig. 5.12. The RG and ECG both successfully enforce the limits with a slight modification to the roll angle command. In order to better see the actions of the RG and ECG, plots

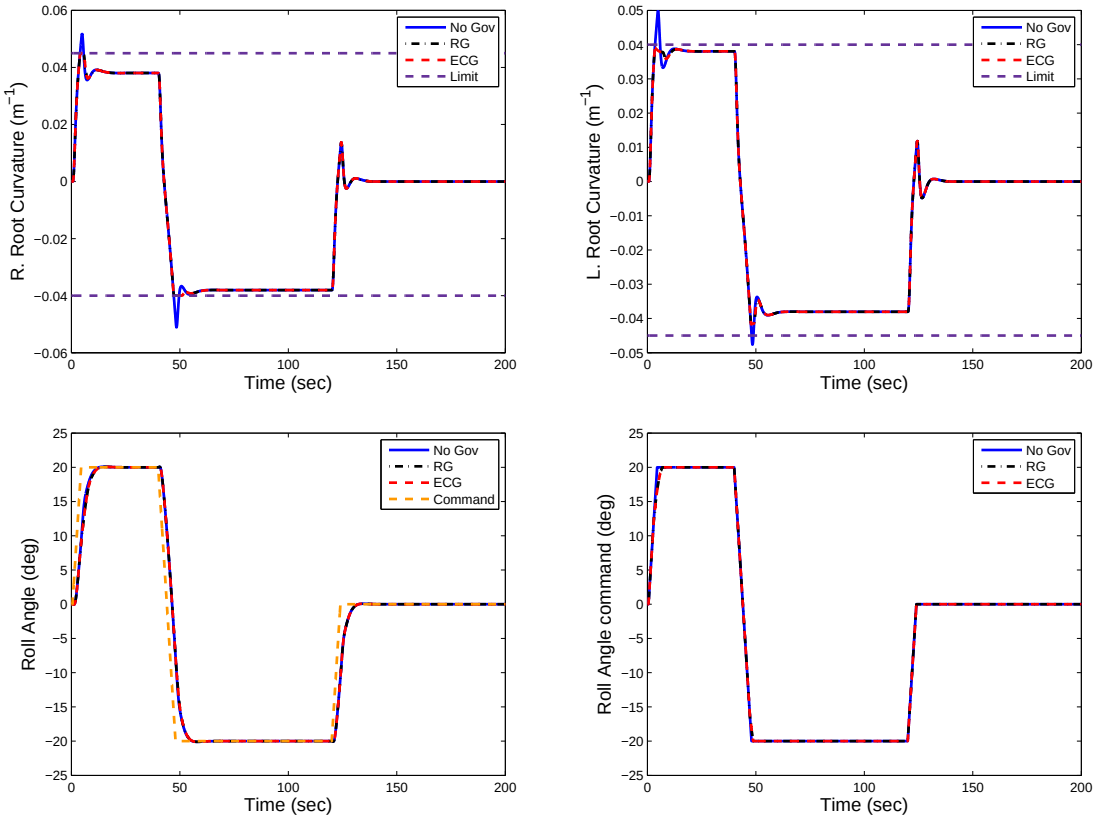

Figure 5.12: Linear response with RG and ECG.

zoomed into the maximum and minimum curvature values are shown in Fig. 5.12. By slightly modifying the roll angle command at the corner, the curvature peaks are reduced to stay within the limits.

The simulations were then repeated on the nonlinear model, using the same RG and ECG as in the linear simulations. The $\tilde{y}$ parameter was not used because the current nonlinear states could be used by the RG and ECG due to the fact that state estimation was not needed. The results are shown in Fig. 5.14. The RG and ECG both perform well during the first roll to 20°. Examining the zoomed in view of the right root curvature, shown in Fig. 5.15, one can see that the ECG successfully enforces the curvature limit, while the limit is very slightly violated with the RG. Additionally roll angle tracking performance is not significantly degraded. The aircraft rolsl slower with the governed commands, but the overshoot is also less. When the aircraft roll from 20° to -20° , the RG and ECG are able

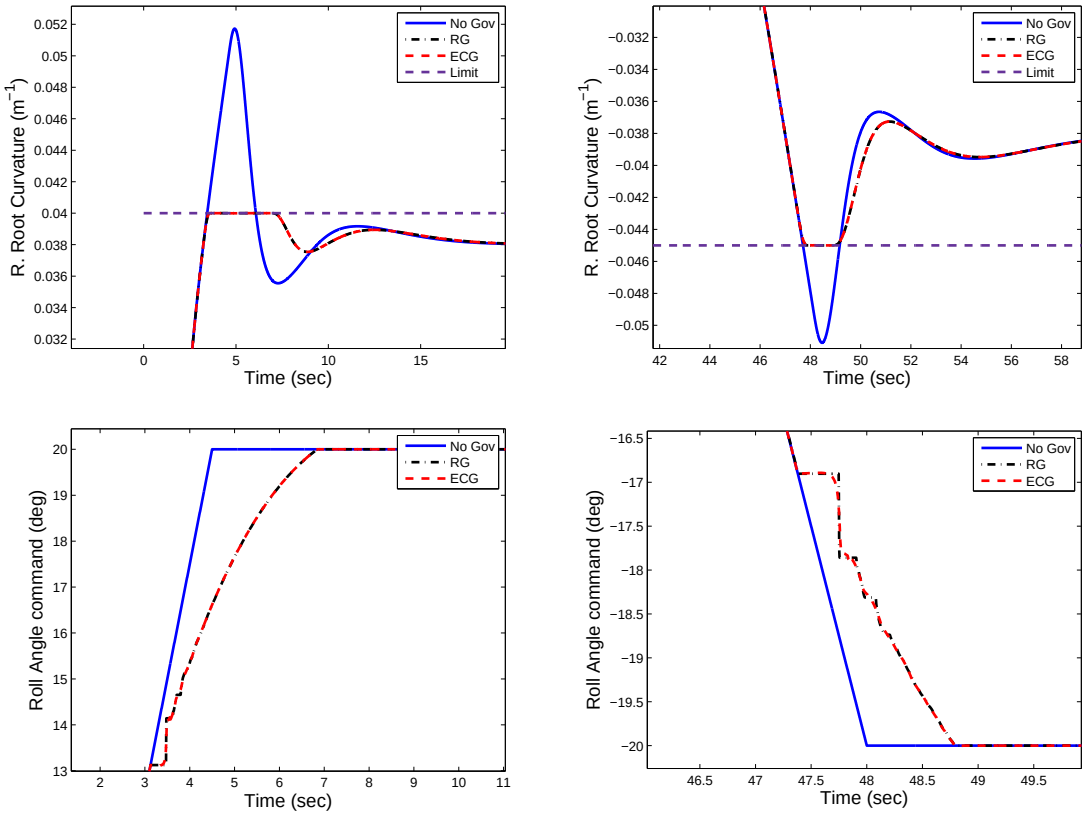

Figure 5.13: Zoomed in view of linear response with RG and ECG.

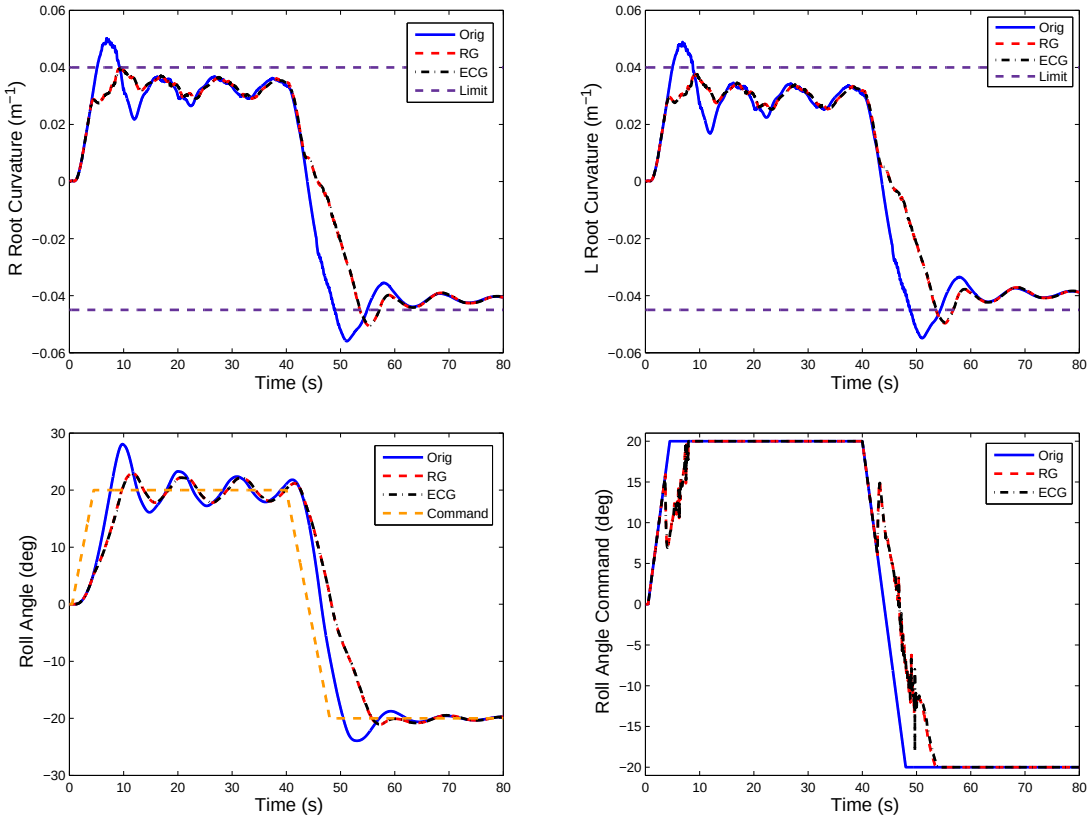

Figure 5.14: Nonlinear response with RG and ECG.

to reduce the curvature peak, however the limits are violated. This is due to the fact that the linearized model was not able to accurately predict the magnitude of this minimum in strain as was shown in Fig. 5.11. It should also be noted that a violation in this limit is not as significant as a violation of the positive limit. A violation of the limit in the negative direction means the aircraft shape is becoming closer to the jig shape.

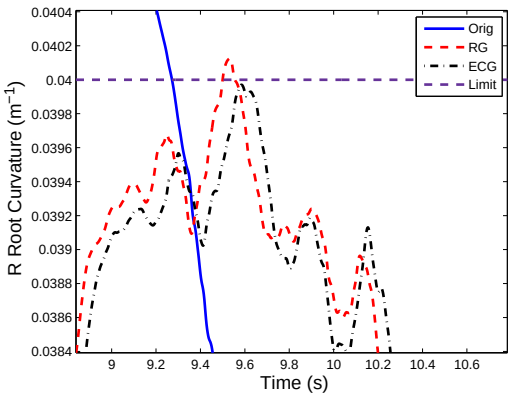

Figure 5.15: Zoomed view of nonlinear right root curvature response with RG and ECG.

5.4 Curvature Reducing Control Concluding Remarks

A novel method for minimizing wing curvature, and therefore aircraft bending moment, induced by a gust encounter or maneuvering flight was presented. This scheme uses an LQR controller relying on full elastic state feedback to command, in a coordinated fashion, the aileron inputs. The controller was designed to reduce the root curvature deviations from trim values. In longitudinal tracking simulation with a gust disturbance, the curvature reducing LQR controller performed very well, with curvature deviation reductions of up to 76% demonstrated and with no degradation in climb performance. When lateral commands were added, the controller did not perform as well. The initial curvature peak was higher with the curvature reducing controller, with subsequent values reduced. Further development of the combined lateral and curvature reducing controller will be pursued in future work.

As another approach to enforce limits on root curvature values, RG and ECG schemes were introduced into the system. The RG and ECG were first simulated on the flying wing model tracking flight path angle commands. An additional variable was added to account for the errors of the linearized system versus the nonlinear model. The governors were shown to effectively enforce the curvature limit, with a slight violation, yet less conservative response, in the ECG case.

The RG and ECG were then applied to the X-HALE model in a combined trajectory tracking simulation. The RG and ECG successfully enforced the curvature limits, with a very small violation with the RG, on the first curvature peak. However, the RG and ECG were not able to enforce the limit as the aircraft rolled from 20° to -20° due to the failure of the linearized model to accurately capture that nonlinear behavior. This simulation did not use additional variables that account for the differences between the linearized and nonlinear models.

CHAPTER 6

Conclusions and Recommendations

This chapter first summarizes the main conclusions of this work, and gives the key contributions of this dissertation. Finally, suggestions for future work and possible improvements are made.

6.1 Summary and Main Conclusions

A study of the sensitivity of two baseline VFA models to changes in wing stiffness was conducted. The stiffness properties of these two baseline aircraft were varied to create multiple aircraft simulation models. The open loop gust response and closed loop characteristics of these simulation models were examined. The results were compared as a function of the elastic frequencies, the rigid body flight dynamic frequencies, and various ratios of these frequencies. The results were found to be different for the two baseline aircraft models. For the flying wing model, the open loop pitch angle and root curvature response could not be simultaneously minimized, while the X-HALE results showed that the minimum pitch angle and root curvature occurred on the same set of parameters. The most important parameter for open loop response of the flying wing model was its bending stiffness, while the torsional stiffness was shown to be important for the X-HALE model. In fact, by increasing the torsional stiffness of the X-HALE baseline model, the maximum pitch angle was reduced by 26% and the maximum root curvature was reduced by 31%.

The closed loop response characteristics of both aircraft were dependent on the bending stiffness, while the in-plane bending stiffness was also important for the X-HALE.

A new longitudinal control architecture was developed departing from the previous work of [16]. In particular, a new method for generating aircraft flight path angle trajectories given a climb command was developed. After an instability was developed and found with the previous outer loop controller when implemented on X-HALE model, two new outer loop controllers were developed and were shown to perform well. AS the outer loop controller is intended to mimic the actions of a human pilot, the two schemes proposed in this dissertation are better at accomplishing this task. The complete longitudinal architecture was shown to accurately track altitude change commands in still air and in the presence of various discrete and continuous gust disturbances. It was also discovered that controls had to be updated twice as often as for the still air simulations to effectively reject the gust disturbance.

Lateral command tracking was demonstrated through the use of a linear controller designed using a reduced order linear model of the aircraft and the application of LQG theory. This approach only requires the measurement of four elastic states in addition to the rigid body states, where previous work required full elastic state feedback.

A novel method for reducing aircraft loads caused by an encounter with gust or by maneuvering flight has been defined. This method uses coordinated aileron commands to reduce wing curvature deviations from trim values, which is proportional to wing bending moment. The LQR curvature reducing controller has been designed assuming full elastic state feedback and has shown the ability to reduce curvature during climbs with small control effort.

Finally, a control architecture which combines the longitudinal and lateral control scheme with reference and extended command governors was demonstrated. The setup was shown to enforce curvature limits during longitudinal command tracking on the flying wing model, with slight constraint violations due to linear model and state estimation errors. This setup

was then shown to work well on the X-HALE aircraft with small constraint violations due to linear model errors.

To summarize, the dissertation has exemplified the application of nonlinear and linear control design techniques and has demonstrated the feasibility of completing a variety of maneuvering tasks under the assumption that elastic state measurements are available.

6.2 Key Contributions of this Dissertation

This dissertation has provide several key contributions, which can be summarized as follows.

1) A new method of calculating the desired VFA trajectory to match a climb command was enhanced to more closely match a human pilot's actions. Two different outer loop controllers were presented and demonstrated on the X-HALE aircraft to replace the original PID controller which was shown to be unstable for the X-HALE aircraft model.

2) A new lateral command tracking control scheme was presented. This architecture relies on an LQG controller designed using a reduced order linear model of the aircraft. The controller only uses the wing curvature at four points along the wing as opposed to full elastic state feedback used in the previous implementation.

3) A novel method for minimizing VFA loads caused by gust disturbances and maneuvering flight, which operates by controlling the shape of the aircraft, was developed. An LQR controller that coordinates the ailerons in order to minimize wing curvature deviations from the trim values has been designed and shown to perform well in simulations.

4) A new control architecture combining the longitudinal and lateral controllers with reference and extended command governors was introduced. The scheme effectively enforced curvature limits, with small constraint violations caused by model linearization errors, while allowing for good command tracking in all axes.

5) From the sensitivity study of the vehicle structural and flight dynamic relative char-

acteristics to gust excitation, the response is dependent on the aircraft configuration. For the two configurations studied, the flying wing aircraft shows that the bending stiffness is the most important for gust response. The X-HALE aircraft shows that both the bending and torsional stiffnesses are important.

6.3 Recommendations for Future Work

One area of future research concerns the use of elastic states for feedback. Obtaining a complete elastic state vector from a flying aircraft is difficult. One solution to this problem is to design a state estimator which uses measured outputs to construct an estimate of the elastic states. Ideally, this would be accomplished only using measured rigid body outputs. Realistically, a small set of elastic outputs, possibly obtained using strain gauges or a vision based system, will likely be necessary. The initial results in this dissertation have highlighted the need for only four elastic state measurements as being adequate for lateral control.

Another approach for dealing with the lack of elastic state availability for feedback would be to design an adaptive controller. The controller could be designed using a rigid body aircraft assumption and allow the adaptive properties of the controller to account for the elastic behavior of the aircraft.

The lateral and curvature reducing controllers could be completely integrated into a single design which is capable of coordinating outboard motors and ailerons to track yaw and roll commands subject to curvature constraints. The use of dynamic inversion for lateral control could be developed and compared to current LQR lateral controller.

Additionally, the curvature reducing controller could be redesigned so that a subset of elastic states is used as opposed to the current use of full elastic state feedback. A study could be performed to investigate the minimum number of elastic states required.

The sensitivity studies presented in this dissertation could be expanded. One possible

expansion would be to examine how the flutter and divergence boundaries change as aircraft stiffness are varied. Additionally, a study could be performed to examine if the amount of improvement of the flutter boundary due to closed loop control is a function of aircraft stiffness. Also, further examination in to the cause of the flying wing trim parameters being essentially constant is needed.

The closed loop sensitivity studies could be improved through the use of a different method to design the controllers. Separate, independent LQR controllers could be designed for each model and a comparison made between the control costs or control commands.

All of the results presented in this dissertation are based on simulation aircraft models. Once UM/NAST has been validated and updated using X-HALE flight data, the control laws presented could be validated in flight on the X-HALE aircraft.

APPENDIX A

X-HALE Airfoil Properties

The airfoil used on the X-HALE is the EMX-07. The data for the lift coefficient, C_L, drag coefficient, C_D, and moment coefficient C_M are shown in Table A.1 and are plotted in Figs. A.1 - A.3.

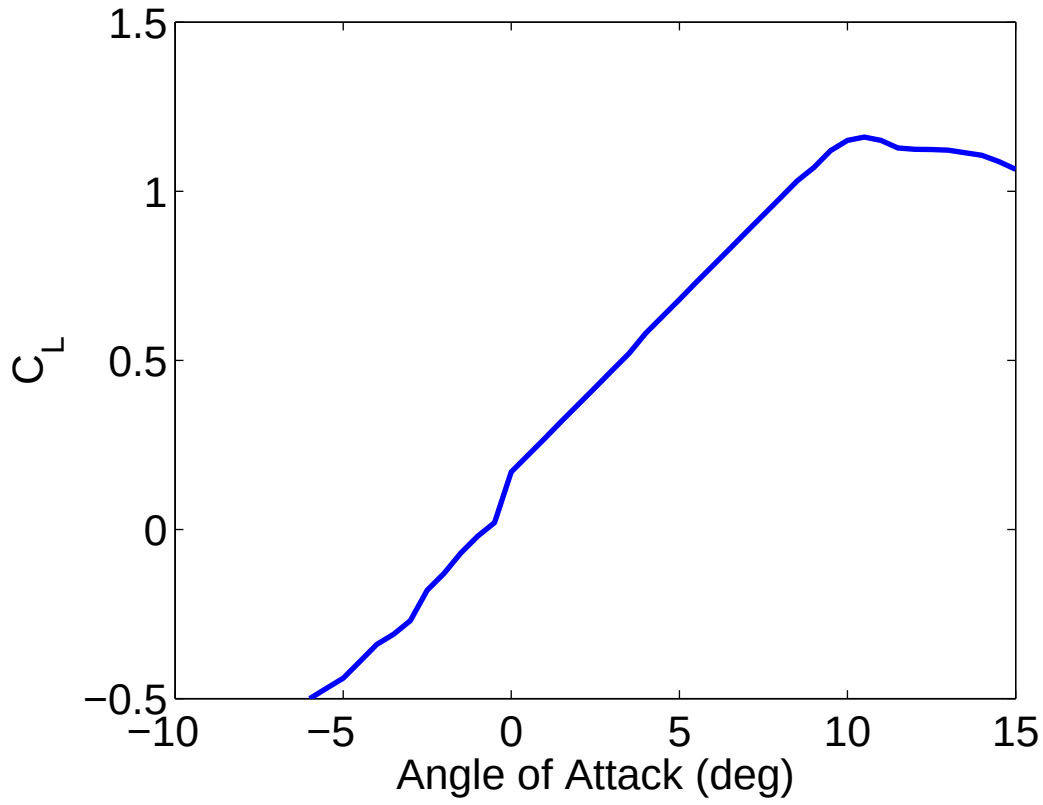

Figure A.1: EMX07 C_L α curve

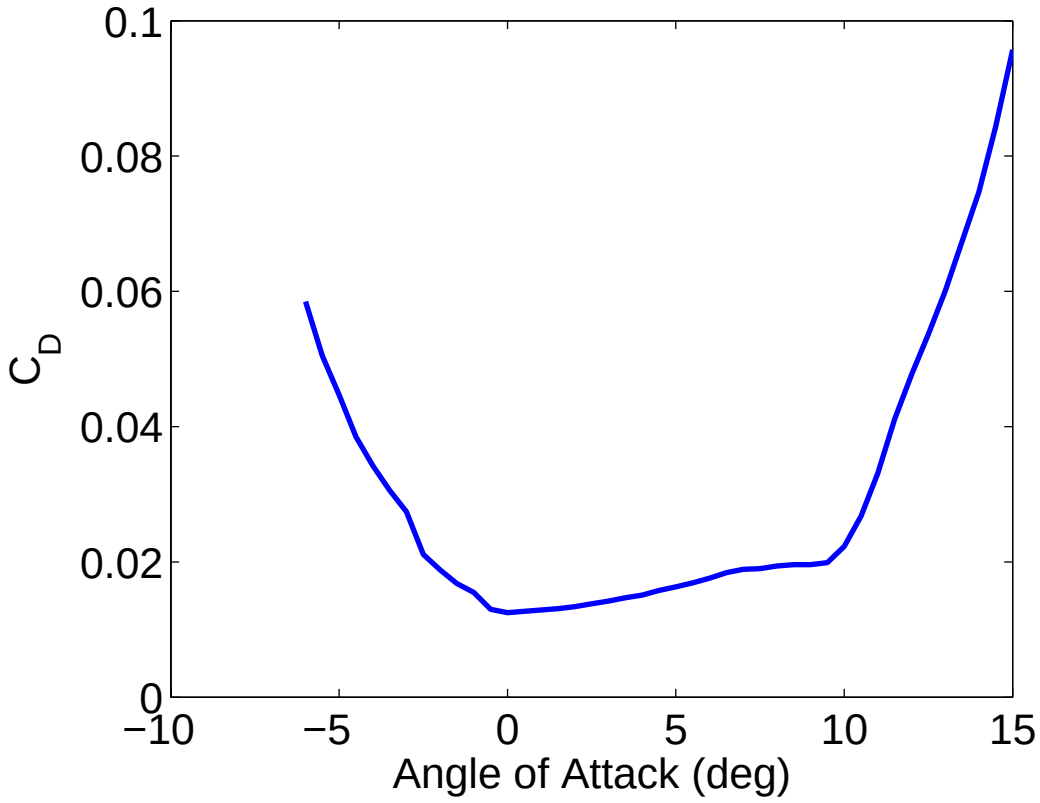

Figure A.2: EMX07 C_D α curve

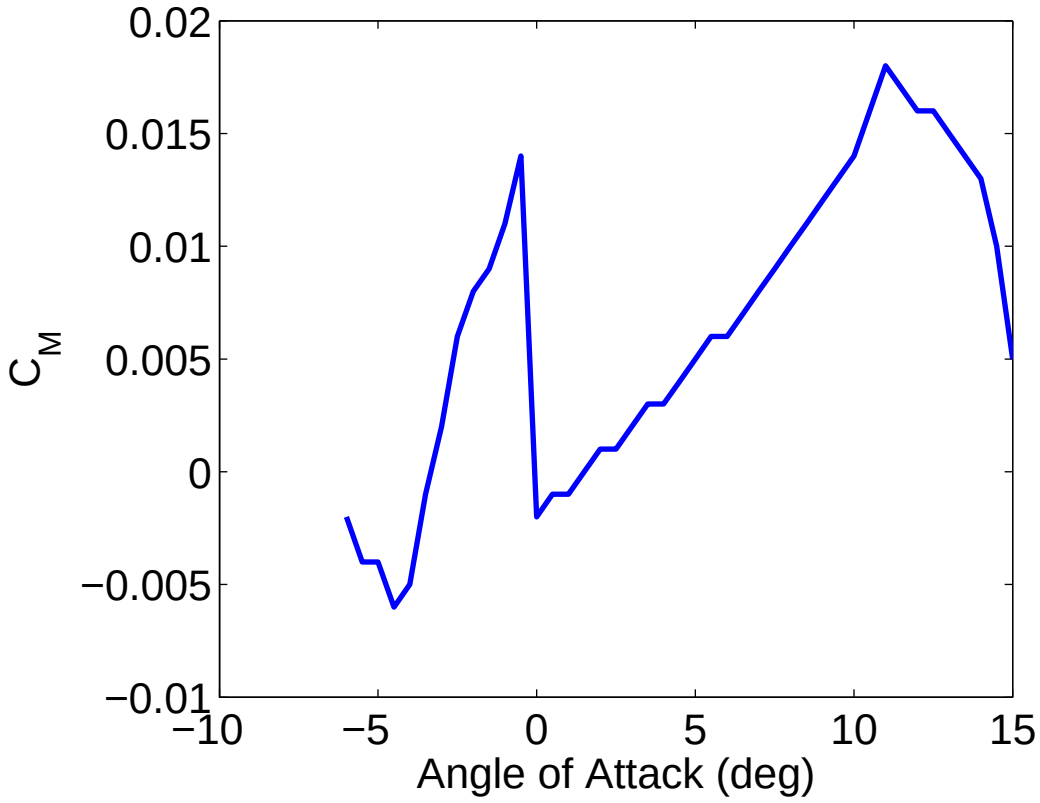

Figure A.3: EMX07 C_M α curve

Table A.1: EMX07 Airfoil Data

α (DEG)	C_L	C_D	C_M
-6.00	-0.505	0.0584	-0.0022
-5.50	-0.475	0.0505	-0.0036
-5.00	-0.436	0.0447	-0.0038
-4.50	-0.387	0.0385	-0.0060
-4.00	-0.341	0.0346	-0.0047
-3.50	-0.305	0.0306	-0.0013
-3.00	-0.265	0.0274	0.0015
-2.50	-0.181	0.0211	0.0064
-2.00	-0.126	0.0188	0.0079
-1.50	-0.073	0.0168	0.0095
-1.00	-0.022	0.0155	0.0111
-0.50	0.020	0.0130	0.0135
0.00	0.166	0.0125	-0.0019
0.50	0.217	0.0127	-0.0013
1.00	0.269	0.0129	-0.0007
1.50	0.320	0.0131	-0.0001
2.00	0.372	0.0134	0.0006
2.50	0.423	0.0138	0.0012
3.00	0.474	0.0142	0.0019
3.50	0.525	0.0147	0.0028
4.00	0.576	0.0151	0.0034
4.50	0.627	0.0157	0.0041
5.00	0.677	0.0163	0.0049
5.50	0.728	0.0169	0.0057
6.00	0.778	0.0176	0.0063
6.50	0.828	0.0183	0.0070
7.00	0.878	0.0189	0.0079
7.50	0.928	0.0190	0.0089
8.00	0.977	0.0193	0.0098
8.50	1.026	0.0195	0.0108
9.00	1.074	0.0195	0.0118
9.50	1.117	0.0199	0.0127
10.00	1.155	0.0223	0.0137
10.50	1.165	0.0268	0.0156
11.00	1.150	0.0330	0.0184
11.50	1.127	0.0411	0.0166
12.00	1.123	0.0476	0.0157
12.50	1.122	0.0537	0.0155
13.00	1.121	0.0600	0.0146
14.00	1.106	0.0747	0.0126
14.50	1.088	0.0844	0.0103
15.00	1.064	0.0957	0.0054

APPENDIX B

Derivation of Linearized Equations

This Appendix presents a derivation of the linearized control and disturbance effector matrices, commonly referred to as B and B_w, respectively. An overview of the technique for linearizing nonlinear equations about a set-point is first presented, followed by the specific case of linearizing the nonlinear aeroelastic EOM used in this study.

B.1 Linearization of Nonlinear Equations

Consider a nonlinear function of the form,

$$\dot{x} = f(x, u, w, t), \tag{B.1}$$

where $x \in \mathbb{R}^n$ is the state vector, $u \in \mathbb{R}^m$ is the control vector and $w \in \mathbb{R}^p$ is the disturbance vector. Let (x_0, u_0, w_0) be an equilibrium point of Eq. B.1, that is,

$$f(x_0, u_0, w_0, t) = 0, \tag{B.2}$$

Assume that x, u and w are perturbed from the equilibrium values,

$$x = x_0 + \delta x, \tag{B.3}$$

$$u = u_0 + \delta u, \tag{B.4}$$

$$w = w_0 + \delta w \tag{B.5}$$

Then Eq B.1 becomes

$$\dot{x}_0 + \delta\dot{x} = f(x_0 + \delta x, u_0 + \delta u, w_0 + \delta w, t) \tag{B.6}$$

A Taylor series expansion is then performed on Eq B.6, yielding

$$\dot{x}_0 + \delta\dot{x} = f(x_0, u_0, w_0, t) + \left.\frac{\partial f}{\partial x}\right|_{x_0,u_0,w_0} \delta x + \left.\frac{\partial f}{\partial u}\right|_{x_0,u_0,w_0} \delta u + \left.\frac{\partial f}{\partial w}\right|_{x_0,u_0,w_0} \delta w + HOT, \tag{B.7}$$

where HOT represents higher order terms. Next, assume that δx, δu and δw are small so that HOT can be neglected. Then

$$\delta\dot{x} = \left.\frac{\partial f}{\partial x}\right|_{x_0,u_0,w_0} \delta x + \left.\frac{\partial f}{\partial u}\right|_{x_0,u_0,w_0} \delta u + \left.\frac{\partial f}{\partial w}\right|_{x_0,u_0,w_0} \delta w, \tag{B.8}$$

Now defining

$$A = \left.\frac{\partial f}{\partial x}\right|_{x_0,u_0,w_0}, B = \left.\frac{\partial f}{\partial u}\right|_{x_0,u_0,w_0}, B_w = \left.\frac{\partial f}{\partial w}\right|_{x_0,u_0,w_0}, \tag{B.9}$$

yields the familiar form of

$$\dot{\delta x} = A\delta x + B\delta u + B_w\delta w, \tag{B.10}$$

with the δ terms usually dropped for notational convenience, which gives,

$$\dot{x} = Ax + Bu + B_w w. \tag{B.11}$$

B.2 Aeroelastic EOM Linearization

The coupled nonlinear aeroelastic and flight dynamic EOM are now linearized to yield the A, B and B_w matrices. This approach follows [25], where the A matrix was derived. Starting with Eqs 2.34 - 2.38, which are repeated here for convenience

$$M_{FF}\ddot{\varepsilon} = -M_{FB}\dot{\beta} - C_{FF}\dot{\varepsilon} - C_{FB}\beta - K_{FF}\varepsilon + R_F \tag{B.12}$$

$$M_{BB}\dot{\beta} = -M_{BF}\ddot{\varepsilon} - C_{BB}\beta - C_{BF}\dot{\varepsilon} + R_B \tag{B.13}$$

$$\dot{\zeta} = -\frac{1}{2}\Omega_\zeta \zeta \tag{B.14}$$

$$\dot{p}_B = \begin{bmatrix} C^{BG} & 0 \end{bmatrix} \beta \tag{B.15}$$

$$\dot{\lambda} = F_1 \begin{bmatrix} \ddot{\varepsilon} \\ \dot{\beta} \end{bmatrix} + F_2 \begin{bmatrix} \dot{\varepsilon} \\ \beta \end{bmatrix} + F_3 \lambda \tag{B.16}$$

where

$$\begin{bmatrix} R_F^{aero} \\ R_B^{aero} \end{bmatrix} = \begin{bmatrix} J_{p\varepsilon}^T \\ J_{pb}^T \end{bmatrix} B_F F^{aero} + \begin{bmatrix} J_{\theta\varepsilon}^T \\ J_{\theta b}^T \end{bmatrix} B_M M^{aero} \tag{B.17}$$

where $J_{p\varepsilon}$ is the structural Jacobian relating nodal positions and element strains, J_{pb} is the structural Jacobian relating nodal positions and rigid body motions, $J_{\theta\varepsilon}$ is the structural Jacobian relating nodal rotations and element strains, and $J_{\theta b}$ is the structural Jacobian relating nodal rotations and rigid body motions.

The linearization is performed about the trimmed values of the states, denoted by x_0, control surfaces and thrust forces, denoted by u_0, and disturbance, denoted by w_0, which

is assumed to be zero. In order to determine the linearization, x_0, u_0 and w_0 are perturbed by Δx, Δu, and Δw, respectively, in Eqs. B.12 - B.16. Note in the following equations that all matrices and partial derviatives are evaluated at (x_0, u_0, w_0), but this is left off for notational convinence. A Taylor Series expansion is then performed which, neglecting the higher order terms, yields,

$$\begin{aligned}
&M_{FF}\ddot{\varepsilon} + M_{FB}\dot{\beta} \\
&+ \left(C_{FF} + \frac{\partial C_{FF}}{\partial \dot{\varepsilon}}\dot{\varepsilon}_0 + \frac{\partial C_{FF}}{\partial \beta}\dot{\beta}_0 + \frac{\partial C_{FF}}{\partial u}u_0 + \frac{\partial C_{FF}}{\partial w}w_0\right)\dot{\varepsilon} \\
&+ \left(C_{FB} + \frac{\partial C_{FB}}{\partial \dot{\varepsilon}}\dot{\varepsilon}_0 + \frac{\partial C_{FB}}{\partial \beta}\dot{\beta}_0 + \frac{\partial C_{FB}}{\partial u}u_0 + \frac{\partial C_{FB}}{\partial w}w_0\right)\beta \\
&+ K_{FF}\varepsilon \\
&= R_F^{aero} + \frac{\partial R_F^{aero}}{\partial \ddot{\varepsilon}}\ddot{\varepsilon} + \frac{\partial R_F^{aero}}{\partial \dot{\varepsilon}}\dot{\varepsilon} + \frac{\partial R_F^{aero}}{\partial \varepsilon}\varepsilon + \frac{\partial R_F^{aero}}{\partial \dot{\beta}}\dot{\beta} + \frac{\partial R_F^{aero}}{\partial \lambda}\lambda \\
&+ \frac{\partial R_F^{aero}}{\partial u}u + \frac{\partial R_F^{aero}}{\partial w}w + R_F^{grav} + \frac{\partial R_F^{grav}}{\partial \zeta}\zeta + \frac{\partial R_F^{grav}}{\partial u}u + \frac{\partial R_F^{grav}}{\partial w}w
\end{aligned} \tag{B.18}$$

$$\begin{aligned}
&M_{BF}\ddot{\varepsilon} + M_{BB}\dot{\beta} \\
&+ \left(C_{BF} + \frac{\partial C_{BF}}{\partial \dot{\varepsilon}}\dot{\varepsilon}_0 + \frac{\partial C_{BF}}{\partial \beta}\dot{\beta}_0 + \frac{\partial C_{BF}}{\partial u}u_0 + \frac{\partial C_{BF}}{\partial w}w_0\right)\dot{\varepsilon} \\
&+ \left(C_{BB} + \frac{\partial C_{BB}}{\partial \dot{\varepsilon}}\dot{\varepsilon}_0 + \frac{\partial C_{BB}}{\partial \beta}\dot{\beta}_0 + \frac{\partial C_{BB}}{\partial u}u_0 + \frac{\partial C_{BB}}{\partial w}w_0\right)\beta \\
&= R_B^{aero} + \frac{\partial R_B^{aero}}{\partial \ddot{\varepsilon}}\ddot{\varepsilon} + \frac{\partial R_B^{aero}}{\partial \dot{\varepsilon}}\dot{\varepsilon} + \frac{\partial R_B^{aero}}{\partial \varepsilon}\varepsilon + \frac{\partial R_B^{aero}}{\partial \dot{\beta}}\dot{\beta} + \frac{\partial R_B^{aero}}{\partial \lambda}\lambda \\
&+ \frac{\partial R_B^{aero}}{\partial u}u + \frac{\partial R_B^{aero}}{\partial w}w + R_B^{grav} + \frac{\partial R_B^{grav}}{\partial \zeta}\zeta + \frac{\partial R_B^{grav}}{\partial u}u + \frac{\partial R_B^{grav}}{\partial w}w
\end{aligned} \tag{B.19}$$

$$\dot{\zeta} = -\frac{1}{2}\left(\Omega_\zeta\zeta + \frac{\partial \Omega_\zeta}{\partial \beta}\beta_0 + \frac{\partial \Omega_\zeta}{\partial u}u_0 + \frac{\partial \Omega_\zeta}{\partial w}w_0\right)\zeta \tag{B.20}$$

$$\dot{p}_B = \left[\left(C^{GB} + \frac{\partial C^{GB}}{\partial \zeta}\zeta_0 + \frac{\partial C^{GB}}{\partial u}u_0 + \frac{\partial C^{GB}}{\partial w}w_0\right) \quad 0\right]\beta \tag{B.21}$$

$$\dot{\lambda} = F_1 \begin{bmatrix} \ddot{\varepsilon} \\ \dot{\beta} \end{bmatrix} + F_2 \begin{bmatrix} \dot{\varepsilon} \\ \beta \end{bmatrix} + F_3 \left(\lambda_0 + \Delta\lambda \right) \tag{B.22}$$

To put the equations in state space form, Eqs B.18 - B.22 are rewritten by moving the right hand side to the left and grouping terms. Also it is assumed that the generalized mass, damping and stiffness matrices, as well as the generalized gravity force, are not functions of u or w so those terms are dropped which leads to

$$\begin{aligned} &\left(M_{FF} - R^{aero}_{F/\ddot{\varepsilon}_0}\right)\ddot{\varepsilon} + \left(M_{FB} - R^{aero}_{F/\dot{\beta}_0}\right)\dot{\beta} + \left(C_{FF} + C_{FF/\dot{\varepsilon}_0}\dot{\varepsilon}_0 + C_{FB/\dot{\varepsilon}_0}\dot{\beta}_0 - R^{aero}_{F/\dot{\varepsilon}_0}\right)\dot{\varepsilon} \\ &+ \left(C_{FB} + C_{FF/\beta_0}\dot{\varepsilon}_0 + C_{FB/\beta_0}\beta_0 - R^{aero}_{F/\dot{\beta}_0}\right)\beta + \left(K_{FF} - R^{aero}_{F/\varepsilon_0}\right)\varepsilon - R^{aero}_{F/\lambda_0}\lambda - R^{aero}_{F/u_0}u \\ &- R^{aero}_{F/w_0}w - R^{grav}_{F/\zeta_0}\zeta = 0 \end{aligned} \tag{B.23}$$

$$\begin{aligned} &\left(M_{BF} - R^{aero}_{B/\ddot{\varepsilon}_0}\right)\ddot{\varepsilon} + \left(M_{BB} - R^{aero}_{B/\dot{\beta}_0}\right)\dot{\beta} + \left(C_{BF} + C_{BF/\dot{\varepsilon}_0}\dot{\varepsilon}_0 + C_{BB/\dot{\varepsilon}_0}\dot{\beta}_0 - R^{aero}_{B/\dot{\varepsilon}_0}\right)\dot{\varepsilon} \\ &+ \left(C_{BB} + C_{BF/\beta_0}\dot{\varepsilon}_0 + C_{BB/\beta_0}\beta_0 - R^{aero}_{B/\dot{\beta}_0}\right)\beta - R^{aero}_{B/\lambda_0}\lambda - R^{aero}_{B/u_0}u \\ &- R^{aero}_{B/w_0}w - R^{grav}_{B/\zeta_0}\zeta = 0 \end{aligned} \tag{B.24}$$

$$\dot{\zeta} + \frac{1}{2}\left(\Omega_\zeta \zeta + \frac{\partial \Omega_\zeta}{\partial \beta}\beta_0\right)\zeta = 0 \tag{B.25}$$

$$\dot{p}_B - \begin{bmatrix} \left(C^{GB} + \frac{\partial C^{GB}}{\partial \zeta}\zeta_0\right) & 0 \end{bmatrix}\beta = 0 \tag{B.26}$$

$$\dot{\lambda} - F_1 \begin{bmatrix} \ddot{\varepsilon} \\ \dot{\beta} \end{bmatrix} - F_2 \begin{bmatrix} \dot{\varepsilon} \\ \beta \end{bmatrix} - F_3 \left(\lambda_0 + \Delta\lambda \right) = 0 \tag{B.27}$$

where the notation X_{y/z_0} means $\left.\frac{\partial X_y}{\partial z}\right|_{z_0}$. The generalized aerodynamic forces can be expanded using Eq. B.17,

$$
\begin{aligned}
\frac{\partial R_F^{aero}}{\partial \ddot{\varepsilon}} &= J_{p\varepsilon}^T B_F \frac{\partial F^{aero}}{\partial \ddot{\varepsilon}} + J_{\theta\varepsilon}^T B_M \frac{\partial M^{aero}}{\partial \ddot{\varepsilon}} \\
\frac{\partial R_F^{aero}}{\partial \dot{\beta}} &= J_{p\varepsilon}^T B_F \frac{\partial F^{aero}}{\partial \dot{\beta}} + J_{\theta\varepsilon}^T B_M \frac{\partial M^{aero}}{\partial \dot{\beta}} \\
\frac{\partial R_F^{aero}}{\partial \dot{\varepsilon}} &= J_{p\varepsilon}^T B_F \frac{\partial F^{aero}}{\partial \dot{\varepsilon}} + J_{\theta\varepsilon}^T B_M \frac{\partial M^{aero}}{\partial \dot{\varepsilon}} \\
\frac{\partial R_F^{aero}}{\partial \beta} &= J_{p\varepsilon}^T B_F \frac{\partial F^{aero}}{\partial \beta} + J_{\theta\varepsilon}^T B_M \frac{\partial M^{aero}}{\partial \beta} \\
\frac{\partial R_F^{aero}}{\partial \varepsilon} &= J_{p\varepsilon}^T B_F \frac{\partial F^{aero}}{\partial \varepsilon} + J_{\theta\varepsilon}^T B_M \frac{\partial M^{aero}}{\partial \varepsilon} \\
\frac{\partial R_F^{aero}}{\partial u} &= J_{p\varepsilon}^T B_F \frac{\partial F^{aero}}{\partial u} + J_{\theta\varepsilon}^T B_M \frac{\partial M^{aero}}{\partial u} \\
\frac{\partial R_F^{aero}}{\partial w} &= J_{p\varepsilon}^T B_F \frac{\partial F^{aero}}{\partial w} + J_{\theta\varepsilon}^T B_M \frac{\partial M^{aero}}{\partial w} \\
\frac{\partial R_B^{aero}}{\partial \ddot{\varepsilon}} &= J_{pb}^T B_F \frac{\partial F^{aero}}{\partial \ddot{\varepsilon}} + J_{\theta b}^T B_M \frac{\partial M^{aero}}{\partial \ddot{\varepsilon}} \\
\frac{\partial R_B^{aero}}{\partial \dot{\beta}} &= J_{pb}^T B_F \frac{\partial F^{aero}}{\partial \dot{\beta}} + J_{\theta b}^T B_M \frac{\partial M^{aero}}{\partial \dot{\beta}} \\
\frac{\partial R_B^{aero}}{\partial \dot{\varepsilon}} &= J_{pb}^T B_F \frac{\partial F^{aero}}{\partial \dot{\varepsilon}} + J_{\theta b}^T B_M \frac{\partial M^{aero}}{\partial \dot{\varepsilon}} \\
\frac{\partial R_B^{aero}}{\partial \beta} &= J_{pb}^T B_F \frac{\partial F^{aero}}{\partial \beta} + J_{\theta b}^T B_M \frac{\partial M^{aero}}{\partial \beta} \\
\frac{\partial R_B^{aero}}{\partial u} &= J_{pb}^T B_F \frac{\partial F^{aero}}{\partial u} + J_{\theta b}^T B_M \frac{\partial M^{aero}}{\partial u} \\
\frac{\partial R_B^{aero}}{\partial w} &= J_{pb}^T B_F \frac{\partial F^{aero}}{\partial w} + J_{\theta b}^T B_M \frac{\partial M^{aero}}{\partial w}
\end{aligned}
\tag{B.28}
$$

Then Eqs. B.23 - B.27 are re-written as

$$\begin{aligned}
\overline{M}_{FF}\ddot{\varepsilon} + \overline{M}_{FB}\dot{\beta} + \overline{C}_{FF}\dot{\varepsilon} + \overline{C}_{FB}\beta + \overline{K}_{FF}\varepsilon - R^{aero}_{F/\lambda_0}\lambda - R^{aero}_{F/u_0}u - R^{aero}_{F/w_0}w - R^{grav}_{F/\zeta_0}\zeta = 0 \\
\overline{M}_{BF}\ddot{\varepsilon} + \overline{M}_{BB}\dot{\beta} + \overline{C}_{BF}\dot{\varepsilon} + \overline{C}_{BB}\beta - R^{aero}_{B/\lambda_0}\lambda - R^{aero}_{B/u_0}u - R^{aero}_{B/w_0}w - R^{grav}_{B/\zeta_0}\zeta = 0 \\
\dot{\zeta} + \frac{1}{2}\left(\Omega_\zeta\zeta + \frac{\partial\Omega_\zeta}{\partial\beta}\beta_0\right)\zeta = 0 \\
\dot{p}_B - \left[\left(C^{GB} + \frac{\partial C^{GB}}{\partial\zeta}\zeta_0\right) \quad 0\right]\beta = 0 \\
\dot{\lambda} - F_1\begin{bmatrix}\ddot{\varepsilon}\\ \dot{\beta}\end{bmatrix} - F_2\begin{bmatrix}\dot{\varepsilon}\\ \beta\end{bmatrix} - F_3\left(\lambda_0 + \Delta\lambda\right) = 0
\end{aligned} \tag{B.29}$$

where

$$\begin{aligned}
\overline{M}_{FF} &= M_{FF} - J^T_{p\varepsilon}B_F\frac{\partial F^{aero}}{\partial\ddot{\varepsilon}} - J^T_{\theta\varepsilon}B_M\frac{\partial M^{aero}}{\partial\ddot{\varepsilon}} \\
\overline{M}_{FB} &= M_{FB} - J^T_{p\varepsilon}B_F\frac{\partial F^{aero}}{\partial\dot{\beta}} - J^T_{\theta\varepsilon}B_M\frac{\partial M^{aero}}{\partial\dot{\beta}} \\
\overline{M}_{BF} &= M_{BF} - J^T_{pb}B_F\frac{\partial F^{aero}}{\partial\ddot{\varepsilon}} - J^T_{\theta b}B_M\frac{\partial M^{aero}}{\partial\ddot{\varepsilon}} \\
\overline{M}_{BB} &= M_{BB} - J^T_{pb}B_F\frac{\partial F^{aero}}{\partial\dot{\beta}} - J^T_{\theta b}B_M\frac{\partial M^{aero}}{\partial\dot{\beta}} \\
\overline{C}_{FF} &= C_{FF} + \frac{\partial C_{FF}}{\partial\dot{\varepsilon}}\dot{\varepsilon}_0 + \frac{\partial C_{FB}}{\partial\dot{\varepsilon}}\beta_0 - J^T_{p\varepsilon}B_F\frac{\partial F^{aero}}{\partial\dot{\varepsilon}} - J^T_{\theta\varepsilon}B_M\frac{\partial M^{aero}}{\partial\dot{\varepsilon}} \\
\overline{C}_{FB} &= C_{FB} + \frac{\partial C_{FF}}{\partial\beta}\dot{\varepsilon}_0 + \frac{\partial C_{FB}}{\partial\beta}\beta_0 - J^T_{p\varepsilon}B_F\frac{\partial F^{aero}}{\partial\beta} - J^T_{\theta\varepsilon}B_M\frac{\partial M^{aero}}{\partial\beta} \\
\overline{C}_{BF} &= C_{BF} + \frac{\partial C_{BF}}{\partial\dot{\varepsilon}}\dot{\varepsilon}_0 + \frac{\partial C_{BB}}{\partial\dot{\varepsilon}}\beta_0 - J^T_{pb}B_F\frac{\partial F^{aero}}{\partial\dot{\varepsilon}} - J^T_{\theta b}B_M\frac{\partial M^{aero}}{\partial\dot{\varepsilon}} \\
\overline{C}_{BB} &= C_{BB} + \frac{\partial C_{BF}}{\partial\beta}\dot{\varepsilon}_0 + \frac{\partial C_{BB}}{\partial\beta}\beta_0 - J^T_{pb}B_F\frac{\partial F^{aero}}{\partial\beta} - J^T_{\theta b}B_M\frac{\partial M^{aero}}{\partial\beta} \\
\overline{K}_{FF} &= K_{FF} - J^T_{pb}B_F\frac{\partial F^{aero}}{\partial\varepsilon} - J^T_{\theta b}B_M\frac{\partial M^{aero}}{\partial\varepsilon}
\end{aligned} \tag{B.30}$$

In order to put the equations in the standard state space form the following matrices are

defined

$$Q_1 = \begin{bmatrix} I & 0 & 0 & 0 & 0 & 0 \\ 0 & \overline{M}_{FF} & \overline{M}_{FB} & 0 & 0 & 0 \\ 0 & \overline{M}_{BF} & \overline{M}_{BB} & 0 & 0 & 0 \\ 0 & 0 & 0 & I & 0 & 0 \\ 0 & 0 & 0 & 0 & I & 0 \\ 0 & -F_{1F} & -F_{1B} & 0 & 0 & I \end{bmatrix} \tag{B.31}$$

$$Q2 = \begin{bmatrix} 0 & I & 0 & 0 & 0 & 0 \\ 0 & -\overline{C}_{FF} & -\overline{C}_{FB} & R^{grav}_{F/\zeta_0} & 0 & R^{aero}_{F/\lambda_0} \\ 0 & -\overline{C}_{BF} & -\overline{C}_{BB} & R^{grav}_{B/\zeta_0} & 0 & R^{aero}_{B/\lambda_0} \\ 0 & 0 & -\frac{1}{2}\Omega_{\zeta/\beta_0}\zeta_0 & -\frac{1}{2}\Omega_{\zeta} & 0 & 0 \\ 0 & 0 & \begin{bmatrix} C^{GB} & 0 \end{bmatrix} & \begin{bmatrix} C^{GB}_{/\zeta_0} & 0 \end{bmatrix} \beta & I & 0 \\ 0 & F_{2F} & -F_{2B} & 0 & 0 & F_3 \end{bmatrix} \tag{B.32}$$

.

The control vector, u, is then broken into two pieces, control surface deflections, δ, and thrust inputs, T. This allows for

$$Q_3 = \begin{bmatrix} 0 & 0 \\ B_{\delta F} & B_{TF} \\ B_{\delta B} & B_{TB} \\ 0 & 0 \\ 0 & 0 \\ 0 & 0 \end{bmatrix} \tag{B.33}$$

where

$$B_{\delta F} = -J_{p\varepsilon}^T B_F \frac{\partial F^{aero}}{\partial \delta} - J_{\theta\varepsilon}^T B_M \frac{\partial M^{aero}}{\partial \delta},$$
$$B_{\delta B} = -J_{pb}^T B_F \frac{\partial F^{aero}}{\partial \delta} - J_{\theta b}^T B_M \frac{\partial M^{aero}}{\partial \delta}, \tag{B.34}$$

$$B_{TF} = -J_{p\varepsilon}^T \frac{\partial F^{pt}}{\partial T},$$
$$B_{TB} = -J_{pb}^T \frac{\partial F^{pt}}{\partial T}, \tag{B.35}$$

and because thrust is considered a point force,

$$\frac{\partial F^{pt}}{\partial T} = 1, \tag{B.36}$$

therefore,

$$B_{TF} = -J_{p\varepsilon}^T,$$
$$B_{TB} = -J_{pb}^T. \tag{B.37}$$

Additionally,

$$Q4 = \begin{bmatrix} 0 \\ B_{w,F} \\ B_{w,B} \\ 0 \\ 0 \\ 0 \end{bmatrix} \tag{B.38}$$

where

$$B_{w,F} = -J_{p\varepsilon}^T B_F \frac{\partial F^{aero}}{\partial w} - J_{\theta\varepsilon}^T B_M \frac{\partial M^{aero}}{\partial w},$$
$$B_{w,B} = -J_{pb}^T B_F \frac{\partial F^{aero}}{\partial w} - J_{\theta b}^T B_M \frac{\partial M^{aero}}{\partial w}. \tag{B.39}$$

Finally, Eq. B.29 can be written in the standard state space form of

$$\dot{x} = Ax + Bu + B_w w, \tag{B.40}$$

where

$$x = \begin{bmatrix} \varepsilon & \dot{\varepsilon} & \beta & \zeta & p_B & \lambda \end{bmatrix}^T, \tag{B.41}$$

$$\dot{x} = \begin{bmatrix} \dot{\varepsilon} & \ddot{\varepsilon} & \dot{\beta} & \dot{\zeta} & \dot{p}_B & \dot{\lambda} \end{bmatrix}^T, \tag{B.42}$$

and

$$\begin{aligned} A &= Q_1^{-1} Q_2, \\ B &= Q_1^{-1} Q_3, \\ B_w &= Q_1^{-1} Q_4. \end{aligned} \tag{B.43}$$

BIBLIOGRAPHY

[1] Su, W. and Cesnik, C. E. S., "Dynamic Response of Highly Flexible Flying Wings," *AIAA Journal*, Vol. 49, No. 6, 2011, pp. 324–339.

[2] Noll, T. E., Brown, J. M., Perez-Davis, M. E., Ishmael, S. D., Tiffany, G. C., and Gaier, M., "Investigation of the Helios Prototype Aircraft Mishap," Tech. rep., NASA, Jan. 2004.

[3] van Schoor, M., Zerweckh, S. H., and von Flotow, A. H., "Aeroelastic Stbility and Control of a Highly Flexible Aircraft," *Proceedings of the 30th AIAA/ASME,/ASCE/AHS/ASC Structures, Structural Dynamics and Materials Conference*, Mobile, AL, 1989.

[4] Pail, M. J., Hodges, D. H., and Cesnik, C. E. S., "Nonlinear Aeroelasticity and Flight Dynamics of High-Altitude Long Endurance Aircraft," *Journal of Aircraft*, Vol. 38, No. 1, 2001, pp. 88–94.

[5] Chang, C. S., Hodges, D. H., and Patil, M. J., "Flight Dynamics of Highly Flexible Aircraft," *Journal of Aircraft*, Vol. 45, No. 2, 2008, pp. 538–545.

[6] Palacios, R. and Cesnik, C. E. S., "Structural Models for Flight Dynamic Analysis of Very Flexible Aircraft," *Proceedings of the 50th AIAA/ASME,/ASCE/AHS/ASC Structures, Structural Dynamics and Materials Conference*.

[7] Shearer, C. M. and Cesnik, C. E. S., "Nonlinear Flight Dynamics of Very Flexible Aircraft," *Journal of Aircraft*, Vol. 44, No. 5, 2007, pp. 1528–1545.

[8] Palacios, R., Cesnik, C. E. S., and Reichenbach, E. Y., "Re-examined Structural Design Procedures for Very Flexible Aircraft," *International Forum on Aeroelasticity and Structural Dynamics*, Stockholm, Sweden, 2007.

[9] Hesse, H. and Palacios, R., "Reduced-Order Aeroelastic Models for the Dynamics of Manoeuvering Flexible Aircraft," *International Forum on Aeroelasticity and Structural Dynamics*, Bristol, UK, 2013.

[10] Hesse, H. and Palacios, R., "Consistent Structural Linearization in Flexible Body Dynamics with Large Rigid Body Motion," *Computers and Structures*, Vol. 110, 2012, pp. 1–14.

[11] Mclean, D., "Gust-alleviation Control Systems for Aircraft," *Proceedings of the Institution of Electrical Engineers*, Vol. 125, No. 7, 1978, pp. 675–685.

[12] Botz, R., Boustani, I., Vayani, N., Bigras, P., and Wong, T., "Optimal Control Laws for Gust Alleviation," *Canadian Aeronautics and Space Journal*, Vol. 47, No. 1, 2001, pp. 1–6.

[13] Shao, K., Wu, A., Yand, C., Chen, L., and Lu, B., "Design of an Adaptive Gust Response Alleviation Control System: Simulations and Experiments," *Journal of Aircraft*, Vol. 47, No. 3, 2010, pp. 1022–1029.

[14] Rui, W., Xiaoping, Z., and Zhou, Z., "Design Gust Alleviation Controller for Highly Flexible Solar UAV," *Proceedings of the Third International Conference on Measuring Technology and Mechatronics Automation*, Shanghai, China, 2011.

[15] Haghighat, S., Liu, H. H. T., and Martins, J. R. R. A., "Model-Predictive Gust Load Alleviation controller for a Highly Flexible Aircraft," *Journal of Guidance, Control, and Dynamics*, Vol. 35, No. 6, 2012, pp. 1751–1766.

[16] Shearer, C. M. and Cesnik, C. E. S., "Trajectory Control for Very Flexible Aircraft," *Journal of Guidance, Control, and Dynamics*, Vol. 31, No. 2, 2008, pp. 340–357.

[17] Shearer, C. M., *Coupled Nonlinear Flight Dynamics, Aeroelasticity and Control of Very Flexible Aircraft*, Ph.D. thesis, University of Michigan, 2006.

[18] Gibson, T. E., Annawwamy, A. M., and Lavretsky, E., "Modeling for Control of Very Flexible Aircraft," *AIAA Guidance, Navigation and Control Conference*, Portland, OR, August 2011.

[19] Cesnik, C. E. S., Ortega-Morales, M., and Patil, M., "Active Aeroelastic Tailoring of High Aspect Ratio Composite Wings," *41st AIAA/ASME/ASCE/AHS/ASC Structures, Structural Dynamics and Materials Conference and Exhibit*, Atlanta, GA, April 2000.

[20] Patil, M. and Hodges, D. H., "Output Feedback Control of the Nonlinear Aeroelastic Response of a Slender Wing," *Journal of Guidance, Control, and Dynamics*, Vol. 25, No. 2, 2002, pp. 302–308.

[21] Raghavan, B. and Patil, M. J., "Flight Control for Flexible High-Aspect-Ratio Flying Wings," *Journal of Guidance, Control, and Dynamics*, Vol. 33, No. 1, 2010, pp. 64–74.

[22] Cook, R. G., Palacios, R., and Goulart, P., "Robust Gust Alleviation and Stabilization of Very Flexible Aircraft," *AIAA Journal*, Vol. 51, No. 2, 2013, pp. 330–340.

[23] Wang, Y., Wynn, A., and Palacios, R., "Robust Aeroelastic Control of Very Flexible Wings using Instrinsic Models," *54th AIAA/ASME/ASCE/AHS/ASC Structures, Structural dynamics, and Materials Conference*, Boston, MA, 2005.

[24] Brown, E. L., *Integrated Strain Actuation in Aircraft with highly Flexible Composite Wings*, Ph.D. thesis, Massachusetts Institute of Technology, 2003.

[25] Su, W., *Coupled Nonlinear Aeroelasticity and Flight Dynamics of Fully Flexible Aircraft*, Ph.D. thesis, University of Michigan, 2008.

[26] Su, W. and Cesnik, C. E. S., "Nonlinear Aeroelasticity of a Very Flexible Blended-Wing-Body Aircraft," *Journal of Aircraft*, Vol. 47, No. 5, 2010, pp. 1539–1553.

[27] Su, W. and Cesnik, C. E. S., "Nonlinear Aeroelastic Simulations of a Flapping Wing Micro Air Vehicle Using Two Unsteady Aerodynamic Formulations," *51st AIAA/ASME/ASCE/AHS/ASC Structures, Structural dynamics, and Materials Conference*, Orlando, FL, 2005.

[28] Su, W. and Cesnik, C. E. S., "Strain-based Geometrically Nonlinear Beam Formulation for Modeling of Very Flexible Aircraft," *International Journal of Solids and Structures*, Vol. 48, 2011, pp. 2349–2360.

[29] Stevens, B. L. and Lewis, F. L., *Aircraft Control and Simulation*, John Wiley and Sons, Inc., New York, 1992.

[30] Peters, D. A. and Johnson, M. J., "Finite State Airloads for Deformable Airfoils on Fixed and Rotating Wings," *Symposium on Aeroelasticity and Fluid/Structure Interaction/Proceedings of the Winter Annual Meeting*, Fairfield, NJ, 1994.

[31] Arora, J. S., *Introduction to Optimum Design*, Mc-Graw Hill, Inc, 1989.

[32] Shearer, C. M. and Cesnik, C. E. S., "Modified Generalized-α Method for Integrating Governing Equations of Very Flexible Aircraft," *47th AIAA/ASME/ASCE/AHS/ASC Structures, Structural dynamics, and Materials Conference*, Newport, RI, May 2006.

[33] Newmark, N. M., "A Method for Computation for Structural Dynamics," *Journal of the Engineering Mechanics Division, Proceedings of The American Society of Civil Engineers*, Vol. 85, 1959, pp. 67–94.

[34] Chung, J. and Hulbert, G. M., "A time Integration Algorith for Structural Dynamics With Improved Numerical Dissapation: The Generalized-α Method," *Journal of Applied Mechanics*, Vol. 60, 1993, pp. 371–375.

[35] Jansen, K. E., Whiting, C. H., and Hulbert, G. M., "A Generalized-α Method for Integrating the Filtered Navier-Stokes Equations with a Stabilized Finite Element Method," *Computer Methods in Applied Mathematics and Engineering*, Vol. 190, No. 3, 2000.

[36] Hughes, T. J. R., *The Finite Element Method, Linear Static and Dynamic Finite Element Analysis*, Prentice Hall, 1987.

[37] Wilson, E. B., "Theory of an Aeroplane Encountering Gusts," Tech. rep., NACA, Report 1, Part 2, 1915.

[38] McLean, D., *Automatic Flight Control Systems*, Prentice Hall, 1990.

[39] Hoblit, F. M., *Gust Loads on Aircraft: Concepts and Applications*, AIAA Education Series, 1988.

[40] anon, "Federal Aviation Regulation (FAR) 23," Tech. rep., Federal Aviation Administration, Title 14, Part 23, August 2013.

[41] anon, "Vulture II Broad Agency Announcement," Tech. rep., Defense Advanced Research Projects Agency, DARPA-BAA-10-04, October 2009.

[42] Nelson, R. C., *Flight Stability and Automatic Control*, McGraw-Hill, Inc., 1998.

[43] Patil, M. J. and Hodges, D. H., "Flight Dynamics of Highly Flexible Flying Wings," *Journal of Aircraft*, Vol. 43, No. 6, 2006, pp. 1790–1799.

[44] McKay, M. D., Beckman, R. J., and Conover, M. J., "A Comparison of Three Methods for Selecting Values of Input Variables in the Analysis of Output from a Computer Code," *Technometrics*, Vol. 21, 1979, pp. 239–245.

[45] Holman, J. P., *Experimental Methods for Engineers*, McGraw Hill, 2001.

[46] Skelton, R. E., *Dynamic Systems and Control: Linear Systems Analysis and Synthesis*, John Wiley and Sons, Inc, 1988.

[47] Kreindler, E. and Sarachik, P. E., "On the Concepts of Controllability and Observability of Linear Systems," *IEEE Transactions on Automatic Control*, Vol. 9, No. 2, 1964, pp. 129–136.

[48] Skogestag, S. and Postlethwaite, I., *Multivariable Feedback Control Analysis and Design*, John Wiley and Sons, Inc, 2005.

[49] Khalil, H. K., *Nonlinear Systems*, Third Edition, Prentice Hall, 2002.

[50] Slotine, J. E. and Li, W., *Applied Nonlinear Control*, Prentice Hall, 1991.

[51] Lin, C. F., *Advanced Control System Design*, Prentice Hall, 1994.

[52] Gilbert, E. G. and Kolmanovsky, I., "Fast Reference Governors for systems with State and Control Constraints and Disturbance Inputs," *International Journal of Robust and Nonlinear Control*, Vol. 9, No. 15, 1999, pp. 1117–1141.

[53] Dillsaver, M. J., Kalabic, U. V., Kolmanovsky, I. V., and Cesnik, C. E. S., "Constrained Control of Very Flexible Aircraft using Reference and Extended Command Governors," *American Control Conference*, Washington, D.C., 2013.

[54] Kolmanovsky, I. V. and Gilbert, E. G., "Theory and computation of disturbance invariant set of discrete-time linear systems," *Mathematical Problems in Engineering*, Vol. 4, No. 7, 1998, pp. 317–367.

[55] Gilbert, E. G. and Ong, C. J., "Constrained linear systems with hard constraints and disturbances: An extended command governor with large domain of attraction," *Automatica*, Vol. 47, No. 1, 2011, pp. 334–340.

[56] Vahidi, A., Kolmanovsky, I., and Stefanopoulou, A., "Constraint management in fuel cells: a fast reference governor approach," *IEEE Trans. Control Syst. Technol.*, Vol. 13, No. 6, 2005, pp. 911–920.